博士論文

Inverse sound rendering : In-situ estimation of surface acoustic impedance for acoustic simulation and design of real indoor environments

(インバースサウンドレンダリング：内部空間の表面の音響特性推定を目的とした音響逆問題解析)

A Dissertation submitted to the
Graduate School of Information Science and Technology
of the University of Tokyo

by

Gabriel Pablo Nava

47405

東京大学大学院
情報理工学系研究科
電子情報学専攻

Supervisor　　Sato Yoichi

指導教官　　佐藤　洋一

December, 2006

平成 18 年 12 月

Abstract

When acoustic engineers make analysis of the sound propagation with numerical methods, they use values of the acoustic properties of the objects to describe the behavior of a given object when a sound wave hits its surface. In other words, these numerical methods often require the specification of boundary conditions that characterize the acoustic properties of the materials. For example, once the acoustic properties of the materials are known, numerical analysis such as boundary or finite element methods can be applied to predict and control the sound field by manipulation of the analyzed materials. In the present work, of particular interest is the development of a method to measure the acoustic property called ”normal acoustic impedance” of the interior surfaces of a room, (in what follows it will be referred sometimes as to simply ”impedance”). On the other hand, since the 3D model of the room is assumed to be known, we may simulate modifications of that room and use the estimated acoustic impedances to make predictions of the sound response that we would hear if we did the actual modifications in the real room. This is important for example in the early stages of the acoustic design of concert halls, seminar rooms, audio studios, etc. where an optimum acoustic design should be determined in advance before making costly expenses.

The kind of problem addressed in this work deals with situations where samples of materials cannot be taken to an acoustic laboratory to measure their acoustic impedance with specialized devices. Therefore, if the impedance of those materials is desired, in-situ measurements must be performed. In the present work, two algorithms for the estimation of acoustic impedance are presented. Both algorithms are based on the solution of the Helmholtz Integral Equation (HIE) of the wave propagation in a homogeneous media. Hence, the underlying theory of these algorithms is the Boundary Element Method (BEM) and the Inverse Boundary Element Method (IBEM). Similar approaches based on these theoretical frameworks have been proposed for the identification of noise sources in a vibrating system. However, the present work represents a first attempt to estimate the

acoustic impedances in interior spaces of arbitrary shapes (such as real rooms).

The basic idea for a system of the inverse estimation of acoustic impedances is therefore as follows: a sound source is placed in a known position inside a room (e.g. an office, a conference room, a hall, etc.), then a harmonic tone is emitted. As the sound travels and reflects on the surfaces, a microphone is recording samples of sound while moving freely in space. After a number of samples are recorded the sound source stops. Now the problem is: given the 3D model of the interior space, the strength of the sound emitted by the source, and the set of recorded samples of sound, the objective is to estimate the acoustic impedance of the surfaces in that interior space.

The approach proposed in this work to solve this problem consists of breaking the geometric model into N elements and using the measured sound samples. Then applying the IBEM theory, a large system of equations is constructed. The unknowns of this linear system are the boundary values of the HIE which happen to be the parameters that define the impedances at the surfaces. Therefore the solution of this linear problem leads to the sought acoustic impedance values. Nevertheless, the solution is not achieved straight forward since this kind of inverse problems are usually ill-posed, meaning that if one wants to find a solution to the linear system in the least-square sense, there exist many vectors in the solution space that minimize the residual norm of the least-squares. In other words, the system is not uniquely solvable and there maybe an infinite number of minimizing vectors near the desired solution. This is a direct consequence of the fact that the system of equations is rank deficient. Moreover, the ill-conditioning of the matrix makes the linear problem sensitive to the noise introduced to the data during the measurement process. Because of these reasons, extra information of the sought solution should be given in the form of constraints to the linear system (this process is usually known as *regularization*).

A number of regularization methods have been proposed in the literature, being *Tikhonov regularization* the most widely used. Other regularization techniques are based on the singular value decomposition (SVD) of the linear system. But on the other hand, while the application of existent regularization methods improves the accuracy of the solutions, the estimation of the amount of regularization is usually a complex work resulting in extra computational cost. And as the dimensionality of the problem becomes large, the limitations imposed by the regularization step are more predominant.

Hence, as an alternative to overcome these difficulties, the methods proposed in this dissertation attempt to solve the ill-conditioned linear system by exploiting a prior knowl-

edge of the geometrical segmentation of the surfaces. This information is introduced as a physically-meaning constraint. The first proposed method consists of a non-linear Least-squares optimization approach aims to find the sound pressure and the particle velocity (parameters that define the acoustic impedance) at each discrete element of the 3D mesh, consequently a good approximation (in terms of geometric resolution) to the distribution of the impedance values over the surfaces is obtained. A strong pitfall of this approach is that the solutions tend to have large variance as the dimension of the geometry grows.

A second approach is an iterative optimization process that estimates directly the sought impedances under the assumption that the interior surfaces have homogenous impedance values. This assumption allows in addition a dramatic reduction of the dimensionality of the optimization problem, and therefore being able to keep an acceptable accuracy for large-scale problems. Another advantage of this method is its robustness to the perturbations in the measured data, due to the fact that the inversion of the ill-conditioned matrix is not required. A drawback of this second approach is its slow convergence.

In the evaluation part, the performance of the methods proposed here is investigated by means of numerical simulations with basic geometrical shapes (such as a unitary cube) and with realistic 3D models (an office room). In addition to the simulations, validation experiments are realized by attempting to estimate the acoustic impedance of the interior walls of a reverberation chamber. Regarding the experimental setup system, the use of video cameras is introduced in this research work to perform 3D real-time tracking of the position of the microphone. This 3D tracking technique permits the acquisition of huge amounts of sound samples in the interior space. Results of the simulations and the experiments are presented and discussed in this dissertation.

Acknowledgements

During the development of the present work many people have been involved directly or indirectly, and I would be threatened by the risk of omitting names if I was to list all of them. However I would like to mention first the Japanese Ministry of Education, Culture and Science for their support granted for the completion of my studies in Japan.

Secondly, the academic guidance of my PhD supervisor and mentor, Professor Yoichi Sato from the Institute of Industrial Science of the University of Tokyo, was a key ingredient to bring my research work into a successful achievement of my doctoral course. I would like to go back a little in time, right after Prof. Sato's course on Digital Image Processing of winter-2003 was completed. An accidental meeting with Prof. Sato at the entrance of a subway station ended in a talk about a possible research taking ideas from apparently two uncorrelated areas, Acoustics and Image Rendering. Without noticing, that talk would become later our first research meeting followed by an intensive doctoral work which is now presented in this dissertation. I am grateful to Prof. Sato for his wise encouragement.

I want to express special thanks to Prof. Shinichi Sakamoto and Dr. Yosuke Yasuda who unconditionally provided invaluable theoretical and technical support for the advance of my research. Most of my experience on numerical methods for acoustics and acoustic measurements is due to Prof. Sakamoto and Dr. Yasuda. Thanks also to the members of Sakamoto's Laboratory.

My sincere thanks to the members of Yoichi Sato's Lab who played an important role with their eventual suggestions and technical discussions. Takahiro Okabe and Imari Sato provided supporting ideas for my understanding of some Image Rendering techniques.

Finally, I am infinitely grateful to another team who from behind the action scenery gave me shouts of encouraging words all along the way of this PhD marathon: I dedicate this dissertation to my parents, Gabriel and Elena, and my brothers, Sonia and Mario.

Table of Contents

Nomenclature

$[\ ]^H$ Hermitian transposed.

α_i Singular values of a given matrix, obtained by SVD.

δ_{ik} Kronecker function. $\delta_{ik} = 1$ if $i = k$, and $\delta_{ik} = 0$ otherwise.

Γ Propagation domain different from the boundaries.

λ Wavelength.

$\langle\ \cdot\ \rangle$ Element–wise vector or matrix product.

$\mathbf{\Delta}$ Matrix of the Kronecker values δ_{ik}.

$\mathbf{A}_f, \mathbf{B}_f$ Influence matrices when the evaluation points are placed in the sound field, different from the boundaries.

$\mathbf{A}_S, \mathbf{B}_S$ Influence matrices when the evaluation points are placed on the nodes of the surface mesh.

$\mathbf{C}$ Acoustic transfer matrix of an inverse acoustic problem.

$\mathbf{C}^+$ Pseudo-inverse of the acoustic transfer matrix $\mathbf{C}$.

$\mathbf{G}$ Matrix of the constraining term in a non-linear least-squares optimization.

$\mathbf{H}$ Matrix of the transfer functions $H_{i,k}$.

$\mathbf{I}$ Identity matrix.

$\mathbf{n}$ Vector normal to the surface S.

$\mathbf{p}_f$ Vector of sound pressures at M points in the interior field.

$\mathbf{p}_S$ Vector of sound pressures at the nodes of the surface mesh.

$\mathbf{r}_{\mathrm{P}}$ Position vector of the receiving point.

$\mathbf{r}_{\mathrm{Q}}$ Position vector of the source point.

$\mathbf{U}\mathbf{\Sigma}\mathbf{V}^H$ Singular value decomposition (SVD) of a matrix.

$\mathbf{v}_S$ Vector of normal velocities at the nodes of the surface mesh.

G Green's function.

Z_0 Characteristic acoustic impedance of the propagation medium.

Z_{c} Characteristic acoustic impedance of a material.

Z_{r} Relative acoustic impedance.

Z_{max} Upper impedance bound of an optimization process.

μ Weighting factor of a non-linear least-squares optimization.

ω Angular frequency.

$\overline{\mathbf{u}}_i, \overline{\mathbf{v}}_i$ Column vectors of the orthonormal matrices $\mathbf{U}$ and $\mathbf{V}$ respectively.

$\partial_{\mathrm{n}} = \frac{\partial}{\partial \mathrm{n}}$ Partial derivative with respect to the normal.

ρ Density of the propagation media ($\approx 1.21 \frac{kg}{m^3}$ for air).

θ_v Phase of the particle velocity of the sound source.

$\widehat{\mathbf{B}}$'s Influence coefficients of the known particle velocities $\widehat{\mathbf{v}}_S$.

$\widehat{\mathbf{q}}$ Vector of sound pressures due to the punctual volume source q.

$\widehat{\mathbf{v}}_S$ Particle velocities known a priori from direct measurements.

$\widetilde{\mathbf{B}}$'s Influence coefficients of the unknown particle velocities $\widetilde{\mathbf{v}}_S$.

$\widetilde{\mathbf{v}}_S$ Unknown particle velocities of the surface elements.

c Speed of sound. $c \approx 343\ \mathrm{m/s}$ in air at $20°\mathrm{C}$.

C_{P} Scaling factor of the pressure at some point.

dS Differential with respect to the surface S.

dV Differential of volume.

$H_{i,k}$ Transfer function relating the discrete source element i with the acoustic pressure at the point k in the sound field.

$k(\ \cdot\ )$ Condition number of a linear system.

M Number of measurement points in the acoustic field.

N Total number of discrete elements in the surface mesh.

p Sound pressure.

p_{e} Component of noise in the measured field pressure.

p_{T} True pressure component of the measured field pressure.

p_f Sound pressure at a point in the interior field.

p_s Pressure on the surface of an element.

Q Mesh quality factor.

q Punctual volume sound source.

r Distance between the source point and the receiving point.

S Surface boundary enclosing the complete volume under consideration.

s Surface of a single element of the the 3D mesh.

S_i Surfaces of different types of materials contained in the general surface S.

SNR Signal to noise ratio in decibels.

v_{n} Normal component of the particle velocity.

v_{source} Particle velocity of the vibrating sound source.

v_s Normal velocity on the surface of an element.

Z Normal acoustic impedance.

Z_s Normal acoustic impedance on the surface element s.

$\mathbf{z}$ Vector of surface impedances at each element.

List of Tables

List of Figures

Chapter 1

Introduction

1.1 Motivation of this research

1.1.1 Inverse rendering techniques

Let us imagine the interior of an empty room of given dimensions, in which the only things that can be seen are the entrance door, the white walls and a big window facing to the exterior. There is no furniture in this room. If we are architectures, designers, or simply we are thinking of renting that room, we usually face the problems of trying to imagine how such a room would look once the furniture is brought in, or new lamps are installed, or how it looks when the sunshine comes in at mornings, the illumination at night, etc.. Even more, we are also interested to know how noisy is inside this room, or how our new audio system would sound when it is brought inside the room. Answers to such questions are not easy to figure out before making the corresponding expenses in all those modifications. One way to previsualize the final room effects is by means of simulations. In this point, since the appearance of the Virtual Reality (VR) area, sophisticated and high quality virtual environments have been achieved, and they are used basically for the purpose of simulation of specific real-world spaces. However there is still a gap between the synthesized virtual environments and the real sceneries. This gap would be reduced if there was the possibility to ”copy” the physical properties of the objects in the real-world and use them to produced more realistic simulations. The latter problem has been the motivation of research in a recently appeared area known as *Inverse Rendering*. The basic idea of inverse rendering techniques is that, given a parametric model that represents a determined physical phenomenon, it is possible to estimate some physical properties of the objects that are of interest (e.g. the light-reflectance properties, or sound absorption,

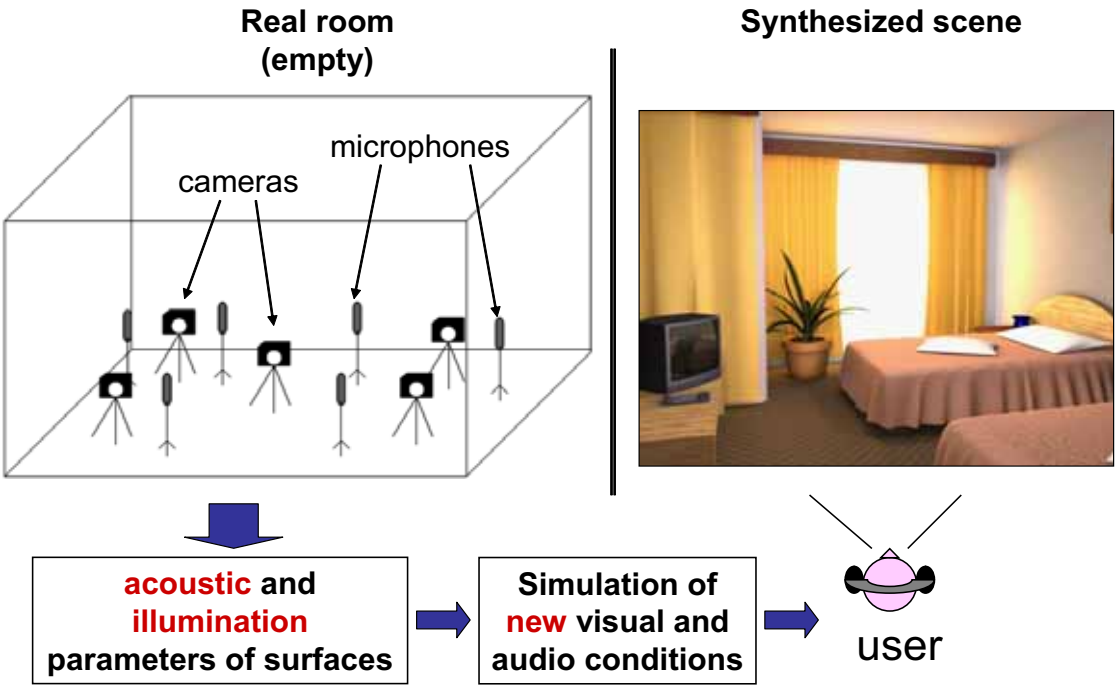

Figure 1.1: By *inverse rendering* techniques, acoustic and illumination parameters are acquired. These parameters are used then to simulate new audio-visual conditions inside a room.

etc.), by using samples of the measurable phenomenon and inverting the parametric model available. Thus, returning to our example of the empty room, it would be desirable to acquire the luminance and acoustic properties of the empty room by an inverse process, and then use them in combination with simulated objects in order to predict the final audio-visual effect in that room. Figure 1.1 summarizes this idea.

Solution to the problem of visual simulation has been already studied, and techniques with notable results were proposed in the Computer Graphics area[1]. Nevertheless, for the part of audio simulation in this context, no approaches have been proposed. Similar to the inverse image rendering algorithms, a method that allow us to capture the acoustic properties of the materials in a real environment – process that is referred in the present dissertation as *inverse sound rendering* – is still a challenge and motivation for research.

[1]Work on this area is discussed in further sections.

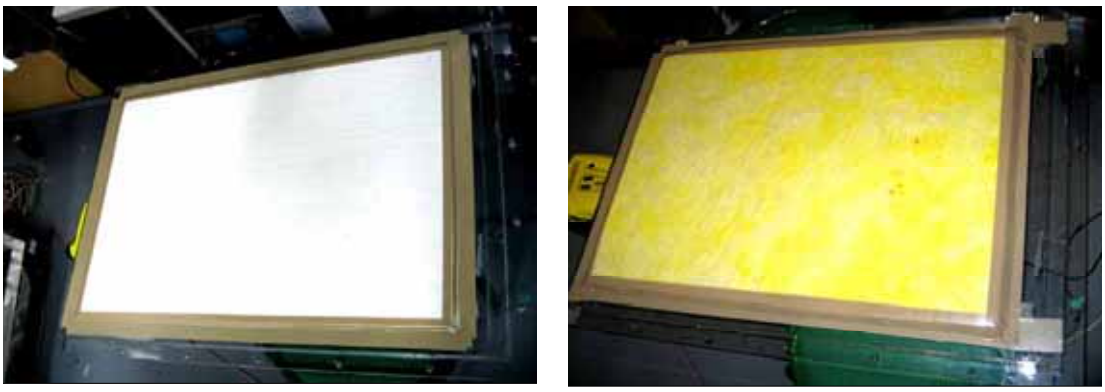

Wool felt Glass wool

a) b)

Figure 1.2: Samples of absorbent materials used for the control sound reverberation.

1.1.2 In-situ measurement of acoustic parameters

Prediction of sound fields with numerical methods has been widely used for noise control, acoustic building design and recently for sound rendering of virtual reality environments. These methods often require the specification of boundary conditions that characterize the acoustic properties of the materials. For example, once the acoustic impedances of the materials are known, numerical analysis such as *boundary* or *finite* element methods can be applied to predict and control the sound field by manipulation of the analyzed materials. For these purposes, tables and databases of acoustic property values – such as sound absorption and acoustic impedance – have been made available in the literature (e.g. [12]) and in the web (e.g. [83]). Usually these values are obtained by measuring directly the desired parameter at the laboratories using samples of the materials and employing devices specifically developed for that purpose, for example the impedance tube [35]. Figure 1.2 shows two examples of materials commonly used for the control of sound fields and that are frequently measured at the laboratory. However, values of the acoustic parameters measured at the laboratory, or found in tables, tend to change when the material is installed in other conditions different from those in the laboratory. Moreover, there are situations in which it is not always possible or desirable to take samples of the materials to the laboratory for proper measurements, and instead their acoustic characteristics have to be estimated in their original location (in-situ). Therefore, the development of a system that allows us to estimate the acoustic properties of the materials in their original location became the motivation for the development of the present work.

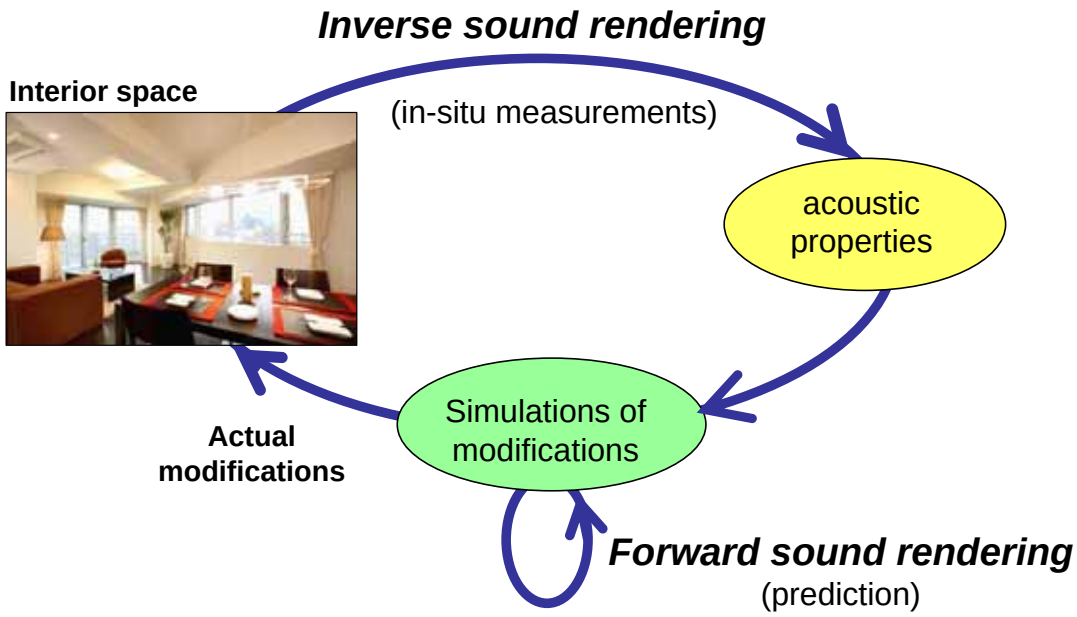

Figure 1.3: Acoustic iterative optimization process involving *inverse* and *forward* sound rendering.

1.2 The goal of this research

In the present work, of particular interest is the development of a method to measure the acoustic property called ”normal acoustic impedance” of the surfaces of an enclosed interior spaces. For instance, as in the example illustrated in Figure 1.1., the estimated values of acoustic impedance are then intended to be used for simulation purposes using numerical methods that are based on the solution of the wave equation. Hence, the impedances obtained by the proposed method are approximations to impedance values that would be measured if the analyzed surfaces were taken to the laboratory or were measured with specialized devices. On the other hand, the impact of the work carried on during the preparation of this dissertation, is basically in two areas: a) it will aid the assessment of acoustic characteristics of materials difficult to measure with current techniques, specially with comlex geometric shapes, and b) it will greatly aid to save costly expenses on the acoustic design of interior spaces by means of an acoustic iterative optimization process that involves an inverse assessment process (in-situ measurement of acoustic properties) and a forward prediction (simulation of the modifications) of the produced sound fields. Figure 1.3 illustrate this acoustic iterative process.

It is emphasized that although the targeted application of the presented algorithms is

to aid the prediction of the acoustic response of indoor environments, the auralization techniques to produce sound effects are out of the scope of this dissertation. Furthermore, because the numerical method (BEM) used as the basis of this work is in principle computationally expensive, the numerical analysis and experiments presented here, are limited to the frequency range 125 Hz to 1 kHz. It is also worth to state some general assumptions that are made all along the discussions of this dissertation:

- The propagation media of the interior space is air, and has homogeneous characteristics such as density $\rho = 1.21\ \mathrm{kg/m^3}$ and speed of sound $c = 343\ \mathrm{m/s}$ at a constant temperature of $20°\mathrm{C}$.
- All surfaces in the interior space are impedance surfaces, i.e. the only source of sound is the experimental speaker which is vibrating harmonically.
- Due to the current implementation of the BEM software in this work, thin layers in the interior of room are not considered. Nonetheless, the methods proposed here are valid for other implementations of BEM capable to deal with thin layers.
- The area of the surfaces of each material is constant and the materials are static in space.
- There are no people inside the enclosed space.

Another aspect to point out is the nature of the acoustic impedance to be estimated. Since the inverse method introduced in this work is based on the acoustic BEM theory, the surface parameters such as surface pressure and particle velocity represent the normal components with respect to the surface. Therefore, the acoustic impedance considered in the rest of the discussions is that of the normal incidence of the sound waves arriving to an specific surface point. Local reaction on the incidence point is also assumed to be the predominant effect on the surfaces. In order to ensure the latter assumption the experiments presented include hard surfaces and absorbent surfaces backed with a rigid planes.

1.3 Outline of the thesis

Chapter 2 is dedicated to present a discussion on previous approaches. The work related to this dissertation covers two major topics: works on in-situ measurement of acoustic

impedance and works on inverse illumination rendering from Computer Graphics. The basic concept in the latter served as inspiration for the development of a parallel idea in the acoustics area which is proposed in this dissertation, thus, a brief review on this work is worth as well.

Chapter 3 and chapter 4 introduce the fundamental theory in which the proposed methods are based. The acoustic *boundary element method* (BEM) for the analysis of interior fields is discussed first in chapter 3 together with its application to the analysis of standard benchmark problems in order to validate its actual implementation. Chapter 4 undertakes the theory *inverse boundary element method* (IBEM) applied to the reconstruction of acoustic parameters on the surface of a vibrating object. The introductory part of that chapter starts with a talk on the state of the art on the acoustic inverse problems closely related with the present work. The discussion passes then to the inverse theory of the IBEM showing the main difficulties of the solution of the acoustic inverse problems.

The formal formulation of the problem addressed in this dissertation is stated in chapter 5, and the derivation of a first approach to solve this problem is also discussed. Simulation examples show the performance of the method. In addition, the analysis of factors that affect the accuracy of the inverse estimation of acoustic impedance of the surfaces is illustrated by means of test simulations on basic geometric spaces.

Chapter 6 goes trough a second alternative approach which consists of an iterative non-linear optimization process. This method showed to be more robust to noise than the least-squares method presented in chapter 5, thus numerical examples are shown in order to illustrate the differences between both approaches.

The actual experimental implementation is developed in chapter 7, and validation experiments on a real reverberation chamber are shown. Discussions on the obtained results are addressed as well.

Final conclusions and future work are presented in chapter 8.

Chapter 2

Related work

2.1 In-situ measurement of acoustic impedance

In-situ measurement methods in acoustics have been studied since around seven decades ago, and the development of effective and universally applicable techniques is still motivating new research even nowadays. The reason of this active research is the same kind of problem as the one addressed in this dissertation: the acoustic absorption coefficients or the acoustic impedance of a given geometric room is required, however the room is already constructed and samples of the materials cannot be taken to the laboratory. A well documented historical survey on in-situ measurements of acoustic absorption and impedance was written in [57], and an illustrative classification of the methods was done in [18].

One of the most widely used in-situ measurement techniques employs two microphones in a free-field space. The method consists on recording the the direct sound signals coming from a loudspeaker and the signals reflected on the test surface. Figure 2.1 shows the general set up for this method. The absorption coefficient for various angles of incidence is then computed from the transfer functions at each microphone with respect to the sound source (speaker) position. More details of the technical aspects can be found in [56]. This method has been shown to give accurate results provided that the test sample is large, homogenous, isotropic, planar, and that the reflections coming from the surrounding objects are negligible (free-field condition). For this reasons the measurements should be done in an anechoic room, or an open space, or at in a room where at the walls are far enough so as to produce reflected signals that can be eliminated by time-windowing. The method fails if unwanted reflections cannot be filtered, or non-plane wave reflections are

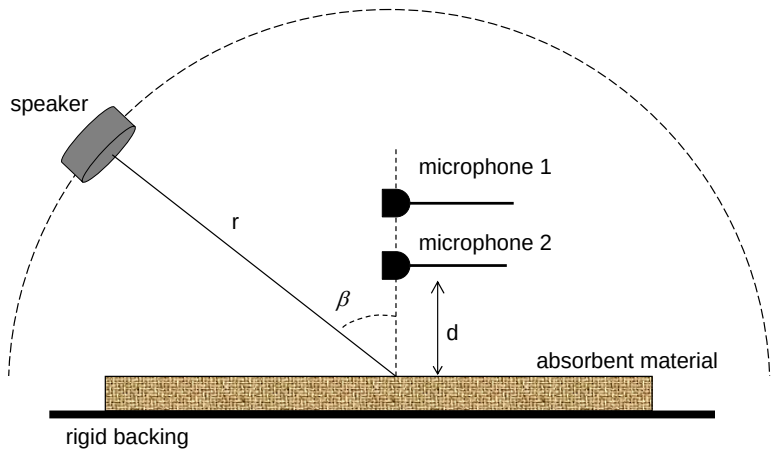

Figure 2.1: In-situ measurement of absorption coefficient by the two-microphone technique.

obtained due to the small size of the test surface, or if the surface is inhomogeneous. Yet even when the surface is homogeneous, poor accuracy at low frequencies arises if the area of the surface is not large. Therefore, while this technique is potentially accurate, its range of applicability is limited and moreover, it is inadequate for complex shape surfaces.

Another proposed approach, [52], based on the so-called *subtraction technique* allows a microphone to be placed close to the test surface. Consequently, measurements in the range 250 Hz to 8 kHz can be performed for normal incidence on plane surfaces larger than 4 m^2. In this approach the oblique incidence is compromised for low frequency accuracy. For oblique incidence and at low frequencies the method fails giving results of absorption coefficients greater than unity. This occurs because at low frequencies, other type of reflections are arisen from the edges of the test sample.

Although several improvements of former in-situ measurement techniques have been achieved, it was not until recent years that in-situ measurement techniques based on inverse acoustic numerical methods attracted the interest of researchers due to their applicability to arbitrary geometries. In such methods the underlying idea is that it is possible to reconstruct the boundary parameters of the vibro-acoustic system if there is a transfer function or a propagation model that relates the sound field with the boundaries. The reconstruction is then achieved by solving an inverse problem in the least-squares sense using samples of sound taken at reference points in the field. These kind of methods have been classified by Dutilleux et. al. [18] as stationary in-situ measurements tech-

niques. In contrast to previous work, the studies of this dissertation are based on the inverse boundary element method (IBEM) as back-propagation model for the estimation of acoustic impedance of the boundaries, which is achieved by a simultaneous calculation of the sound pressure and the particle velocity of the steady-sate vibrating surfaces of a closed geometry.

On the other hand, the idea of inverse reconstruction of surface parameters in acoustic radiation problems was widely spread with the appearance of the near-field acoustic holography (NAH)[1]. In NAH, estimation of the sound source strength is performed by placing a plane array of sensors (hologram) in the near-field of the vibrating source and using the sampled data to solve the discretized Kirchoff-Helmholtz equation. Extensive work and improvements have been done in that area, but in contrast a few researchers have recently started to tackle the inverse acoustic interior problem in which the boundary values of an enclosed space are sought given the geometry and a set of interior pressure samples. For example Kim and Ih, [38], presented an approach based on the boundary element method (BEM) for the identification of the noise sources in the interior of car panels, in which only numerical simulations are presented. A more recent work on similar problems was introduced by Dutilleux et. al., [19]. In [19], the finite element method (FEM) and the finite difference method (FDM) are used as propagation models to construct a system of linear equations which is solved by an optimization method called Evolution Strategy (ES). Numerical examples are presented showing the application of the ES method to 2D and simple 3D geometries. This is perhaps the first attempt to estimate the absorption coefficient of the surfaces in an interior space, however practical experiments with real geometries have not been reported. Although contamination of noise in the field pressures is considered in their simulations, it seems that the ES algorithm does not take into account the ill-conditioning of the linear system of equations.

Recent research work has reported that the solution of this kind of acoustic inverse problems is typically ill-conditioned, and in most cases the use of singular value decomposition (SVD) together with a regularization step is required in order to ensure an acceptable accuracy of the reconstructed boundary parameters, [65]. Indeed, because the ill-conditioning seems to be inherent to most of the inverse acoustic problems, in the present study the ill-conditioning has been also taken into account, and physically-meaning regularization techniques are proposed. The use of SVD analysis is avoided as much as possible since the computation of the SVD factorization of matrices is relatively

[1] Representative work on NAH is discussed later in chapter 4 when treating the inverse acoustic BEM.

expensive.

2.2 Inverse rendering in Computer Graphics

It is well known that some techniques of computer graphics and computer audio have been developed to complement each other towards the creation of more realistic virtual environments. A few examples of are mentioned in [23]. And in fact, the method that is proposed here was inspired by efforts of computer graphics researches trying to develop algorithms to solve the inverse problem of finding photometric parameters of a real scene, including surface reflectance properties and illumination distributions, as for instance in [5, 79, 71, 103]. There is a number of papers related to inverse rendering in computer vision and graphics. A more comprehensive survey on that work can be found in [63].

The basic idea in *inverse image rendering* is as follows: given,

1. one or more photographs of the interior space taken at selected positions,
2. the geometry of the room (including the objects contained in the scene),
3. the position of the light source and their parameters,
4. and the parametric values of the cameras,

the problem is to find the reflectance parameters of the surfaces within the scene. This problem is the reverse process of what it is usually done when creating synthetic images by a process called *Radiosity* [84], where the photometric parameters of the virtual objects to be drawn are specified by the user, and the task is to compute the light radiance values that arrive to an observer at a given view point. As an example, Figure 2.2 depicts the basic process of the inverse illumination process proposed by Yu et. al., [103]. Note however, that the method of Yu et. al. does not solve an inverse linear system as the traditional inverse acoustic problems do. The solution is instead iteratively computed by doing direct comparisons of an image synthesized using initial parameters, and an image of the real scene. If the threshold condition is not satisfied, the data is updated with the current image and new reflectance parameters are estimated. Again a new image is synthesized, compared, and so on. Although the method has not been proved theoretically, Yu et.al. found that in practice the process converges to the true estimations of the reflectance properties of the surfaces. The key point of the approach is the assumption

that the reflectance factors at each point on the surface is composed by a *specular* and a *diffuse* component, hence during the iterative process, both components can be computed separately. Furthermore, for the initial iteration, the starting guess of the reflectance factor is assumed to be a *lamberian* condition (uniform light diffusion in all direction). Once the reflectance parameters are known, Yu et. al. use them to produce synthetic images with novel lighting conditions (Figure 2.3a) and with inserted virtual objects (Figure 2.3b).

Let us further note that, such inverse illumination approaches suggest the possibility to propose an analogy between inverse light rendering techniques and inverse acoustic methods. And that in principle, some ideas of inverse illumination can be brought to specific acoustic inverse problems where similar goals are pursue. For example, one can observe that in its basic form the Radiosity method [84](in which some image rendering techniques are based) is a particular case of the boundary element method widely used in acoustics and other areas. Therefore, one may import ideas from inverse illumination, for example the assumption of homogenous distribution of surface parameters on each interior surface and bring it to the inverse problem targeted in the present work in order to improve the accuracy of the sought solution. This idea is discussed with more detail in further sections.

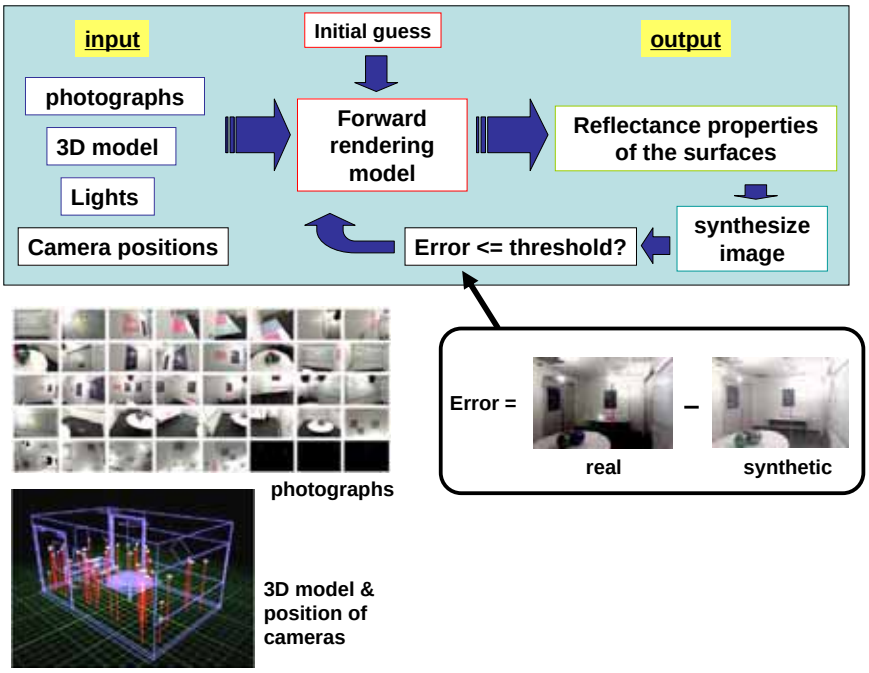

Figure 2.2: Inverse illumination process proposed by Yu et. al.,[103].

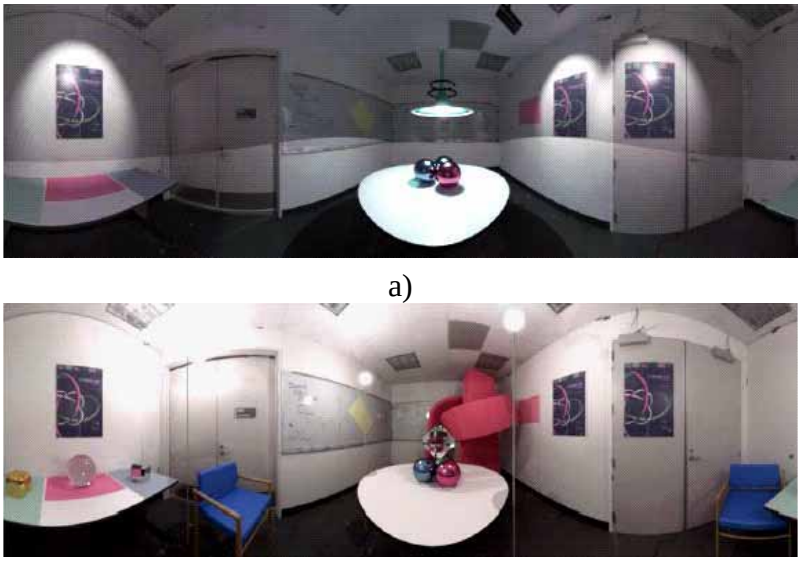

a)

b)

Figure 2.3: Results of the inverse illumination approach of Yu et. al.,[103]. a) Synthesized image with new lighting conditions. b) Synthesized image where seven new virtual objects have been inserted.

Chapter 3

Prediction of sound in interior fields by the acoustic BEM

The Boundary Element Method (BEM) is a powerful numerical tool primarily developed for the solution of complex boundary integral problems. Since its appearance in the literature (1977), it attracted the attention of a number of researchers because of its intrinsic advantages over its counter part, the Finite Element Method (FEM), which attempts to solve the wave propagation in the complete domain, while in contrast the BEM reduces the solution of the wave equation to a surface integral problem that can be solved by considering only the boundary conditions at the domain limits. Once the solution at the boundaries is known, it is possible to derive expressions that relates parameter values in the domain with parameter values at the boundaries. Because of this capability, the BEM has been adopted as the acoustic analysis tool for the purposes of this research work.

This chapter introduces the theoretical foundations of the acoustic BEM that are used for the analysis of sound fields in a time-harmonic domain. And the equations derived here form the bases for the subsequent development of the inverse BEM theory applied to the estimation of acoustic impedance from sound field measurements. On the other hand, most of the equations and conventions for the implementation of the BEM software in this work have been aligned to those suggested in [97]. Moreover, because only the analysis of sound propagation in interior acoustic fields is of particular interest, the general case applied to exterior problems will be skipped, however there is a variety of implementations documented in the literature of the BEM theory (e.g. [11, 44, 101]) that may suite those specific problems.

3.1 Theoretical background

3.1.1 The Helmholtz equation and the fundamental solution

Consider a closed boundary S of arbitrary shape immersed in a domain Γ in a 3D space filled with a compressible fluid of density ρ. For a time–harmonic wave that propagates in Γ, the sound pressure p at any place in the domain satisfies the Helmholtz equation

$$\nabla^2 p + \mathrm{k}^2 p = q, \tag{3.1}$$

where q is a volume sound source and the wave number $\mathrm{k} = \omega/c$ defines the relationship between the frequency ω and the velocity of propagation c of the wave. Note that the time–dependent term $e^{j\omega t}$, with $j = \sqrt{-1}$ the imaginary unit and t the time, does not appear since (3.1) expresses the wave propagation in steady–state. Furthermore, the sound pressure p is related to the particle velocity v_{n} by

$$\frac{\partial p}{\partial \mathrm{n}} = -j\rho v_{\mathrm{n}}, \tag{3.2}$$

denoting n the normal component of the direction of propagation. The presence of S imposes constraints to the wave propagation at the boundaries whose conditions can be specified by three types:

$$\begin{array}{ll} 1.\ \text{Dirichlet} & p = \overline{p} \\ 2.\ \text{Neumann} & v_\mu = \overline{v_{\mathrm{n}}} \\ 3.\ \text{Robin (or mixed)} & Z = \frac{p}{v_{\mathrm{n}}} \end{array} \tag{3.3}$$

For a partition S, such that $S = S_p \cup S_v \cup S_Z$, only one boundary condition from the above types is prescribed. On the other hand, when q is a point source radiating a sound of frequency ω, the sound field G in free space is obtained by solving the Helmholtz equation

$$\nabla^2 \mathrm{G} + \mathrm{k}^2 \mathrm{G} = \delta(\mathbf{r}_{\mathrm{P}} - \mathbf{r}_{\mathrm{Q}}), \tag{3.4}$$

where the a fundamental solution G is given by the Green's function as

$$\mathrm{G}(r, \omega) = \frac{e^{-j\mathrm{k}r}}{4\pi r}, \tag{3.5}$$

where $r = |\mathbf{r}_{\mathrm{P}} - \mathbf{r}_{\mathrm{Q}}|$ is the distance between a source point Q and a receiver point P. It is worth to make the observation here that expression (3.5) indicates that the complex amplitude of the propagating wave fades exponentially as the receiver point goes faraway

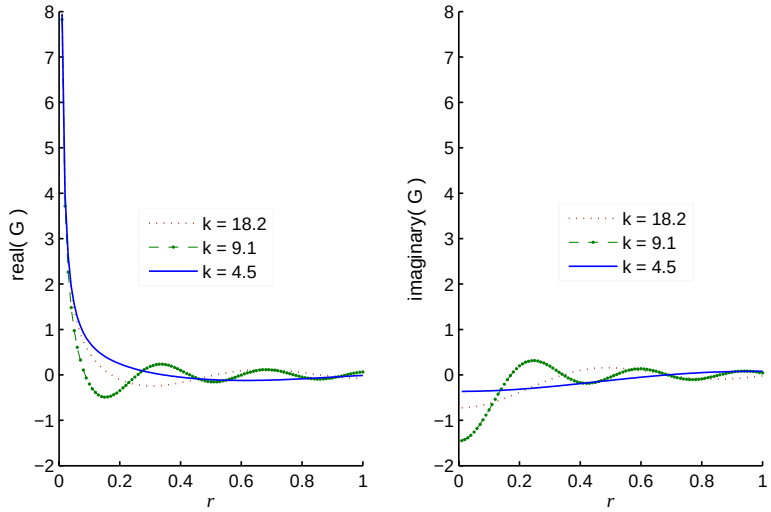

Figure 3.1: Exponential behavior of the Green's function.

from the source point, as illustrated in the example of Figure 3.1. This fact will help to discuss the physical interpretation of one of the difficulties of the inverse BEM presented in further sections.

If the sound pressure is to be calculated at some point P in the domain Γ, the Helmholtz equation (3.1) has to be solved subjected to the boundary conditions (b.c.) given in (3.3). This can be achieved by restating equation (3.1) in an equivalent form using the second Green's identity

$$\int_V (\alpha\partial_{\mathrm{ii}}\beta - \beta\partial_{\mathrm{ii}}\alpha)\, dV = \oint_S (\alpha\partial_{\mathrm{n}}\beta - \beta\partial_{\mathrm{n}}\alpha)\, dS, \tag{3.6}$$

which yields to the formulation of the so-called *Helmholtz integral equation* for three different cases: 1) P inside the closed surface S, 2) P on the boundary S, and 3) P outside S. In the subsequent discussion only the first two cases will be addressed.

3.1.2 Direct formulation of the acoustic BEM for interior fields

Let us consider now the case in which the domain Γ is inside the boundary defined by an arbitrary geometry S in a 3D space, as depicted in Figure 3.2. The vector $\mathbf{n}$ normal to the surface at every place of S is assumed to point out of the domain of interest. With a volume source q located somewhere in the interior field, and boundary conditions given by (3.3) prescribed in the partitions S_p, S_v, and S_Z respectively, the field pressure p_f at

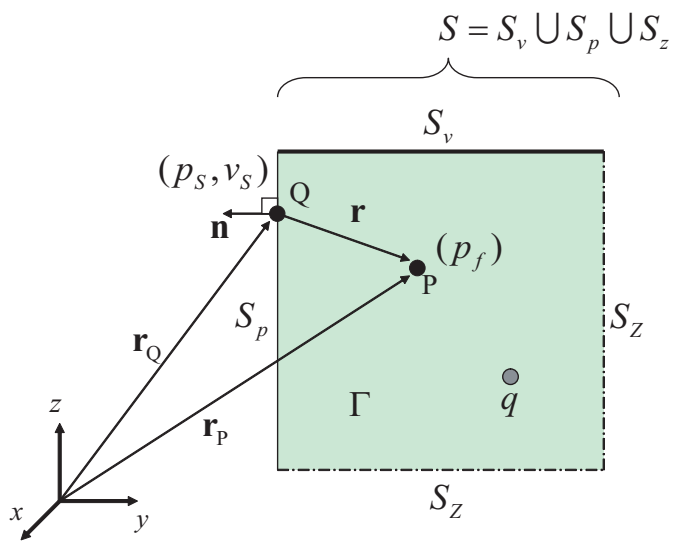

Figure 3.2: The interior case of the acoustic BEM.

the point P is to be determined.

As stated before, by applying the Green's identity (3.6) to the Helmholtz equation (3.1) and following the derivations suggested in [97], the Helmholtz integral equation for an interior field (also known as the *Kirchhoff–Helmholtz* equation) is expressed as

$$C_{\mathrm{P}} p(\mathbf{r}) + \oint_S (p\partial_{\mathrm{n}}\mathrm{G} + j\rho\omega\mathrm{G}v_{\mathrm{n}})\, dS + \int_V \mathrm{G}q\, dV = 0, \tag{3.7}$$

where ∂_{n} denotes partial derivative with respect to the normal, and C_{P} is a constant defined by

$$C_{\mathrm{P}} = \frac{1}{4\pi} \int_\alpha \sin\theta\, d\theta\, d\phi, \tag{3.8}$$

being α the equivalent solid angle in which P sees the surface S. For the special cases when P is in the interior field, $C_{\mathrm{P}} = 1$, and if P lies on a smooth surface $C_{\mathrm{P}} = \frac{1}{2}$. Moreover, if the geometry S is a cube $C_{\mathrm{P}} = \frac{1}{4}$ for P lying on the edges, and $\frac{1}{8}$ when P is on a corner.

It can be shown (see for example [97]) that when the b.c. are specified the sound pressure p_S and the normal particle velocity v_S on the surface S can be readily known, and the sound pressure p_f in the field is obtained by

$$C_P\, p_f(\mathbf{r}) = -\oint_S (p_S\partial_{\mathrm{n}}\mathrm{G} + j\rho\omega\mathrm{G}v_S)\, dS - \int_V \mathrm{G}q\, dV. \tag{3.9}$$

Note that in (3.7) and (3.9) the dependence of G on r and ω has been omitted for ease of

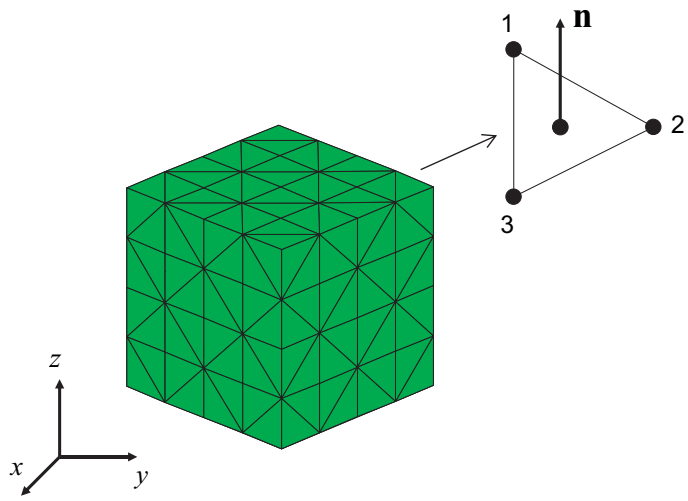

Figure 3.3: Discretization of the surface S. Example of a cube mesh.

notation, and that the partial derivative of G respect to the normal is

$$\frac{\partial \mathrm{G}}{\partial \mathrm{n}} = \frac{\partial \mathrm{G}}{\partial \mathrm{r}} \frac{\partial \mathrm{r}}{\partial \mathrm{n}} = -\frac{1 + j\mathrm{k}r}{4\pi r^2} e^{-j\mathrm{k}r} \left(\frac{\mathbf{r} \cdot \mathbf{n}}{|\mathbf{r}|} \right) \tag{3.10}$$

3.2 Implementation of the acoustic BEM

3.2.1 The discrete formulation of the Helmholtz integral equation

The solution of the integral equation (3.7) is not straight forward. An exact solution is difficult to achieve without making use of numerical techniques, and even the solution obtained by these is an approximation to the original one. Additionally, since the calculations are to be made by computer systems, the integral equations have to be restated in a discrete form.

Let us consider an example in which the geometry of S is a cube whose surface has been broken into N boundary elements as shown in Figure 3.3. In general, the shape of the elements can be quadrangles, triangles, or any shape that suites the problem, however in what follows, only triangular elements will be assumed. Additionally, the nodes of each element are numbered in such a way that the normal **n** points to the exterior of the mesh.

The discretization of the surface S makes necessary the introduction of an interpolation function Ψ between the nodes of the elements in the mesh. This interpolation can

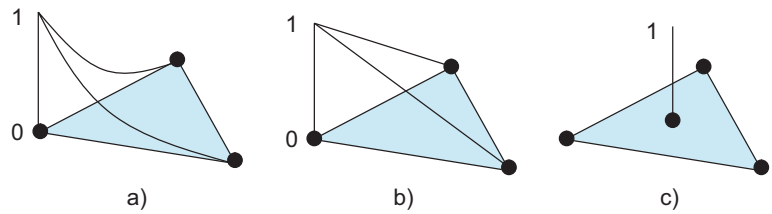

Figure 3.4: Interpolation functions: a) quadratic, b) linear, c) isoparametric.

be linear, quadratic or of higher order, yielding the following definitions of the sound pressure p_s and normal velocity v_s at any point in the surface s of a single element:

$$\begin{aligned} p_s &= \sum_l \Psi_l p_l, \\ v_s &= \sum_l \Psi_l v_l, \end{aligned} \tag{3.11}$$

where p_l and v_l are the pressure and normal particle velocity at the l–th node of the element. Figure 3.4 illustrates examples of interpolation functions. Introduction of the interpolations (3.11) into (3.7) gives therefore

$$C_{\mathrm{P}} p(\mathbf{r}) + \sum_{k=1}^{N} \int_{\mathrm{s}_k} \left(\left(\sum_l \Psi_l p_l \right) \partial_{\mathrm{n}} \mathrm{G} + j\rho\omega \mathrm{G} \left(\sum_l \Psi_l v_l \right) \right) ds + \int_V \mathrm{G} q \, dV = 0. \tag{3.12}$$

Furthermore, since an isoparametric interpolation and one node per element (at the centroid) are considered in this work, Ψ can be set to unity yielding the expression

$$C_{\mathrm{P}} p(\mathbf{r}) + \sum_{k=1}^{N} p_{s_k} \int_{\mathrm{s}_k} \partial_{\mathrm{n}} \mathrm{G} \, ds + j\rho\omega \sum_{k=1}^{N} v_{s_k} \int_{\mathrm{s}_k} \mathrm{G} \, ds + \int_V \mathrm{G} q \, dV = 0. \tag{3.13}$$

Let us define the operators

$$\begin{aligned} a_k &= \int_{\mathrm{s}_k} \partial_{\mathrm{n}} \mathrm{G} \, ds_k, \\ b_k &= -j\rho\omega \int_{\mathrm{s}_k} \mathrm{G} \, ds_k, \\ \widehat{q} &= \int_V \mathrm{G} q \, dV, \end{aligned} \tag{3.14}$$

using the above operators the discrete equation (3.13) can be written as

$$C_{\mathrm{P}} p(\mathbf{r}) + \sum_{k=1}^{N} p_{s_k} a_k - \sum_{k=1}^{N} v_{s_k} b_k + \widehat{q} = 0. \tag{3.15}$$

Now, when a set of M points in the field is considered, the sound pressure p_{f_i} at the i–th point is given by

$$p_{f_i} = -\sum_{k=1}^{N} p_{s_k} a_{i,k} + \sum_{k=1}^{N} v_{s_k} b_{i,k} - \widehat{q}_i \tag{3.16}$$

with $i = 1, 2, ..., M$. Last equation can be expressed in a matrix form arriving finally to

$$\mathbf{p}_f = -\mathbf{A}\ \mathbf{p}_S + \mathbf{B}\ \mathbf{v}_S - \widehat{\mathbf{q}}. \tag{3.17}$$

Notice that since the elements of the matrices $\mathbf{A}$ and $\mathbf{B}$ depend only on the geometry and the position of the M field points, they can be readily computed in advance and stored in memory. If in addition the boundary parameters $\mathbf{p}_s$ and $\mathbf{v}_s$ together with the sound source $\widehat{\mathbf{q}}$ are also known, then the field pressures $\mathbf{p}_f$ can be determined. In practice however, only one parameter of the boundary conditions is usually specified. The missing parameters should be found by solving the discrete integral equations.

3.2.2 Solution of the boundary parameters

When the boundary conditions (3.3) are prescribed to each type of surface partition (as it was illustrated in Figure 3.2) one of the boundary parameters (either p_s or v_s) is known at each element. Therefore, the equation (3.17) is an equation with two unknowns, namely $\mathbf{p}_f$ and $\mathbf{p}_s$ or $\mathbf{v}_s$. In order to solve the discrete integral equation (3.17) for the unknown parameters, the so-called *collocation technique* is applied as follwos: suppose that the M field points of $\mathbf{p}_f$ are placed not in the interior field but on the boundary S. Moreover, the locations are chosen to coincide with the nodes of the mesh (which are assumed to be located at smooth areas of S). Under that situation the number of M field points (now on the surface) becomes equal to N, $\mathbf{p}_f$ is included in $\mathbf{p}_s$, and the equation (3.17) is rewritten as

$$(\mathbf{A} + \frac{1}{2}\mathbf{\Delta})\mathbf{p}_S - \mathbf{B}\ \mathbf{v}_S = -\ \widehat{\mathbf{q}}, \tag{3.18}$$

where $\mathbf{\Delta}$ is a diagonal matrix whose entries are $\delta_{ik} = 1$ if $i = k$, and $\delta_{ik} = 0$ otherwise. For what follows, the influence matrices $\mathbf{A}_S$ and $\mathbf{B}_S$ will be introduce to denote the matrices $\mathbf{A}$ and $\mathbf{B}$ when the collocation points are placed on the nodes of the mesh. Additionally the notation $\mathbf{A}_S = (\mathbf{A} + \frac{1}{2}\mathbf{\Delta})$ will be adopted. Thus, equation (3.13) is now

$$\mathbf{A}_S\ \mathbf{p}_S - \mathbf{B}_S\ \mathbf{v}_S = -\ \widehat{\mathbf{q}}, \tag{3.19}$$

After one of the parameters is user-specified as boundary condition, the equation (3.18) is solved for the missing parameter. For example, if values of $\mathbf{v}_S$ are imposed at each surface element, then $\mathbf{p}_S$ can be obtained by solving the linear system of equations

$$\mathbf{A}_S\, \mathbf{p}_S = \mathbf{d}, \tag{3.20}$$

where

$$\mathbf{d} = \mathbf{B}_S\, \mathbf{v}_S - \widehat{\mathbf{q}}. \tag{3.21}$$

3.2.3 Impedance boundaries

When impedance boundaries are imposed at the boundaries, the relation

$$Z_s = \frac{p_s}{v_s} \tag{3.22}$$

is used to solve the system of equations (3.20). For example, if the surface pressures $\mathbf{p}_S$ are to be determined, the velocities $\mathbf{v}_S$ in (3.18) are substituted by the impedance values, and the coefficients of the matrix $\mathbf{B}_S$ are computed as follows:

$$b_{ik} = -j\rho\omega \int_{s_k} \frac{\mathrm{G}_{ik}}{Z_{s_k}}\, ds_k. \tag{3.23}$$

The matrix equation (3.18) is then rewritten as

$$(\mathbf{A}_S + \mathbf{B}_S)\mathbf{p}_S = -\,\widehat{\mathbf{q}}, \tag{3.24}$$

and $\mathbf{p}_S$ can be readily found by solving the system of equations (3.24).

3.2.4 Computational cost

One of the strongest drawbacks of the BEM is the computational cost. The matrices $\mathbf{A}_S$ and $\mathbf{B}_S$ of the equation (3.19) are complex and fulled populated, and need to be stored in memory in order to solve for the boundary conditions. Therefore, the memory requirements are dominated by the size of there matrices. For example, for an acoustic problem with a mesh of N nodes the memory required to store the matrices with complex double precision is of the order $\approx 2(N^2) \times (16 \text{ bytes})$. Figure 3.5 shows the increase of memory with the number of nodes. Furthermore, if the analysis of the acoustic problem has to be made over a range of frequencies, the time of computation is increased considerably since the BEM matrices have to be recomputed for each frequency step. Although several

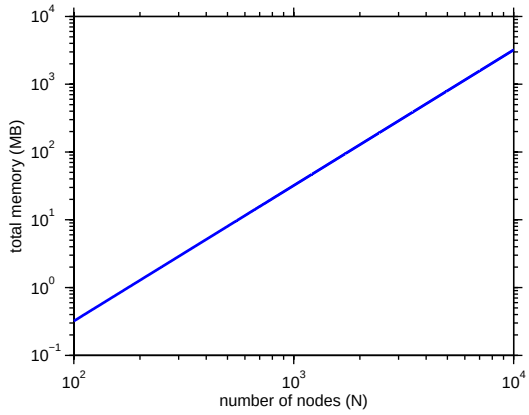

Figure 3.5: Memory requirements for the storage of the BEM matrices.

techniques to speed up the calculations have been suggested , accuracy in the results has been given priority in the present work and no speed up optimization is applied. The use of interpolation and approximation techniques to speed up the computation time results in an increase of round off errors that will affect the solution of the inverse problem of acoustic impedance estimation as will be discussed later.

3.3 Validation of the acoustic BEM software

3.3.1 Test problems from a benchmark platform

When developing a numerical analysis software such as BEM, it is important to make proper tests in order to confirm the effectiveness of the implementation. And thus it is usually a reasonable idea to carry out comparisons with results obtained with other software programs that have been already validated by extensive experimentation. For these purposes there are some standard acoustic problems suggested in [3] that serve as a reference for the benchmark of computational methods in architectural and environmental acoustics.

The test problems proposed in [3] are divided in three categories according to the geometric place of analysis: *exterior*, *interior* and *structural-acoustic*. Each of them containing *basic* geometry problems and more complex geometries such as in *practical* situations, e.g. loudspeakers, barriers, halls, etc. Directions for the tasks of the problems are addressed in the time and frequency domain taking as basis the parameters indicated

Category	Geometry type	Frequency domain	Time domain
Exterior	basic	Steady-state	Impulse response
	practical		
Interior	basic		
	practical		
Structural-acoustic	basic		
	practical		

Table 3.1: Categories of the benchmark problems suggested in [3].

in each problem. Table 3.1 summarizes the categories of the benchmark problems, and details for each problem can be accessed at [3].

On the other hand the problem considered for the validation of the BEM implementation presented in the previous sections is the benchmark problem B0–1F which belongs to the category *interior* and *basic* geometry type (a unit cube). The analysis is performed in the frequency domain and two tasks are proposed. Figure 3.6 depicts the geometry of the problem, and the details are described in the following paragraphs.

Problem B0–1F

Geometry

A unit cube (1m$\times$1m$\times$1m) with its center in the origin (0, 0, 0).

Boundary conditions

Rigid boundaries (particle velocity $=$ 0) in all the faces. A punctual source located in the origin and vibrating harmonically at a frequency ω with a volume acceleration amplitude of $1\mathrm{m}^3/\mathrm{s}^2$.

Task A

Compute the sound pressure amplitude at 101 points (marked as R1) which lay on the line $x = 0, z = 0.5$, and are apart from each other at intervals of 0.01 m ($y = -0.5, ..., 0.5$). The analysis frequencies are 31.5, 63, 125, 250, 500, 1k, 2k, and 4k Hz.

Task B

Compute the sound pressure amplitude at three points R2(0.5, 0.5, -0.5), R3(0, 0.5,

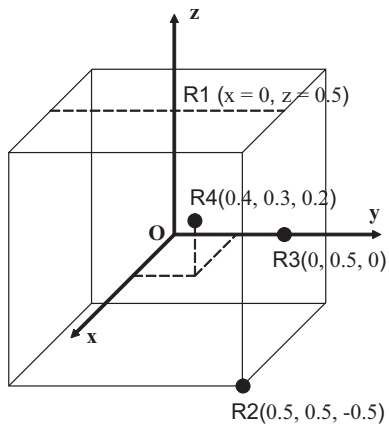

Figure 3.6: Geometry of the benchmark problem B0–1F.

0) and R4(0.4, 0.3, 0.2), in the range of frequencies from 20Hz to 4kHz at intervals of 10Hz.

3.3.2 Results from the simulations for the test problems

In the validation process with the benchmark problems described before, the following general assumptions are considered:

- Velocity of sound in air (at 20° C), $c = 343.7\ \mathrm{m/s}$.
- Density of air (at 20° C), $\rho = 1.21\ \mathrm{kg/m^3}$.
- Six elements per wavelength for the size of the boundary elements, i.e.:

$$\text{max. size of element} = \frac{\lambda}{6} \tag{3.25}$$

Although a range of frequencies from 20 Hz to 4 kHz is indicated in the above problems, here the range is limited to the band from 20 Hz to 1 kHz, which is enough for the validation purposes of this work since most of the analyses presented in the next sections are within this range.

For the task A of the problem B0–1F the sound pressure is computed at a set of 101 points that lay on one of the sides of the cube. The results of the simulations for this

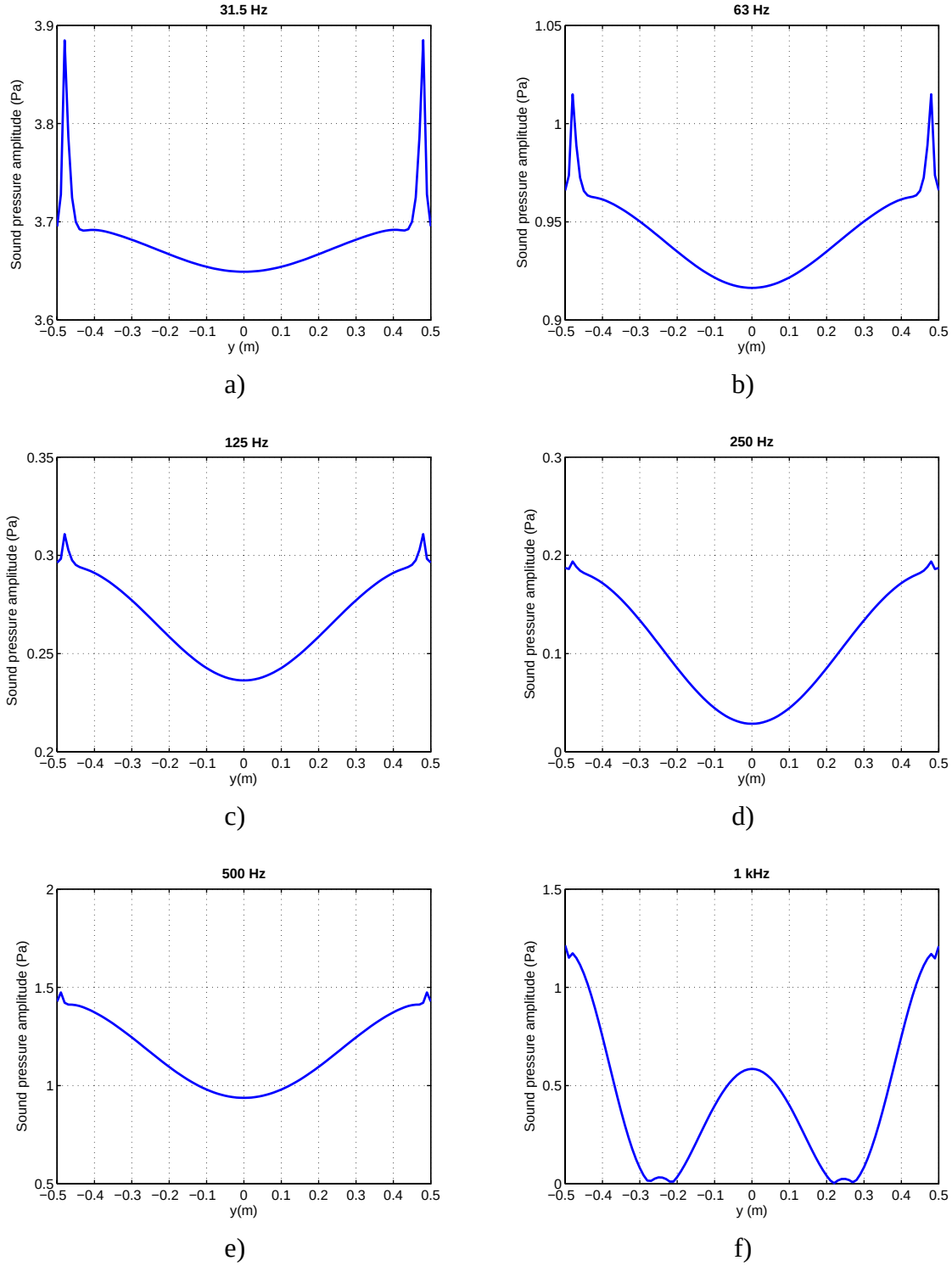

Figure 3.7: Results of the simulations, benchmark problem B0–1F task A, using the BEM implementation presented in this work.

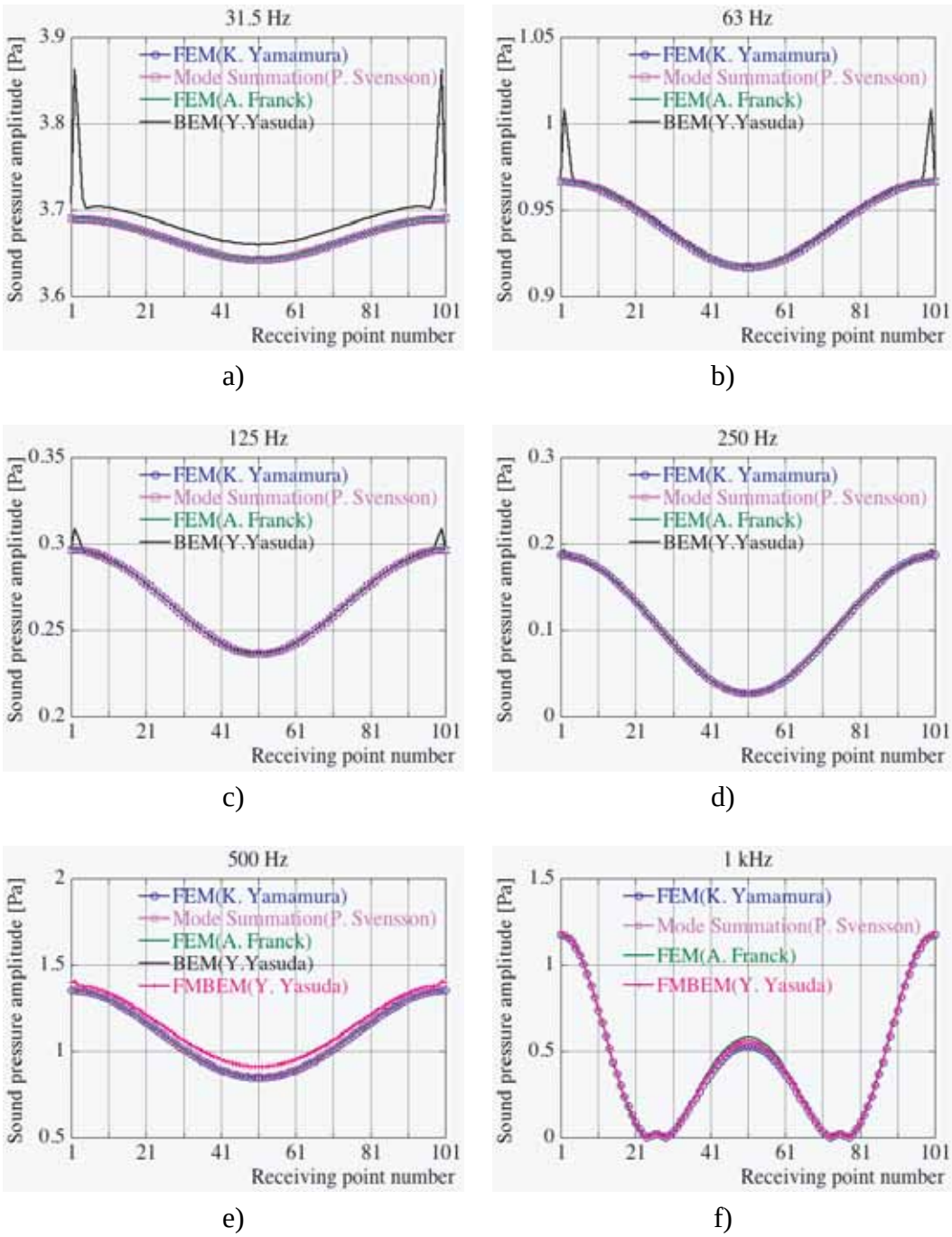

Figure 3.8: Results taken from [3] for the benchmark problem B0–1F task A contributed by other users, shown here for comparison purpose. Note that the receiving points are numbered so that point 1 corresponds to $y(m) = -0.5$, and point 101 corresponds to $y(m) = 0.5$.

task are shown in Figure 3.7. Note that these sound pressure levels at each frequency are in complete agreement with the results obtained by other contributors to the same benchmark problem in [3].

Similarly, the simulations for the task B of the problem B0–1F are performed. This time the sound pressure is computed at three points that lay on one side, in the interior, and at one corner of the cube. For each of these points the sound pressure amplitude is shown in Figure 3.9. The frequency step of the analysis is 10 Hz, covering the band of 20–1 kHz.

Summary of the benchmark tests

It is important to perform evaluations of the effectiveness of the BEM implementation since further numerical analysis are based on the software implemented. For the purpose of comparisons of results, the benchmark problems proposed in [3] are a useful reference point since the problem start with simple geometrical situations with basic boundary conditions that can be immediately confirmed with analytical solutions (in addition to the available results obtained by other contributors). Finally, the results performed with the acoustic BEM implementation discussed in previous sections show agreement with the reference solutions and therefore its reliability for future analysis is confirmed.

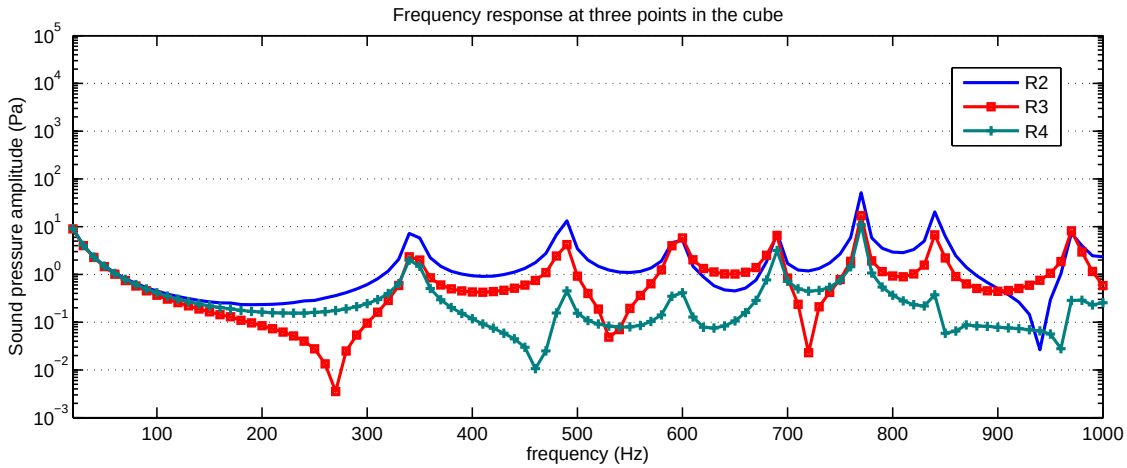

Figure 3.9: Results of the simulations, benchmark problem B0–1F task B, using the BEM implementation presented in this work. Frequency resolution: 10 Hz steps.

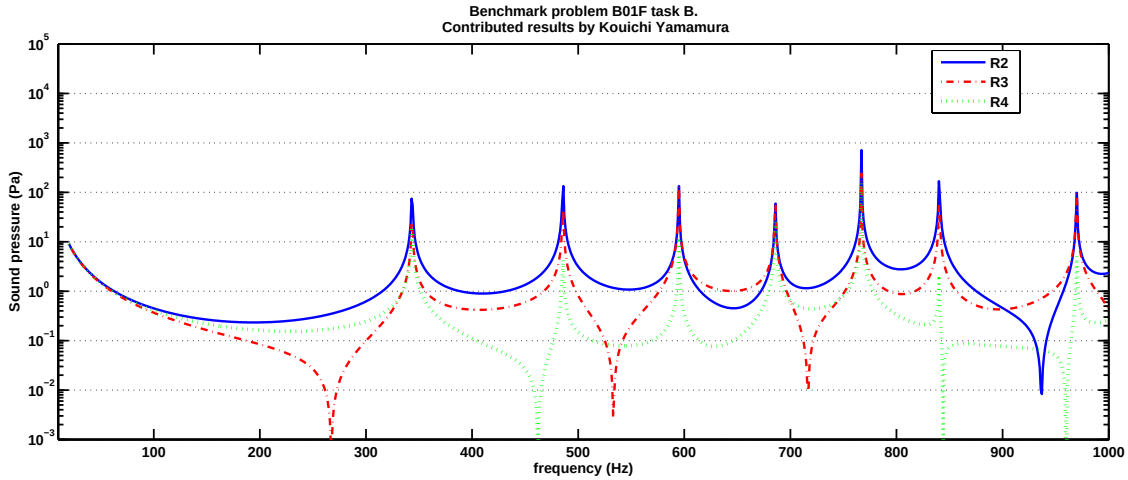

Figure 3.10: Results taken from [3] for the benchmark problem B0–1F task B contributed by other users, shown here for comparison purpose. Frequency resolution: 1 Hz steps.

Chapter 4

Acoustic parameter estimation by Inverse BEM

The forward prediction of sound field by BEM is important because it gives us a preview of the approximated values that we would expect when passing to the experimental part. Moreover, the importance of the correct implementation of a BEM software resides in that it provides the bases for the formulation of the inverse process. For these reasons the fundamentals of the BEM were readily introduced in the previous chapter, and its practical implementation was also demonstrated by using benchmark simulation problems. It is convenient now to introduce the theory of the inverse acoustic problems that are based on the BEM. As it will be noted, the equations of the inverse BEM derived here represent the fundamental form not only of the inverse problem addressed in this dissertation but also of other problems studied in previous work. Therefore, as an illustrative background a brief review of the existent research on the area of inverse acoustic problems will be presented. And again, some of the formulae in this chapter will serve as the starting point for further study of the estimation of acoustic impedance by inverse BEM – problem that will be formally defined in the next chapter.

4.1 Background on the acoustic parameter estimation by inverse mehtods

Acoustic parameter estimation has been studied in many areas of Acoustics, and the methods to assess these parameters vary according to the application. Traditionally, parameters such as sound pressure, particle velocity, absorption factor, acoustic impedance, etc., are

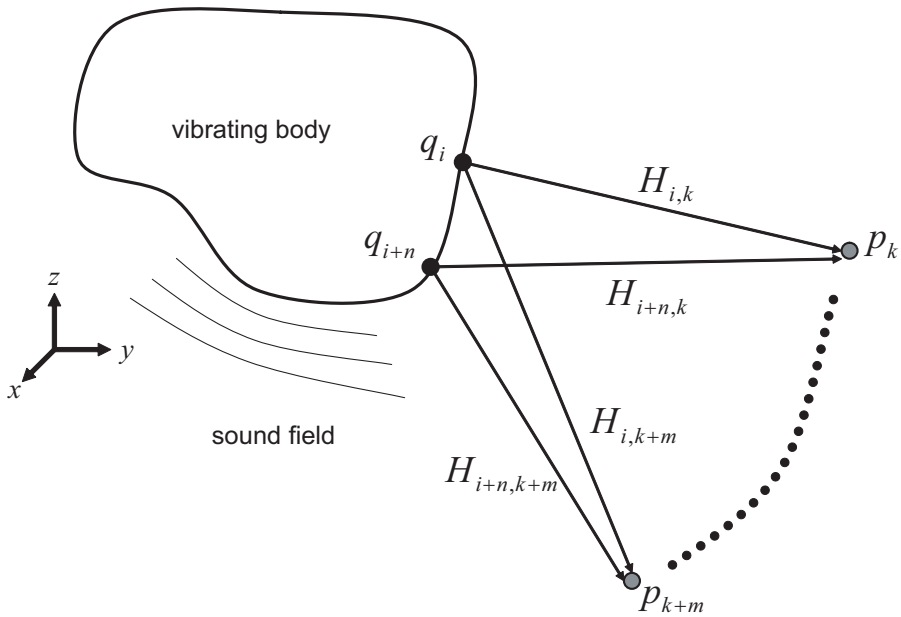

Figure 4.1: Example of an exterior inverse acoustic problem.

measured directly in controlled experimental conditions using specialized devices, but in recent decades the assessment of acoustic parameters of vibrating objects has been attempted from measurements of samples of the acoustic field that these objects produce. Approaches of this kind are known as *inverse acoustic methods*. In such methods the underlying idea is that it is possible to reconstruct the boundary parameters of the vibro-acoustic system if there is a transfer function or a propagation model that relates the sound field with the acoustic parameters at the boundaries, i.e. the surface of the vibrating body. Figure 4.1 shows an example of this idea applied to a sound radiation problem in the exterior field. The surface of the object is usually represented as a number of discrete independent sound sources q_i's (with $i = 1, \ldots, n$). By taking a number of measurements p_k's (with $k = 1, \ldots, m$) in the sound field and using the propagation model adopted, a matrix **H** of the transfer functions $H_{i,k}$'s is obtained, and the acoustic system can then be expressed as a linear system of equations:

$$\mathbf{p} = \mathbf{H}\,\mathbf{q}. \tag{4.1}$$

The back estimation of the sought acoustic parameters at the surface is then achieved by solving the inverse problem in the least-squares sense using the samples of sound taken at the reference points in the field:

$$\mathbf{q} = \mathbf{H}^{-1}\,\mathbf{p}. \tag{4.2}$$

The above approach is in principle applicable to any arbitrary geometry as long as the transfer matrix **H** does not represent coefficients of the Rayleigh integral form (see [97]) and the source surface is model with sufficient discrete source elements.

Perhaps the most widely studied inverse acoustic problem of the type of the technique described above is that of the localization of a sound source in relation to an array of microphones. More specifically, the estimation of the strength of acoustic sources given a number of measurements of their radiated field. A number of variations of this approach have been proposed, however the idea of inverse reconstruction of surface parameters in acoustic radiation problems was widely spread with the appearance of the Near-field Acoustic Holography (NAH) technique, introduced by Maynard *et. al.*, [50],[94], and subsequently followed by other researchers on that subject, e.g. [6][27][2]. In NAH, estimation of the sound source strength is performed by placing a plane array of sensors (hologram) in the near-field of the vibrating source and using the sampled data to solve the discretized Kirchoff-Helmholtz equation. A detailed implementation of the NAH was published in [95] and a discussion of its practical use is presented in [27] and [28]. A good theoretical background on the NAH in the spatial Fourier Transform domain can be found in [99]. Formulations of NAH based on the BEM started to appear in the 1990's, e.g. [2, 40, 88], and more continued recently by a number of researchers, [92, 39, 16].

On the other hand, precise experiments on the estimation of acoustic source strength were reported in by Nelson and Yoon [54, 55], where they attempt to recover the volume velocities of a vibrating flat plate mounted on an infinite baffle, and tanking measurements in the near-field generated by the plate with a linear array of microphones that move forming a plane close to the plane of the source. Nelson and Yoo also investigated the effects of the placement of the microphone array over the accuracy of the reconstruction of the source strength. They conclude that for an optimal estimation of the surface parameters in their experiments, the positioning of the microphone array should be close to the reconstruction surface and following the distribution of the discretizing source elements. This conditions seem to be necessary for a satisfactory reconstruction of the source strengths when the method employed is a spatial Fourier Transform–based NAH for an exterior radiation problem. This results are in complete agreement with the fact that in free space the pressure level of the sound waves decay rapidly as the receiving point moves away from the source (this effect was discussed in chapter 2). Similar findings have been made by other workers on the area, e.g. [39, 92], but for the case of an interior field using BEM–based NAH. In spite of these important conclusions, an optimal placement of a fixed

microphone array is still hard to achieve when dealing with complex geometries (situation that usually arises in real practical applications). For instance, in a problem such as that addressed in the present work, where geometries of realistic indoors are considered, a large–scale microphone array following the shape of the interior would be difficult to implement due to the presence of unaccessible areas. A suggested approach in that case would be to perform measurements of the sound field trying to cover the interior volume space as much as possible, and indeed more information about the sound field created by the geometry and the boundary conditions is collected. For this reason (and for the purpose of this work), further chapters will introduce a novel measurement technique which allows the measurement of sound samples in real-time while using one microphone that can be moved in a total random way.

4.2 Theory of the inverse BEM–based parameter reconstruction

One of the main reasons to prefer parameter estimation methods based on the Inverse BEM is the fact that they can be used for practically any arbitrary geometry and do not require a cumbersome and expensive measurement procedure, making them suitable for the reconstruction of velocity distribution of sound sources (radiation problems). A number of experiments have been discussed already in the previous section. This kind of problems is of most relevance to engineers who try to get a better insight of the nature of the sound source in order to control noise levels. Nevertheless, for the present work of particular interest in the development of an inverse method based on the inverse BEM that can be used to estimate the acoustic impedances of the surfaces. Therefore the following formulation will consider the application of the inverse BEM to an interior problem, which is basically the same formulation as the radiation case. Readers interested on details of the reconstruction of source velocities in exterior problem, are referred to [54, 97].

From the mathematical point of view, the inverse BEM is a procedure in which the solution to the governing integro–differential equations is known and the corresponding boundary conditions (B.C.) are sought, (in contrast to the forward BEM that gives an approximate solution of the sound field for specified B.C.). Let us start by considering a sound field inside an enclosed surface S as depicted in Figure 4.2. It was studied in a

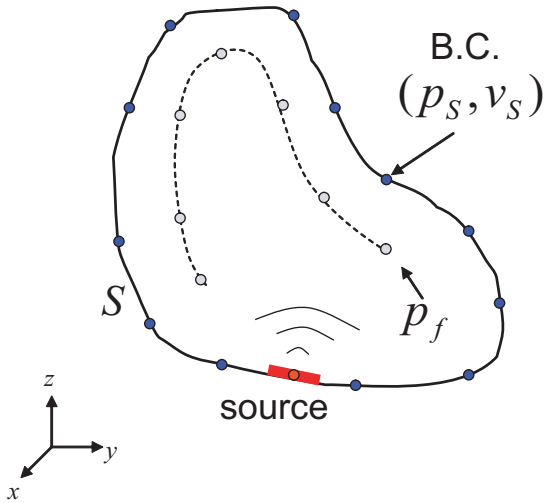

Figure 4.2: Inverse BEM in an interior problem.

previous chapter that the basic Helmholtz integral equation

$$\oint_S (p_S \frac{\partial \mathrm{G}}{\partial n} + j\omega\rho \mathrm{G}\, v_S)\, dS = -p_f, \tag{4.3}$$

describes the relationship between the sound pressure p_f at any point in the field with the surface boundary parameters p_S and v_S. Differing from the formulations for an interior BEM derived in chapter 3, it is assumed now that the sound source is some vibrating area of the closed surface[1]. Note that in practice p_f represents the sound pressure directly measured from the sound field. Therefore, as discussed in chapter 3, if a set of sound pressures p_f are measured at M points in the field and the surface S is discretized into N elements (indicated with dots in Figure 4.2), the following system of equations can be written

$$\sum_{k=1}^{N} p_{s_k} a_{i,k} - \sum_{k=1}^{N} v_{s_k} b_{i,k} = -p_{f_i}, \tag{4.4}$$

with $i = 1, 2, ..., M$. The coefficients $a_{i,k}$'s and $b_{i,k}$'s are defined as in (3.14). In matrix form

$$\mathbf{A}_f\, \mathbf{p}_s - \mathbf{B}_f\, \mathbf{v}_s = -\, \mathbf{p}_f, \tag{4.5}$$

where the vector $\mathbf{p}_f$ is now the set of measured pressures along a path in the farfield, e.g. as illustrated in Figure 4.2, and the elements of the matrices $\mathbf{A}_f$ and $\mathbf{B}_f$ are the BEM

[1]The consideration of a punctual sound source was dropped here since it is difficult to be achieved in practical applications

coefficients at the field points. It was also seen in chapter 3 that placing the measurement points on the surface (i.e. matching the nodal points of the mesh), the following expression holds:

$$\oint_S (p_S \frac{\partial \mathrm{G}}{\partial n} + j\omega\rho \mathrm{G}\, v_S)\, dS = -\frac{p_S}{2}. \tag{4.6}$$

It is assumed that the nodal points are located at smooth areas of the surface S, thus the $1/2$ factor in the right hand side of (4.6). From the last equation, and without going into details of the discretization of (4.6)(see chapter 3 section 3.2.2), the matrix equation bellow is satisfied when the measurement points are at the surface S:

$$\mathbf{A}_s\, \mathbf{p}_s - \mathbf{B}_s\, \mathbf{v}_s = 0. \tag{4.7}$$

It is readily noted that (4.7) and (4.5) form another system of equations, namely

$$\begin{array}{rcl} \mathbf{A}_s\, \mathbf{p}_s - \mathbf{B}_s\, \mathbf{v}_s & = & 0 \\ \mathbf{A}_f\, \mathbf{p}_s - \mathbf{B}_f\, \mathbf{v}_s & = & -\,\mathbf{p}_f, \end{array} \tag{4.8}$$

with unknown acoustic parameters $\mathbf{p}_S$ and $\mathbf{v}_S$. Since it is a system of two equations with two unknowns, it can be typically solved for one of the parameters by elimination of the other unknown parameter (simply substitute one equation into the other). The idea is therefore, to use the information obtained from the measured field pressures to solve the resulting inverse linear problem. For example, if the acoustic parameters to be reconstructed are the particle velocities at the surface nodes, then substitution of (4.7) into (4.5) gives

$$\mathbf{A}_f(\mathbf{A}_S^{-1}\mathbf{B}_S\mathbf{v}_S) - \mathbf{B}_f\, \mathbf{v}_S = -\,\mathbf{p}_f, \tag{4.9}$$

and finally, solving for $\mathbf{v}_S$ yields

$$\mathbf{v}_S = \mathbf{C}^{-1}\, \mathbf{p}_f, \tag{4.10}$$

where $\mathbf{C} = (\mathbf{B}_f - \mathbf{A}_f\mathbf{A}_S^{-1}\mathbf{B}_S)$ is usually known as the *acoustic transfer matrix*, and its coefficients can be computed in advance since they depend only on the geometry and the analysis frequency. It is clear now that the back reconstruction of the velocities $\mathbf{v}_S$ can be achieved by taking enough measurements of pressures in the sound field, and by direct inversion of the matrix $\mathbf{C}$ provided that it is not singular and its inverse $\mathbf{C}^{-1}$exits. It happens however that the transfer matrix of inverse problems such as that defined in (4.10) is usually ill–conditioned and nearly singular, making the solution of equation (4.10) far from a simple inversion of the matrix $\mathbf{C}$. Alternatively, the solution can be stated in the least–squares form

$$\min_{\mathbf{v}_S} \quad \|\mathbf{C}\, \mathbf{v}_S - \mathbf{p}_f\|^2, \tag{4.11}$$

nonetheless, due to the rank deficiency of the linear system there is not only a unique solution but rather there are many solutions close to the desired one that minimizes equation (4.11). On the other hand, things get more complicated in a practical situation where the measured sound pressure is contaminated with some level of noise, in such a way that

$$p_f = p_{\mathrm{T}} + p_{\mathrm{e}}, \tag{4.12}$$

i.e. the actual measured data $\mathbf{p}_f$ contains not only components of the true field pressure p_{T} but also a noisy component p_{e}. In the worst case if the levels of noise are larger than the actual field pressures, the reconstructed parameters will be dominated only by errors.

For these reasons acoustic parameter estimation by inverse BEM, and in general inverse problems in the form of equation (4.10), requires a special treatment known as *regularization*.

4.3 Ill-conditioning of the acoustic transfer matrix

As in the case of the NAH based on the spatial Fourier transform technique, the acoustic transfer matrix $\mathbf{C}$ in (4.10) is complex, full populated, and ill-conditioned, being the latter condition the reason that makes necessary the use of special techniques to compute the inverse of $\mathbf{C}$ so that meaningful solutions of (4.10) can be achieved. But before passing to review some of the existent regularization techniques, two aspects regarding the ill-conditioning of the matrix will be discussed.

4.3.1 Errors due to the ill-conditioning

In order to better appreciate the effects of the ill-conditioning of the acoustic transfer matrix, let us take hand of the Singular Value Decomposition (SVD) technique, which is a numerical tool that has been widely used in the analysis of linear systems due to its capability to provide detailed information of the linear system's behavior. The theory of this useful technique is well established and it has been well documented in the literature (e.g. [25, 69]). This section is therefore devoted to show the application of the SVD to the acoustic transfer matrix rather than introducing the fundamentals of the SVD technique itself. Nevertheless the basic properties of the SVD are discussed next.

In principle any $M \times N$ complex matrix $\mathbf{D}$ can be represented by its eigen–vector

factorization (or SVD) as

$$\mathbf{D} = \mathbf{U}\mathbf{\Sigma}\mathbf{V}^H, \tag{4.13}$$

where the superscript $[\ \ ]^H$ means the *hermitian* transposed. In a pictorial way, for the case $M > N$ this factorization looks like follows

$$\begin{pmatrix} \\ \\ M \times N \\ \\ \\ \end{pmatrix} = \begin{pmatrix} \\ \\ M \times M \\ \\ \\ \end{pmatrix} \begin{pmatrix} \alpha_1 & 0 & \dots & 0 \\ 0 & \alpha_2 & & \vdots \\ \vdots & & \ddots & 0 \\ \vdots & & & \alpha_N \\ \vdots & & & 0 \\ \vdots & & & \vdots \\ 0 & 0 & \dots & 0_M \end{pmatrix} \begin{pmatrix} \\ \\ N \times N \\ \\ \\ \end{pmatrix},$$

where it is clear that $\mathbf{U}$ is $M \times M$, $\mathbf{V}$ is $N \times N$, and $\mathbf{\Sigma}$ is an $M \times N$ matrix whose elements in the diagonal $\mathrm{diag}(\mathbf{\Sigma})$ are the singular values of $\mathbf{D}$ in the order $\alpha_1 > \alpha_2 > \ldots > \alpha_N > 0$. The matrices $\mathbf{U}$ and $\mathbf{V}$ are unitary and their columns are known respectively as the left–side eigen vectors and right–side eigen vectors of the matrix $\mathbf{D}$. Furthermore, $\mathbf{U}$ and $\mathbf{V}$ have the property that satisfies

$$\mathbf{U}^H\mathbf{U} = \mathbf{U}\mathbf{U}^H = \mathbf{V}^H\mathbf{V} = \mathbf{V}\mathbf{V}^H = \mathbf{I}, \tag{4.14}$$

where $\mathbf{I}$ is the identity matrix. It is worth to introduce also the term *condition number*, which is another concept useful to quantify the ill-conditioning of a matrix, and is defined as

$$k(\mathbf{D}) = \|\mathbf{D}\| \, \|\mathbf{D}^{-1}\| = \frac{\alpha_1}{\alpha_N}. \tag{4.15}$$

Going back to the inverse acoustic problem defined in (4.10), the ill-conditioned matrix $\mathbf{C}$ can be represented by its SVD factorization as seen before,

$$\mathbf{C} = \mathbf{U}\mathbf{\Sigma}\mathbf{V}^H. \tag{4.16}$$

Here is where SVD comes to help in the problem. When the acoustic transfer matrix $\mathbf{C}$ is ill-conditioned, the singular values α_i's of the diagonal of $\mathbf{\Sigma}$ tend to fall quickly to tiny values under the unity (and consequently a large condition number is obtained). This tendency has been observed (by previous work, [54, 55]) to be highly dependent on the place of the measurement points. The best situation that can be achieved is when the measurements are taken right on the surface nodal points. The condition number then increases drastically as the measurement points are moved out from the surface.

As an example, consider two acoustic transfer matrices $\mathbf{C}_S$ and $\mathbf{C}_f$ generated by the inverse BEM process discussed before, and corresponding to measurements taken in the interior of a volume space whose geometry is a unit cube. Figure 4.3 shows two cases in which: **a)** the measurement points are placed on the surface nodes (thus obtaining $\mathbf{C}_S$), and **b)** when the measurements are taken uniformly distributed in the interior space (giving $\mathbf{C}_f$). Figure 4.3c shows that in both cases, a) and b), the acoustic transfer matrices have singular values smaller than unity, i.e. both are ill-conditioned, however the transfer matrix $\mathbf{C}_f$, which was generated with measurement points in the interior field, exhibits singular values decaying faster into tiny values. How much is each transfer matrix ill-conditioned?, employing the condition number defined in (4.15), it is seen that $k(\mathbf{C}_S) = 57.14$ and $k(\mathbf{C}_f) = 2.45 \times 10^{11}$ in the example. These numbers suggest that the transfer matrix $\mathbf{C}_S$ would lead to a considerably more accurate reconstruction of the surface velocities $\mathbf{v}_S$ than the transfer matrix $\mathbf{C}_f$ when solving either (4.10) or (4.11). And certainly that is the case, but again, as long as the measured data is not dominated by high levels of noise, and the geometry of the problem allows measurements at least as close as possible to the surface nodes. In practice this situation is hardly found, therefore acoustic engineers on inverse acoustic problems have to deal with highly ill-conditioned transfer matrices (with large condition numbers such as the one of $\mathbf{C}_f$ in the example above) even when they have the possibility to take a few measurements close to the vibrating surface. For this reason, the problem addressed in the present work considers the worst case in which, due to the large complex geometry of realistic indoors, measurement of sound pressure at the surfaces is not possible and the measurements are taken along the interior field (as in the case of Figure 4.3b). From the definition in (4.15), it can be expected that transfer matrices with large condition numbers are nearly singular, implying that their inverse may not exists and that the solution of the linear system is not unique. Unfortunately, a general rule to specify limits on how much singular the transfer matrix is allowed to be in order to obtain meaningful solutions is still a research subject.

In addition to the problem of non-uniqueness of the solution of (4.10) or (4.11), the ill-conditioning of the transfer matrix affects the accuracy of the reconstructed parameters in another way: as the transfer matrix gets more singular, the inverse linear system becomes more sensitive to the noise in the measured data. To appreciate better the role that the singular values play in the accuracy of the solution let us rewrite the SVD factorization of

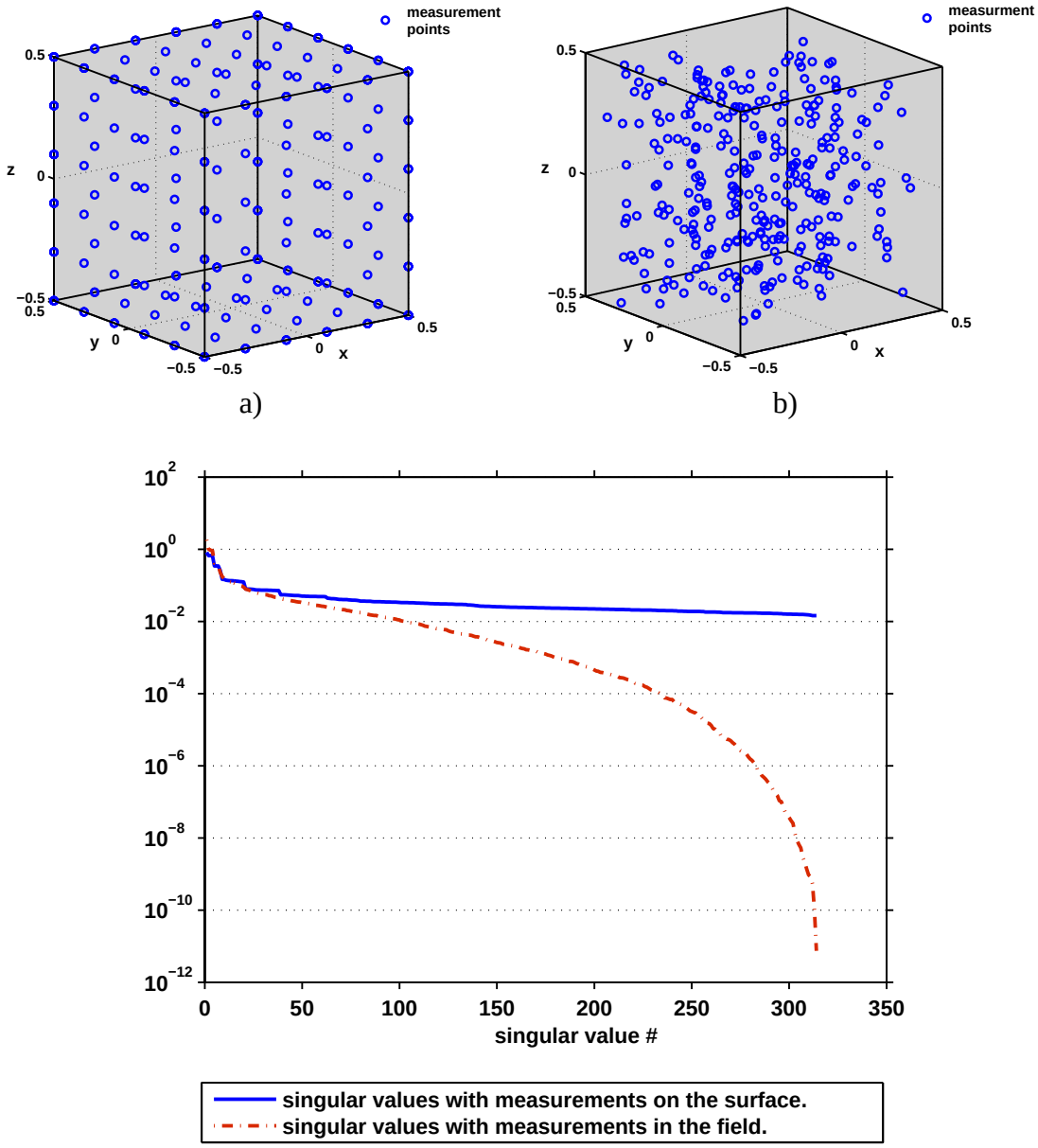

a) b)

c)

Figure 4.3: Example of measurements in a unitary cube geometry at 100 Hz: a) the measurement points are placed at the surface nodal points (314 nodes), b) the measurement points are uniformly distributed in the interior space (314 points). c) Singular values α_i's of the corresponding acoustic transfer matrices.

$\mathbf{C}$ from equation (4.16) in the vector equation

$$\mathbf{C} = \mathbf{U}\mathbf{\Sigma}\mathbf{V}^H = \sum_{i=1}^{N} \overline{\mathbf{u}}_i \alpha_i \overline{\mathbf{v}}_i^H, \tag{4.17}$$

where the vectors $\overline{\mathbf{u}}_i$ and $\overline{\mathbf{v}}_i$ are the columns of the matrices $\mathbf{U}$ and $\mathbf{V}$ respectively. This factorization is now substituted into equation (4.10), and using the orthonormal properties of the unitary matrices $\mathbf{U}$ and $\mathbf{V}$, the inverse reconstruction of surface velocities $\mathbf{v}_S$ takes the form

$$\mathbf{v}_S = \mathbf{V}\mathbf{\Sigma}^{-1}\mathbf{U}^H\mathbf{p}_f = \sum_{i=1}^{N} \frac{\overline{\mathbf{u}}_i^H \cdot \mathbf{p}_f}{\alpha_i} \overline{\mathbf{v}}_i. \tag{4.18}$$

Recalling that the actual measurements are contaminated by noise components as represented in equation (4.12), last equation becomes

$$\mathbf{v}_S = \sum_{i=1}^{N} \overline{\mathbf{u}}_i^H \left(\frac{\mathbf{p}_\mathrm{T}}{\alpha_i} + \frac{\mathbf{p}_\mathrm{e}}{\alpha_i} \right) \overline{\mathbf{v}}_i. \tag{4.19}$$

From the above expression, it can be clearly observed that the final effect of the presence of small singular values α_i's is an amplification of the actual data together with the noise components. If high levels of noise are introduced in the data, they will be amplified by the small singular values and as a result the solution will be dominated by erroneous values. In this sense, efforts should be made in order to ensure the best SNR when performing the experimental measurements.

4.3.2 Causes of the ill-conditioning

The causes of the ill-conditioning of the transfer matrix are manifold. For example, while it has been observed that the ill-conditioning keeps a strong relationship with the geometric complexity of the problem, other factors such as the modal response of the acoustic domain and the quality of the modeling mesh have also influence over the condition number of the acoustic transfer matrix. The latter two factors are investigated and discussed in a further chapter.

I. The mathematical point of view: Fredholm integral equations.

Boundary condition problems usually involve the solution of integral equations in the form of Fredholm integral equations of the first or second kind, [69, 1]. It is well known

thus, that acoustic inverse problems based on the Helmholtz integral equation (4.3) fall into the type of Fredholm integral equations of the first kind, which have the general form

$$\int_a^b K(x,y)\varphi(y)dy = f(x), \qquad a \leq x \leq b, \tag{4.20}$$

where $K(x,y)$ is any integrable kernel. For the case of inverse problems, $f(x)$ is known and $\varphi(y)$ is the sought function. The analogous matrix form of equation (4.20) can be written as

$$\mathbf{K}\,\boldsymbol{\varphi} = \mathbf{f}, \tag{4.21}$$

and the solution of the latter equation is now given by

$$\boldsymbol{\varphi} = \mathbf{K}^{-1}\,\mathbf{f}, \tag{4.22}$$

It is clear now the close similarity between equation (4.22) and the inverse acoustic problem defined by equation (4.10) whose transfer matrix $\mathbf{C}$ is computed using kernels of the form $\partial\mathrm{G}/\partial n$ and G, being G the Green's function. On the other hand, studies on inverse problems (e.g. [64, 98]), have shown that Fredholm equations of the first kind are inherently ill-conditioned, and there is no warranty for a successful solution of $\varphi(y)$ from equation (4.20), given an arbitrary kernel $K(x,y)$ and a known $f(x)$ with poor accuracy. The reason can be explain from the observation that, while the forward mapping from $\varphi(y)$ to $f(x)$ using (4.20) with a given kernel is bounded and unique, the inverse process may not be bounded. Moreover, since applying a kernel to a function often results in a smoothing operation, detailed information of the original mapping is lost, yielding the non-uniqueness of the solution in the inverse operation.

II. The physical interpretation.

Recall that the kernels of the BEM integral equations are the fundamental solution of the Helmholzt equation (3.4)–the Green's function

$$\mathrm{G}(r,\omega) = \frac{e^{-j\mathrm{k}r}}{4\pi r},$$

and its normal derivative

$$\frac{\partial\mathrm{G}}{\partial\mathrm{n}} = -\frac{1+j\mathrm{k}r}{4\pi r^2}e^{-j\mathrm{k}r}\left(\frac{\mathbf{r}\cdot\mathbf{n}}{|\mathbf{r}|}\right).$$

As depicted in Figure 3.1 of page 15, the magnitude of G decays with the proportion $1/r$, i.e. the inverse of the distance between the source and the receiving points. For the case

of the normal derivative $\partial \mathrm{G}/\partial \mathrm{n}$, the magnitude decays even faster (by a factor $1/r^3$). In practice this is translated as a rapid fading off of the sound waves from the source points (the surface nodal points) to the receiving points (measurement points). Consequently, when the measurements of sound pressure are placed out of the surface, the influences contributed by each individual discrete surface node tend to be in the same order of magnitude. Hence, the impact of this effect is directly reflected in the condition number of the transfer matrices assembled by the BEM process. Consider again the previous example of the two measurements steps: measurements of sound pressure at the surface nodes, and measurements distributed in the interior field. Figure 4.4 shows now a close up to a diagram of the measurements in 2D together with the corresponding transfer matrices. Note that although with small values, both matrices are complex and full populated. In the ideal case when the measurement points are on the surface boundaries, strong auto-influence coefficients of the BEM matrices are produced by the integral kernel evaluated at the neighbor elements of each node, Figure 4.4a. As a result, the entries of the acoustic transfer matrix are dominated by strong values in the main diagonal, see Figure 4.4b. A small condition number of the transfer matrix is obtained consequently, indicating that the boundary acoustic parameters can be recovered with high accuracy. On the other hand, as the measurement points are brought into the interior field, the transfer matrix changes its structure. A daigonal-dominant matrix can still be achieved if the measurements are taken close enough to the surface whenever it is possible, however, it is stressed again that this situation is hardly found in large and complex geometries. When the measurements are performed in the interior field, many of the influence coefficients computed by the BEM process tend to be similar for neighbor field points, Figure 4.4c. In other words, there is no auto-influence of the field points, and the final effect is a transfer matrix with similar columns (as seen in Figure 4.4d) producing rank deficiency that leads to a high condition number which, at the same time, readily adverts near-singularity of the transfer matrix. If one wants to reconstruct the boundary parameters by the inverse BEM process, some regularization techniques should be applied before the solution of the inverse system of equations either by the use of SVD analysis or incorporating extra information in the form of constraints. Some of the existent regularization techniques are discussed next.

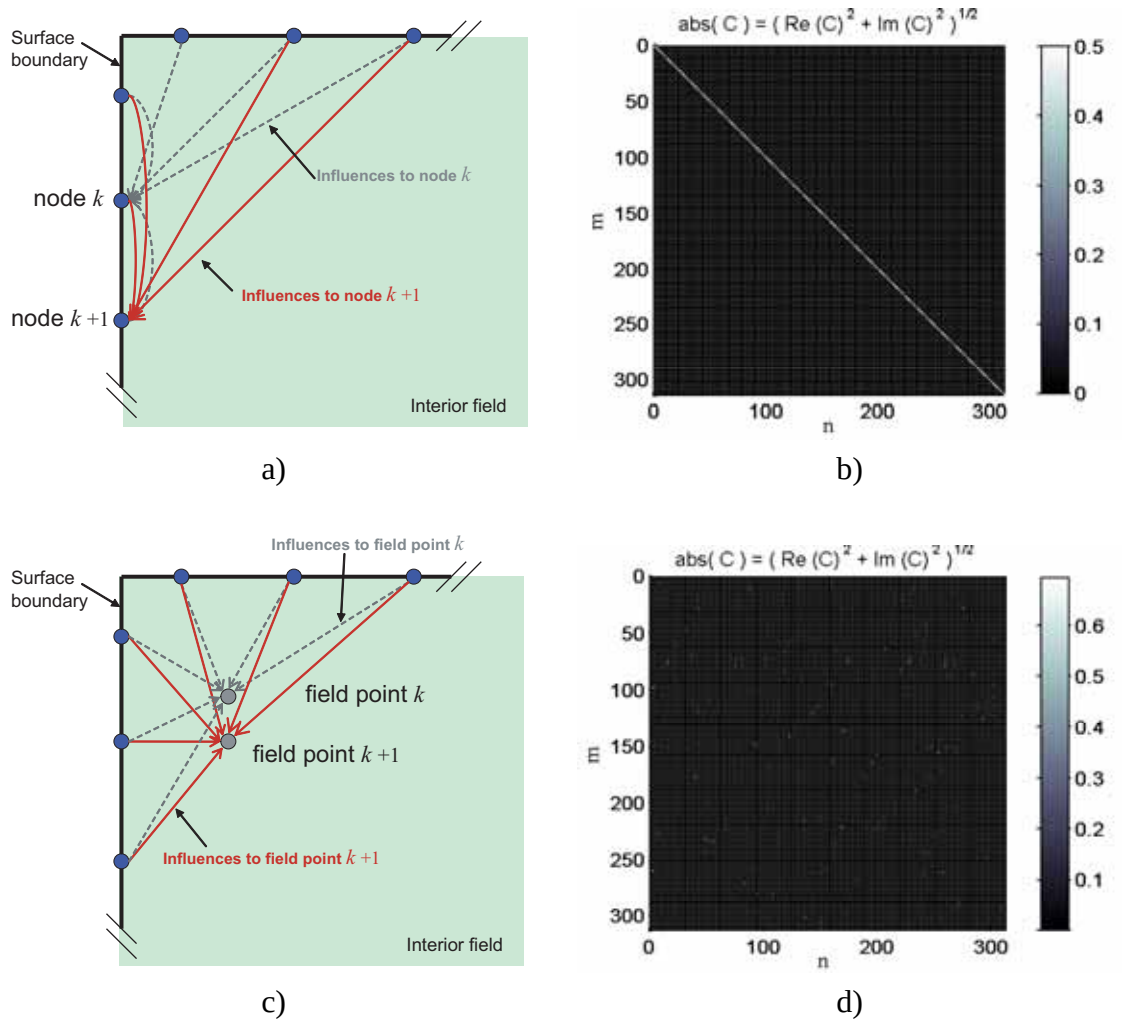

Figure 4.4: Measurement of sound pressures at: a) the surface nodal points, c) the interior field. b) and d) are the structures of the transfer matrices produced respectively in the cases a) and b). ($N = M = 314$, at 100 Hz in a unit cube).

4.4 Existent regularization methods for ill-posed problems in inverse acoustics

In the area of acoustic parameter estimation by inverse problems, two regularization methods have been widely used in order to deal with the ill-posedness of the problem. The first one (e.g. [95, 65, 54]), which is based on the SVD analysis, is equivalent to the solution of equation (4.10) in the least–squares sense. The second method, known as Tikhonov regularization [90], represents a more sophisticated approach but involves extra computational effort as well. In recent years iterative methods have been also proposed by a number of researchers [8, 29, 77], unfortunately these are out of the scope of this dissertation. As a

brief note for interested readers, the latter methods depart from the observation that the iterative process can arrive to an approximate solution if the iterations are stopped at an earlier time before the solver finds the solution with minimum residual. These iterative approaches seem to be promising due to their capability to handle large–scale problems, however, the lack of a unified stopping criteria is still the main pitfall for their usability.

4.4.1 Regularization by truncated-SVD

In previous sections, the mechanism in which the presence of small singular values affect the reconstruction of the boundary parameters was already studied: if the contribution of a node corresponds to a non-zero boundary value, the corresponding singular value will act as an scaling factor in the back reconstruction process; thus, small singular values will produce large and erroneous boundary values. This can be seen better recalling that in equation (4.18), the matrix $\mathbf{\Sigma}^{-1}$ has the structure form

$$\mathbf{\Sigma}^{-1} = \begin{pmatrix} \frac{1}{\alpha_1} & 0 & \dots & 0 \\ 0 & \frac{1}{\alpha_2} & & \vdots \\ \vdots & & \ddots & 0 \\ 0 & \dots & 0 & \frac{1}{\alpha_N} \end{pmatrix} \tag{4.23}$$

Hence the basic idea of the truncated-SVD is that, discarding an appropriate number of the last small singular values the original ill-conditioned transfer matrix $\mathbf{C}$ can be replaced by a near-by approximation which is a rank–k well-conditioned matrix $\mathbf{C}_k$. It is proven in [65] that the solution obtained by use of the new approximation matrix $\mathbf{C}_k$, the reconstructed parameters represent a least–squares solution of (4.11).

After truncation of $(N-k)$ singular values, equation (4.18) can be restated as

$$\mathbf{v}_{S_{tsvd}} = \sum_{i=1}^{k} \frac{\overline{\mathbf{u}}_i^H \cdot \mathbf{p}_f}{\alpha_i} \overline{\mathbf{v}}_i, \tag{4.24}$$

or written back to a matrix form,

$$\mathbf{v}_{S_{tsvd}} = \mathbf{C}_k^{-1} \mathbf{p}_f = \mathbf{C}^{+} \mathbf{p}_f, \tag{4.25}$$

where $\mathbf{C}^{+}$ is known as the Moore-Penrose pseudo-inverse of $\mathbf{C}$. Since singular values near to zero are discarded, errors in the reconstructed parameters are reduced, however, truncation of inadequate number of singular values leads to unrecoverable loss of information. Therefore, the key for the effectiveness of this method is how to determine the limit of the number of truncated singular values.

4.4.2 Tikhonov regularization

Tikhonov regularization (name due to its creator, Andrey Nicolayevich Tikhonov, [89]) is a technique widely used for the improvement of the solution of ill-posed problems. Its applicability to inverse acoustic problems has been demonstrated by a number of researchers as well, e.g [55][42][80]. This method is based on the observation that solutions obtained from ill-conditioned linear matrices contain highly dispersed values producing a large vector norm (usually measured with the 2-norm). Therefore, the improvement of the accuracy of the solution consists on requiring that the sought vector not only minimizes the unconstrained least–squares (4.11), but also have a small norm. The imposition of this constraint leads to a problem whose solution is given now by the weighted least–squares

$$\mathbf{v}_S = \min_{\mathbf{v}_S} \quad \|\mathbf{C}\,\mathbf{v}_S - \mathbf{p}_f\|^2 + \beta\,\|\mathbf{L}\,\mathbf{v}_S\|^2 \,. \tag{4.26}$$

The matrix $\mathbf{L}$ in last equation is usually an identity matrix, however, it can be substituted by another matrix that suites an specific problem. For example, $\mathbf{L}$ can be a discrete approximation of a derivative operator having a physical meaning. On the other hand, β is the regularization parameter that controls the balance between the two requirements. Making this regularization parameter bigger translates into solutions with small vector norm, and on the contrary, decreasing β results in solutions with low residual norm. Note that when $\beta = 0$ the problem reduces to the unconstrained least–squares (4.11).

As in the truncated-SVD, the key point in Tikhonov regularization is the selection of the optimal regularization value β. A practical approach to accomplish that is to construct a log plot by doing calculations with different values of β. It is observed that in general, the resulting curve shows an ”L”–like shape whose corner represents the optimal regularization parameter. Figure 4.5 shows the effects of varying the regularization parameter β. A mathematical procedure has been developed to compute th corner of this L curve, and it is described in detail in [32]. Another method to compute the optimal value of the regularization parameter is the so-called *Generalized Cross Validation* (GCV). This method attempts to find a balance between the perturbation errors and the regularization errors for all the valid regularization values of β. Thus the optimal point is accomplish by minimizing the functional

$$\min_{\beta} \quad f(\beta) = \frac{(1/N)\,\|(\mathbf{I} - \mathbf{B}(\beta))\mathbf{p}_f\|^2}{[(1/N)\,\mathrm{tr}(\mathbf{I} - \mathbf{B}(\beta))]^2}, \tag{4.27}$$

where M is the number of discrete nodes, $\mathbf{I}$ the identity matrix, tr denotes the trace of a matrix, and $\mathbf{B}(\beta)$ is a matrix which is computed as function of β using the following

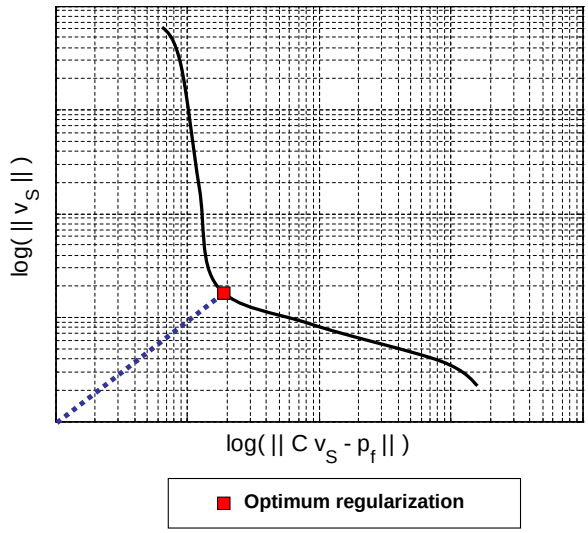

Figure 4.5: Inverse BEM in an interior problem.

expression:

$$\mathbf{B}(\beta) = \mathbf{C}[C^H C + \beta \mathbf{I}]^{-1} \mathbf{C}^H. \tag{4.28}$$

The derivation and application of the formulas above are out of the scope of this dissertation. Detailed description of the GCV can be found in [55]. Moreover, subroutines written in MATLAB to compute the GCV regularization parameter and the solution of discrete ill-posed problems are already available, [30].

Chapter 5

Least-squares estimation of the acoustic impedance from field measurements

In the previous chapter, the theory of the inverse acoustic problem based on the inverse boundary element method (IBEM) was studied, and the difficulties that prevent the solution of the inverse linear system be reachable by a simple least–squares approach. The example of the parameter reconstruction given as well, was focused on the estimation of the surface velocities $\mathbf{v}_S$ showing the general approach that other researchers have used in problems of sound source strength reconstruction. The purpose of this chapter is to introduce now the inverse acoustic problem targeted in the present work: estimation of the acoustic impedance of the surfaces in an interior field. The reader will realize that the fundamental form of this problem is similar to that of the inverse problems presented in previous sections. However, the definition of the acoustic impedance as the relation between the sound pressure and the particle velocity, makes our inverse linear problem turn into an non-linear optimization problem when extra information about the sought solution is incorporated as a constraining condition to the least–squares problem. As most of the inverse problems, the one introduced here is also ill-conditioned, and because of that, analysis simulations using basic geometries will be presented, showing the connection between some physical factors and the ill-conditioning of the acoustic transfer matrix. Finally, the back estimation of the surface impedances in a realistic geometry (an office room) is performed by numerical simulations as an example of the performance of the constrained least–squares of this chapter, and comparisons with other approaches will be shown.

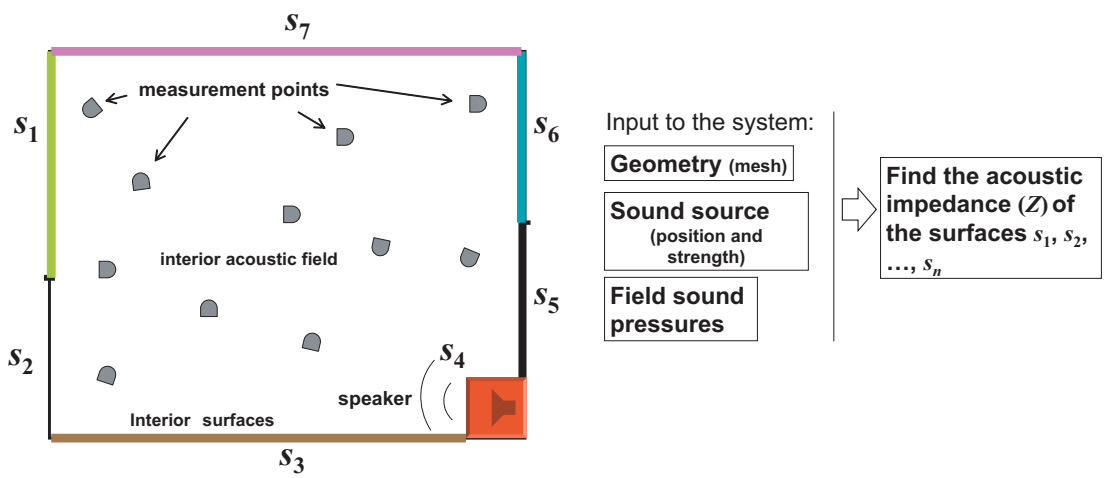

Figure 5.1: Inverse problem of the estimation of acoustic impedance at the interior surfaces.

5.1 Definition of the inverse problem

Similarly to the inverse radiation problems, the estimation of the acoustic impedance of the interior surfaces $S_1, S_2, ..., S_n$ of an enclosed space (e.g. a room) involves the solution of an inverse model and a set of sound samples measured in the interior field. In other words, given the geometry of the space, the strength and position of a time-harmonic sound source (e.g. a speaker with a sinusoidal tone) placed somewhere in the enclosing shape, and a set of sound pressures taken at known locations in the acoustic field, the problem is to find the acoustic impedance values Z_S of the interior surfaces, where at a given point x on a surface the Z_{s_x} is defined by the ratio between the sound pressure p_{s_x} and particle velocity v_{s_x} as

$$Z_{s_x} = \frac{p_{s_x}}{v_{s_x}}. \tag{5.1}$$

In Figure 5.1 the inverse problem of in-situ estimation of acoustic impedances is summarized.

Therefore the estimation of the impedance at the boundaries is equivalent to finding the sound pressure p_S and particle velocity v_S of the interior surfaces. In similar approaches, but for the reconstruction of sound source strength (i.e. [39]), it has been already shown that by means of the IBEM a solution to the problem of Figure 5.1 can be approach.

5.2 Estimation of $\mathbf{p}_s$ and $\mathbf{v}_s$ by the inverse BEM

5.2.1 The least–squares solution

Let us begin again recalling the Kirchhoff–Helmholtz equations for the interior field in their matrix form:

$$\mathbf{A}_S\,\mathbf{p}_S - \mathbf{B}_S\,\mathbf{v}_S = 0, \tag{5.2}$$

$$\mathbf{A}_f\,\mathbf{p}_S - \mathbf{B}_f\,\mathbf{v}_S = - = \mathbf{p}_f. \tag{5.3}$$

As discussed above, the geometry and the location of the field points $\mathbf{p}_f$ are known, therefore the influence matrices **A**'s and **B**'s can be computed in advance. Also information of the sound source strength (vibration amplitude of the speaker, $\widehat{\mathbf{v}}_S$) is known, thus equations (5.2) and (5.3) can be rewritten giving:

$$\mathbf{A}_S\,\mathbf{p}_S - \widetilde{\mathbf{B}}_S\,\widetilde{\mathbf{v}}_s = \widehat{\mathbf{B}}_S\,\widehat{\mathbf{v}}_S, \tag{5.4}$$

$$\mathbf{A}_f\mathbf{p}_S - \widetilde{\mathbf{B}}_f\widetilde{\mathbf{v}}_S = \widehat{\mathbf{B}}_f\widehat{\mathbf{v}}_S - \mathbf{p}_f, \tag{5.5}$$

separating unknown variables $\mathbf{p}_S$, $\widetilde{\mathbf{v}}_S$ in the left, and known parameters $\mathbf{p}_f$, $\widehat{\mathbf{v}}_S$ in the right side. The corresponding matrices are $\mathbf{A}$'s and $\widetilde{\mathbf{B}}$'s for the unknowns, and $\widehat{\mathbf{B}}$'s for the known parameters. It is readily noted that equations (5.4)–(5.5) form a linear system with two unknowns that can be solved by combining both equations. There are different choices to compute a solution for this linear system in the least–square sense. As studied in the previous chapter, one unknown variable can be eliminated by substitution of one equation into the other and then use SVD-based analysis to obtain one of the least-square solutions. However the approach taken here is as follows. Recalling that the sought parameter is the acoustic impedance given by (5.1), a solution for both $\mathbf{p}_S$ and $\widetilde{\mathbf{v}}_S$ is simultaneously computed. The unknowns $\mathbf{p}_S$ and $\widetilde{\mathbf{v}}_S$ of equations (5.4)–(5.5) can be grouped in one vector, and the augmented system of equations is therefore expressed as

$$\begin{pmatrix} \mathbf{A}_S & -\widetilde{\mathbf{B}}_S \\ \mathbf{A}_f & \widetilde{\mathbf{B}}_f \end{pmatrix} \begin{pmatrix} \mathbf{p}_S \\ \widetilde{\mathbf{v}}_S \end{pmatrix} = \begin{pmatrix} \widehat{\mathbf{B}}_S\widehat{\mathbf{v}}_S \\ \widehat{\mathbf{B}}_f\widehat{\mathbf{v}}_S - \mathbf{p}_f \end{pmatrix}, \tag{5.6}$$

or in a compact form

$$\mathbf{D}\mathbf{x}_S = \mathbf{d}. \tag{5.7}$$

Now the inverse estimation process can be done by taking $M \geq N$ measurements of field pressures $\mathbf{p}_f$ and obtaining the least-squares solution of equation (5.7). One may

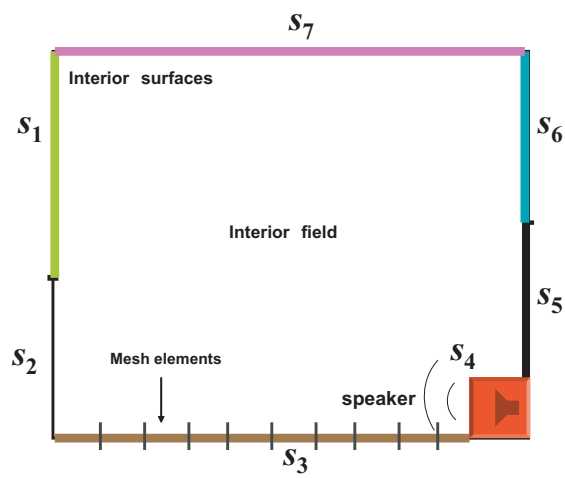

Figure 5.2: Segmentation of the interior surfaces.

argue that solving an augmented system of equations such as (5.7) involves unnecessary computational effort, and in fact, that argument is true. However, as it will be shown in the following paragraphs, the augmented arrangement of the BEM equations facilitates the addition of extra information in the form of a constraining term.

5.2.2 Exploiting a priori information of the surfaces

A priori knowledge of the distribution of the surfaces inside the given geometry may be exploited in order to incorporate extra information about the desired solution in the inverse estimation. In other words, assuming that the partitioning of surfaces inside a room is known (and represented in the 3D mesh as groups of elements), an additional constraint can be imposed to the least-square problem given in equation (5.7).

Let $\mathbf{k}_i$ be the acoustic impedance uniformly distributed over each surface S_i, where $i = 1, 2, ..., n$ surfaces, as illustrated in Figure 5.2. Assuming that the surfaces have homogeneous impedance value $\mathbf{k}_i$, the relation

$$Z_{S_i,j} = \frac{p_{S_i,j}}{v_{S_i,j}} = \mathrm{k}_i \qquad j = 1, 2, ..., m, \tag{5.8}$$

i.e. the impedance Z of the j-th element of surface S_i, should satisfy

$$\frac{p_{S_i,1}}{v_{S_i,1}} = \frac{p_{S_i,2}}{v_{S_i,2}} = ... = \frac{p_{S_i,m}}{v_{S_i,m}} = \mathrm{k}_i. \tag{5.9}$$

Because of the assumption that k_i is approximately constant and uniform on S_i, taking

the differential of the impedance with respect to the surface yields

$$\frac{d[Z_i]}{dS_i} = \frac{d}{dS_i}\left[\frac{p_{S_i}}{v_{S_i}}\right] = \frac{d[\mathbf{k}_i]}{dS_i} = 0 \tag{5.10}$$

In the actual meshed model the surfaces S_i are discretized into m elements, therefore an equivalent condition can be stated as follows:

$$f_{S_i}(Z) = \sum_{j=1}^{m_i-1} (Z_{S_i,j+1} - Z_{S_i,j}) = 0 \tag{5.11}$$

There are n different surfaces in the model, thus there are n equations of the form:

$$\begin{aligned} f_{S_1}(z) &= \sum_{j=1}^{m_1-1} (Z_{S_1,j+1} - Z_{S_1,j}) = 0 \\ f_{S_2}(z) &= \sum_{j=1}^{m_2-1} (Z_{S_2,j+1} - Z_{S_2,j}) = 0 \\ &\vdots \\ f_{S_n}(Z) &= \sum_{j=1}^{m_n-1} (Z_{S_n,j+1} - Z_{S_n,j}) = 0 \end{aligned}$$

Or expressed in the matrix form

$$\mathbf{f}(\mathbf{z}) = \mathbf{G}\mathbf{z} = \mathbf{0} \tag{5.12}$$

where

$$\mathbf{G} = \begin{pmatrix} \mathbf{W}_{S_1} & \mathbf{0} & \cdots & \cdots & \mathbf{0} \\ \mathbf{0} & \mathbf{W}_{S_2} & \mathbf{0} & & \vdots \\ \vdots & & \ddots & & \vdots \\ \vdots & & & \ddots & \mathbf{0} \\ \mathbf{0} & \cdots & \cdots & \mathbf{0} & \mathbf{W}_{S_n} \end{pmatrix} \quad , \quad \mathbf{W}_{S_i} = \begin{pmatrix} -1 & 1 & 0 & \cdots & \cdots & 0 \\ 0 & -1 & 1 & 0 & \cdots & 0 \\ \vdots & & \ddots & \ddots & & \vdots \\ \vdots & & & \ddots & \ddots & \vdots \\ 0 & \cdots & \cdots & 0 & -1 & 1 \end{pmatrix}$$

$$\mathbf{z} = [Z_{S_1,1} \cdots Z_{S_1,m_1} \ , \ Z_{S_2,1} \cdots Z_{S_2,m_2} \ , \ \cdots \ , \ Z_{S_n,1} \cdots Z_{S_n,m_n}]^T$$

The dimension of the matrices $\mathbf{W}_{S_i}$ is $(m_i - 1) \times m_i$. Equation (5.7) together with the condition (5.12) to solve a non–linearly constrained least-square problem. Furthermore, assuming that the relative impedance of the surfaces fall within an specific range, e.g.

between the relative impedance of air ($Z_0 = 1$) and the relative impedance of the hardest surface (concrete, Z_{max}), some bounds to the sought solution can be imposed.

The optimization problem is then given by:

$$\min_{\mathbf{x}_S} \quad g(\mathbf{x}_S) = \|\mathbf{D}\,\mathbf{x}_S - \mathbf{d}\|^2 + \mu\|\mathbf{G}\,\mathbf{z}(\mathbf{x}_S)\|^2 \tag{5.13}$$

$$\text{with} \qquad \mathrm{Z}_0 < \mathbf{z}(\mathbf{x}_S) < \mathrm{Z}_{max}$$

Note that the introduction of the constraining term (5.12) into the least-squares of (5.7), implicitly transforms the linear system into a non–linearly constrained optimization problem where fast algorithms for a standard least-squares solution (such as QR–decomposition) cannot be applied anymore. However, since the formulation of the minimization problem defined by (5.13) is in an standard form of a non–linear optimization problem, general methods for non–linear optimization cab be applied. For example, in the current implementation of the algorithm described above, non–linear optimization subroutines of the commercial software MATLAB are used for the solution of (5.13). On the other hand, it is worth to note that in contrast to the Tikhonov-regularized least–squares in equation (4.26), the solution of equation (5.13) requires the satisfaction of both terms: the residual norm and the norm of the non-linear term; therefore the weighting term μ can be set to 1 as an starting value. When the measurements are dominated by noise, the weighting parameter μ can be included in the optimization process as another unknown.

5.3 Numerical example: scaled office room

This section presents a simulated example of the inverse estimation of the acoustic impedances on the surfaces in an interior space. A numerical simulation is performed basically in two stages: a) The forward prediction, and b) the back reconstruction. As shown in Figure 5.3, in the stage a), sound pressures are computed at field points which are uniformly distributed among the interior space. Hence, input to the forward BEM process is: vibration amplitude of the sound source, the 3D model together with the coordinates of M field points, and the values of the impedances assigned manually to the surfaces of the 3D model. The output of stage a) is a set of complex sound pressures. This set of pressures is then used as input data for the inverse estimation process. Simulation of noise is included in numerical examples of further sections. Now in the inverse process, the impedance values of the surfaces is to be estimated, therefore, the input data to the stage b) is: vibration

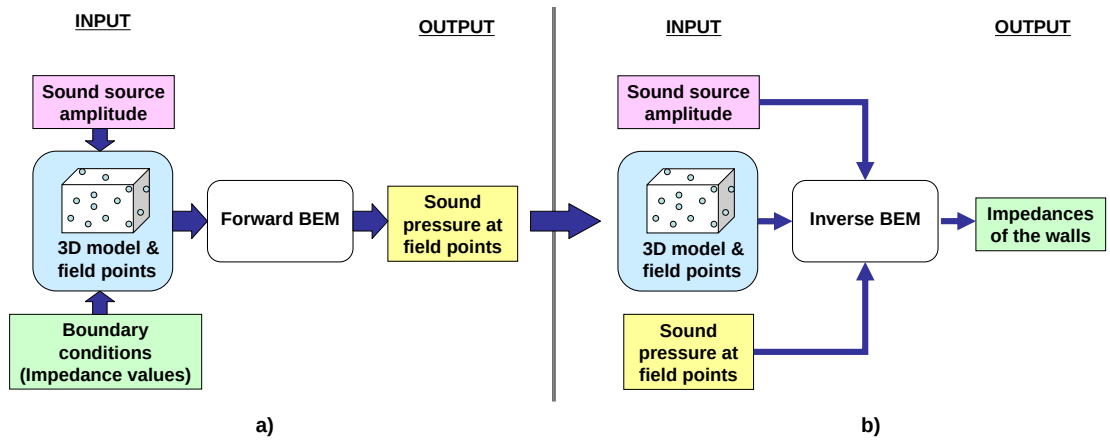

Figure 5.3: Flow chart of the numerical simulations: a) generation of data with known B.C., b) back reconstruction of the impedances.

amplitude of the sound source, the 3D model together with the coordinates of M field points, and the field pressures generated in the stage a).

The first 3D model used for the application of the inverse method presented in a previous section, consists of a realistic geometry taken from an empty office room. The model is scaled 1:4 and the surfaces are discretized using triangular elements. Figure 5.4 shows the scaled model of the office. The resulting mesh is composed of 414 elements ($N = 414$) with a maximum edge size of 0.168 m. Following the criterion of $1/6$ of a wavelength the mesh can be used in simulations for frequencies up to 340 Hz. However the analysis is limited to the range of 10–250 Hz.

As discussed above, a set of M points are uniformly distributed in the interior field, as shown in Figure 5.5. The field pressures are calculated in the forward BEM process in which acoustic impedances have been assigned manually to the boundaries. For simplicity, real-valued impedances have been applied to all the surfaces. Table 5.1 shows the type of materials assigned to the surfaces and their impedance values which were taken from a database [83]. Note that they are not the original values of the real office room but they are useful for our test purposes in this example. The relative impedance $\mathrm{Z_r}$ in Table 5.1 is given by the relation

$$\mathrm{Z_r} = \frac{\mathrm{Z_c}}{\mathrm{Z}_a}, \tag{5.14}$$

where $\mathrm{Z_c}$ is the characteristic acoustic impedance of the material. Z_a is in this case the characteristic impedance of air, $\mathrm{Z}_a \simeq 415$ rayls.

A sound source is simulated by placing the model of a loudspeaker in one corner of

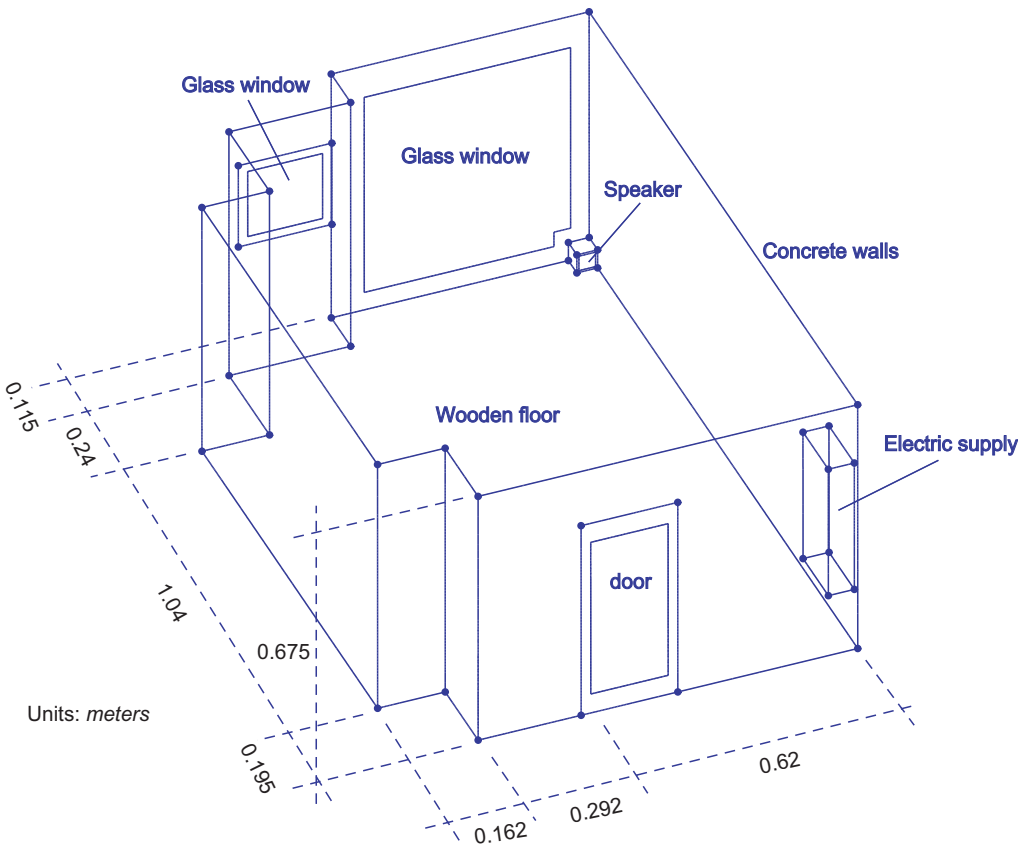

Figure 5.4: Scaled model of the office room.

the room. The dimensions of the real loudspeaker are $(9.5 \times 9.5 \times 10)$ cm, thus after scaling it can be properly simulated with cubic geometry. The vibrating surface of the speaker displaces with an amplitude of particle velocity of $1\ \mathrm{m}^3/\mathrm{s}$. On the other hand, vibration modes can be expected to fall within the range of analysis frequencies, however the effects of the vibration modes will be discussed and illustrated in a further example.

The generated set of field pressures is used in the inverse process defined in equation (5.7) to recover the designated impedances . In practice however, the measurements are

Surface	**Material**	**Impedance** ($\times 10^6$ Rayls)	**Relative Impedance**
floor	Wood	1.5	3,614
walls	Concrete	8	19,277
windows	Glass (8 mm)	13	31,325
door	Aluminum	17	40,964

Table 5.1: Assignment of acoustic impedance values for the simulations with the office room.

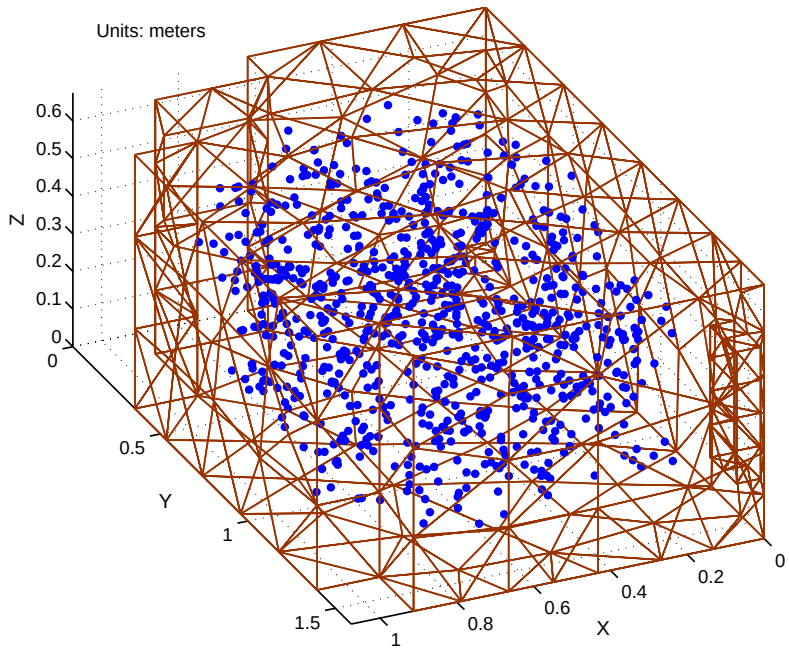

Figure 5.5: Mesh and randomly distributed field points.

contaminated with some level of noise. It has been studied in previous chapters how this noisy components are propagated to the reconstructed boundary parameters by means of the amplification effect due to singular values of the ill-conditioned matrix. Moreover, when dealing with computer simulations, noise is also introduced by the numerical approximations of the analysis method employed. In principle, the BEM leads to the introduction of noise caused by the discrete approximations and the round off's in the operations. Although current computer systems are able to work with high precision floating-point numbers the tiny singular values of the inverse transfer matrix tend to decay at the same time to infinitesimal values as the arithmetic precision of the computer systems allows. For these reasons, even when artificial noise is not added to the field pressures generated in the forward BEM stage, the impedance values are not recovered perfectly. In order to show this effect, in the present example noise has been neglected in the field pressures. Hence the following analysis will investigate the levels of error introduced by the inverse process itself.

Another point to show in this numerical example is the solution obtained by using different solvers applied to the inverse problem (5.7). Therefore, for the purpose of comparisons two sets of M field pressures is generated: a set with $M = N$, and a set with

$M = 2N$ field points. In the case of $M = N$, the classic Gaussian elimination with partial pivoting is employed as linear solver and compared with the solution obtained by using Tikhonov regularization applied to the same linear system. For $M = 2N$ field points, the inverse linear system is overdetermined. In this case the least-squares optimization of equation (5.13) is used, and compared again to the solution obtained by applying Tikhonov regularization to the same overdetermined system.

The error of the estimated values is measured as a relative norm error, which is calculated as

$$\text{error}(\%) = \frac{\|(\mathbf{p}_S, \mathbf{v}_S) - (\mathbf{p}_\text{X}, \mathbf{v}_\text{X})\|}{\|(\mathbf{p}_S, \mathbf{v}_S)\|} \times 100, \tag{5.15}$$

where $\mathbf{p}_\text{X}$ and $\mathbf{v}_\text{X}$ are respectively the surface sound pressures and velocities estimated by the inverse process. $\|\cdot\|$ denotes the 2-norm. Figures 5.6 and 5.7 show the amplitudes and phase reconstructions, as well as the computation times achieved by each solver.

Regarding Figures 5.6 and 5.7, the following observations can be made:

- The reconstruction error of surface velocities $\mathbf{v}_S$ always keeps a higher level than that of the surface pressures $\mathbf{p}_S$. However, these levels of error tend to decrease as the analysis frequency increases. This tendency can be observed more evidently in the relative norm error of amplitude in Figure 5.6 with $M = N$. Previous work in the inverse radiation problem with NAH has also pointed out this effect and it was mentioned in [39] with studies on an interior problem.

- In the case when $M = N$ (i.e. number of field pressures p_f is equal the number of elements in the mesh), Tikhonov regularization shows lower error levels than Gaussian elminiation. However after about 110 Hz (i.e. $\lambda/d \approx 18$, with d =max. size of the elements), the performance of Gaussian elimination tends to get closer to the one of Tikhonov regularization, being the first in addition approximately 30 times faster than the second. Recall that Tikhonov method involves SVD analysis which in turn is expensive. However it should be stressed here, that the use of efficient solvers such as Gaussian elimination may be possible when a high signal to noise ratio is ensured, in which case computationally efficient solvers represent an alternative to deal with large-scale problems.

- With a number of field points bigger than the number of elements in the mesh (e.g. $M = 2N$), the constrained least-squares optimization approach gives similar performance to Tikhonov method, being in addition approximately 7 times faster.

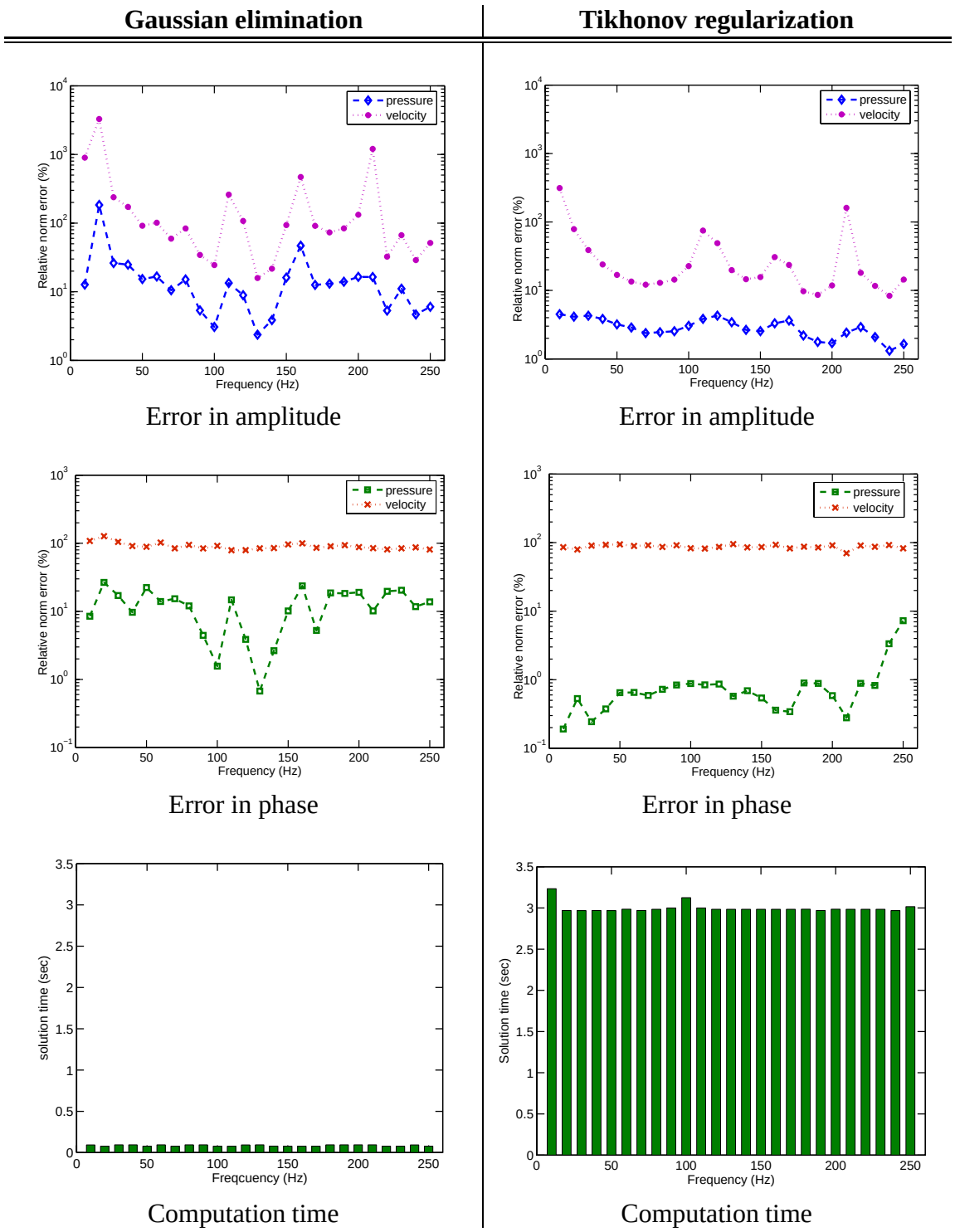

Figure 5.6: Recovered sound pressures and velocities with $M = N$ field samples in the office room simulations.

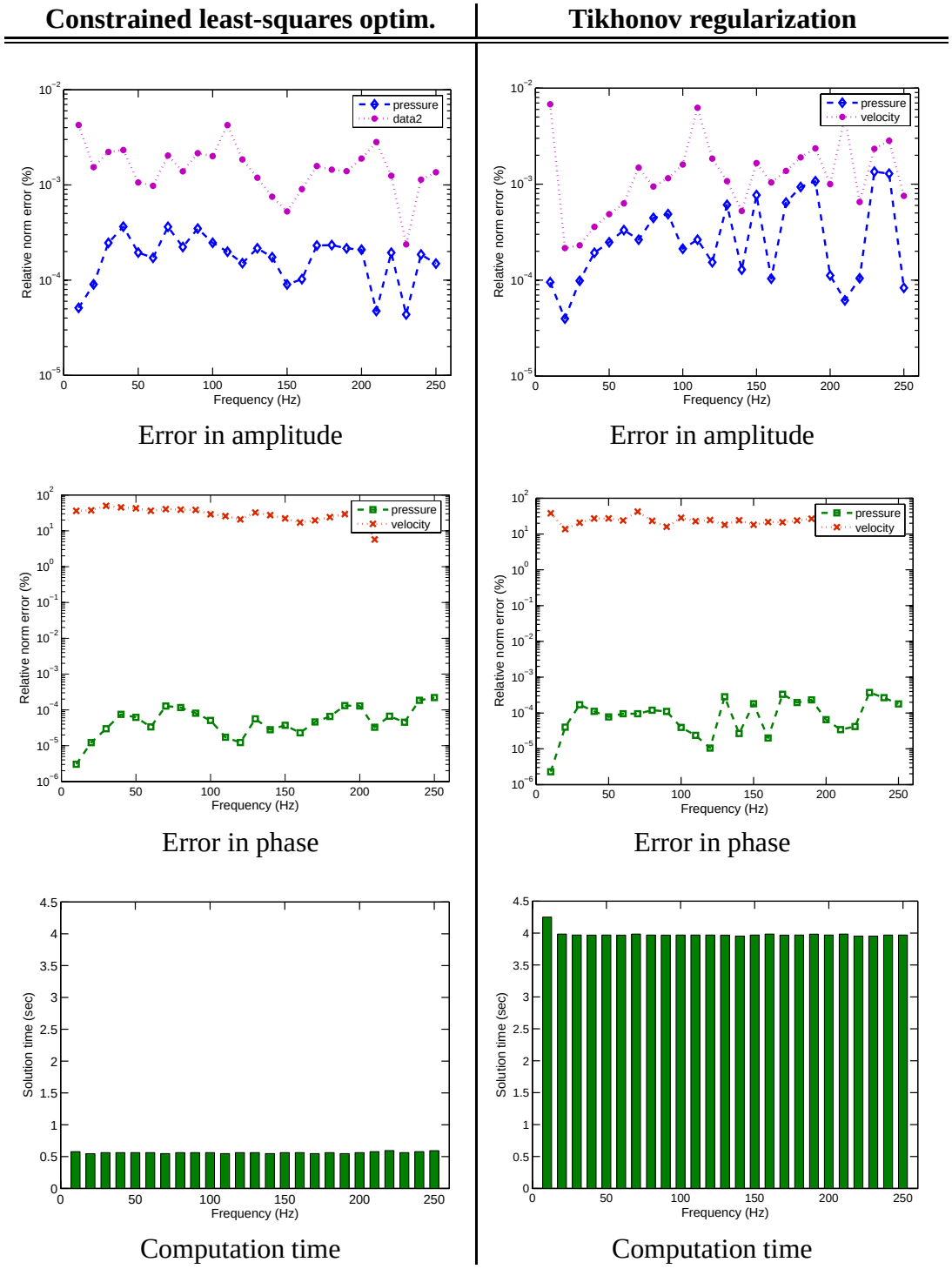

Figure 5.7: Recovered sound pressures and velocities with $M = 2N$ field samples in the office room simulations.

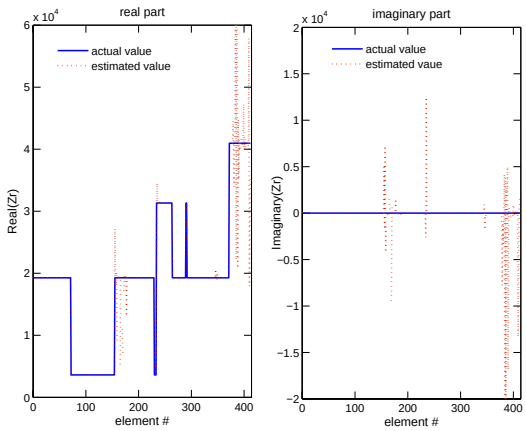

Figure 5.8: Relative impedances in the surfaces of the office room at 210 Hz.

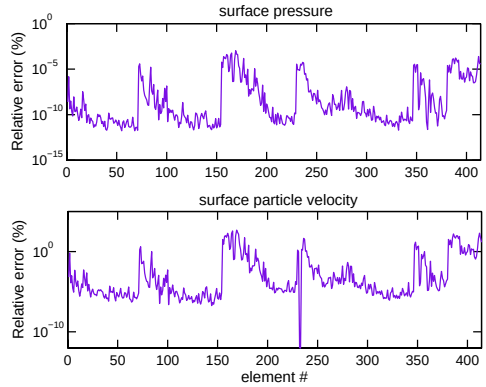

Figure 5.9: Reconstructed surface pressures and particle velocities of the office room at 210 Hz.

In this example the weighting factor μ of equation (5.13) was found to be optimum in with small values within the order of 10^{-8} to 10^{-7}. This is to be expected since there is no noise component in the field pressures, and therefore the error is basically due to the residual term.

On the other hand, an example of the recovered impedances by least-squares at a test frequency of 210 Hz and $M = 2N$ is also shown in Figure 5.8, where the real and imaginary parts have been plotted element-wise for a better appreciation. Figure 5.9 shows in a similar way the estimated surface pressures and velocities of the same example. As can be seen in Figure 5.9, a low percentage of error was obtained in the solutions by the overdetermined least-square optimization. The relative error of surface pressures remains under 1% in all the elements and in most of the surface velocities. From Figure 5.8, it can be seen that the recovered acoustic impedances are nearly the same as the actual values assigned manually. Nonetheless, it should be noted from these results that even when low error levels in surface pressures $\mathbf{p}_S$ and velocities $\mathbf{v}_S$ where achieved, the reconstruction of impedances is more sensitive to errors since the impedance is given by the relationship of both the surface pressure and particle velocity. The elements where erroneous impedance was obtained can be observed easily by looking at the imaginary part of the estimated impedances of Figure 5.8, in which the original value is zero for all the elements. Regarding this, it has been already mentioned in [54] and [97] that these errors are closely related to the complexity of the geometry. This fact will be discussed in next section.

5.4 Analysis of Errors introduced in the solution

Let us examine now two geometric factors that affect the accuracy of the estimation of the acoustic impedance on the boundaries: the *vibration modes* and the *mesh quality*. The effects of the vibration modes has been investigated previously by Nelson and Yoo, [54, 55], for the case of radiation problems (reconstruction of sound source in exterior surfaces) , and the influence of these resonance modes on the ill-conditioning of an interior problem was mentioned also by Kim and Ih [39], in which they presented the problem of noise source identification in the interior of half–scaled car cabin. General conclusions are stated in their reports, but since the numerical examples presented in those reports consist of complex geometries, it is difficult to see a direct connection between the ill–conditioning of the acoustic transfer matrix and the geometry of the vibro–acoustic structure. Hence, in order to appreciate the implications of geometric factors such as modal response and mesh quality, the next paragraphes present a numerical analysis example using an enclosed surface with a basic geometric shape (a unit cube).

5.4.1 Effects of the modal response

When in an enclosed space there are at least a pair of parallel walls and the distance between them is a harmonic multiple of the wavelength, standing waves will arise due to the interference between the incident and the reflected waves, creating thus an interference pattern along the vibration axis of that pair of walls. These patterns are what is known as *vibration modes*, and they represent the *resonant* frequencies (or *eigenfrequencies*) of that geometric space. There is therefore a strong relationship between the vibration modes and the geometry of the enclosed field. The resonant frequencies of a rectangular geometric space in 3D, can be calculated by the following equation (see [48, 66]):

$$f_{\mathbf{m}}(m_x, m_y, m_z) = \frac{c}{2}\sqrt[2]{\left(\frac{m_x}{l_x}\right)^2 + \left(\frac{m_y}{l_y}\right)^2 + \left(\frac{m_z}{l_z}\right)^2} \tag{5.16}$$

where $m_x, m_y, m_z = 1, 2, \ldots$, are the axial modes of that space. Any combination of m_x, m_y, m_z gives a mode. l_x, l_y, l_z are the dimensions of the rectangular room along the x, y, and z axis respectively. In [39], it is pointed out that these modes are related with the condition number of the transfer matrix through the *anti-resonances* that cause the *transmission zero* of the system, [39]. In order to observe the variation of the condition number the following numerical examples is presented here.

A unit cube is meshed into 432 triangular elements with nearly the same size. Taking the element size rule of $1/6$ wavelength, the maximum analysis frequency allowable by this mesh model is approx 455Hz. The analysis is then performed for a range of frequencies 10–450 Hz with interval steps of 10 Hz. In an ideal case, the walls of the cube would be assigned a rigid condition ($v_S = 0$), which implies an infinite impedance boundary condition. However, it is clear that values of $Z = \infty$ or $v_S = 0$ are not likely to be obtained by the inverse process because of the ill-conditioning, making the solution rather erroneous and difficult to validate. Instead of perfect rigid boundary conditions, the impedance value of concrete (8×10^6 rayls) walls is assigned to the sides of the cube. We can expect now estimated values not such as $v_S = 0$ but small values close to zero.

The number of field points for this analysis is fixed to $M = 2N$. As in the numerical example of the previous section, the field points are uniformly distributed among the interior space. Finally, the sound field in the interior is generated by a mesh element which is vibrating harmonically with an amplitude of $1\ \mathrm{m}^3/\mathrm{s}$ and zero phase, located at the center of one of the walls.

With the above settings, the analysis is performed for each step frequency following the procedure described before in Figure 5.3. Noiseless field pressures are considered again here since the purpose of this simulation example is to investigate the effects of the vibration modes over the ill-conditioning of the problem.

Figure 5.10a shows the condition number of the acoustic transfer matrix, plotted with the frequency on the x-axis. The eigenfrequencies have been aligned to the bottom of the graph for a better comprehension. From the results of this test, it is observe that the condition number of the linear system takes maximum values at the frequencies of resonance associated with the cube. Although the condition number shows a decreasing tendency at high frequencies, the eigenfrequencies become denser at that range. Here, the condition number of the matrix **D** of equation (5.7) is calculated as defined in equation (4.15):

$$k(\mathbf{D}) = \|\mathbf{D}\|\|\mathbf{D}^{-1}\|$$

where $\|\cdot\|$ denotes the 2-norm.

In Figure 5.10b the norm error of the sound pressures $\mathbf{p}_S$ and the velocities v_S recovered at each frequency step are shown. As in the previous analysis example, the level of error in the surface velocities is higher than that of the surface pressures. Moreover, considering the line of the surface pressure $\mathbf{p}_S$, minima can be observed at the frequen-

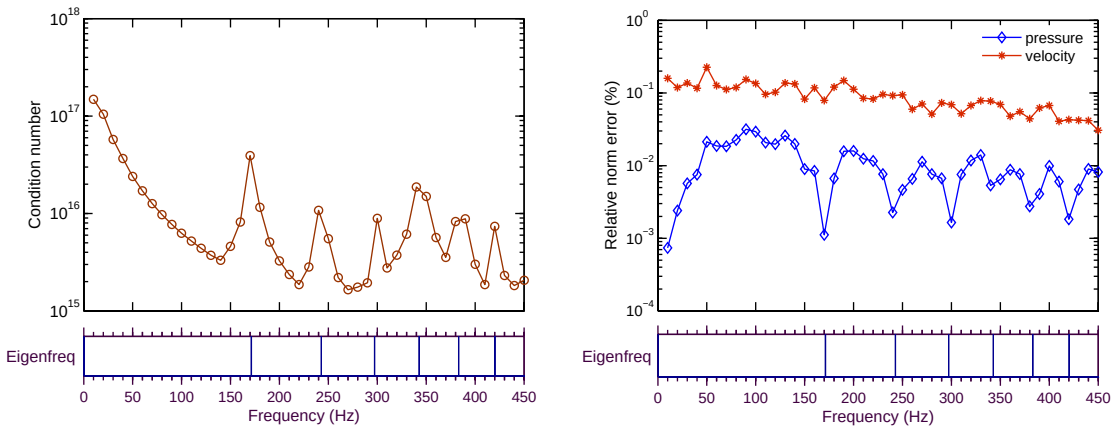

(a) (b)

Figure 5.10: Effects of the vibration modes over the inverse estimation accuracy. (a) Condition number vs. eigenfrequencies. (b) Relative norm error vs. eigenfrequencies.

cies of resonance. This observation seems to agree with experiments performed by other researchers. In the presence of noise, the errors are dominated by the amplification effect produced by the singular values. However, when the noise in the data is neglected, the errors are basically due to the numerical round-off's of the floating-point operations. Compared to the noise introduced in the physical measurements, the error caused by the round off's is relatively smaller. In this case it became evident that the ill-conditioning also affect the way the errors are distributed along the surface. This last effect is illustrated in figure 5.11 showing an error pattern produced by one of the resonance frequencies of the cube.

5.4.2 Effects of the mesh quality

Another geometrical factor that was found to affect the accuracy of the solutions is the size of the mesh elements. There is a tendency of the error to increase as the size of the mesh elements is less uniform. In order to investigate this effect, the unit cube is employed again and an analysis frequency that does not fall in any of the eigenfrequencies is chosen. The same boundary conditions used in the previous simulation with the cube are applied, but this time the area of a group of elements in the mesh is varied manually at each test, as illustrated in Figure 5.13. The *mesh quality* factor Q is define therefore as follows:

$$Q = \frac{max(\text{element area})}{min(\text{element area})} \tag{5.17}$$

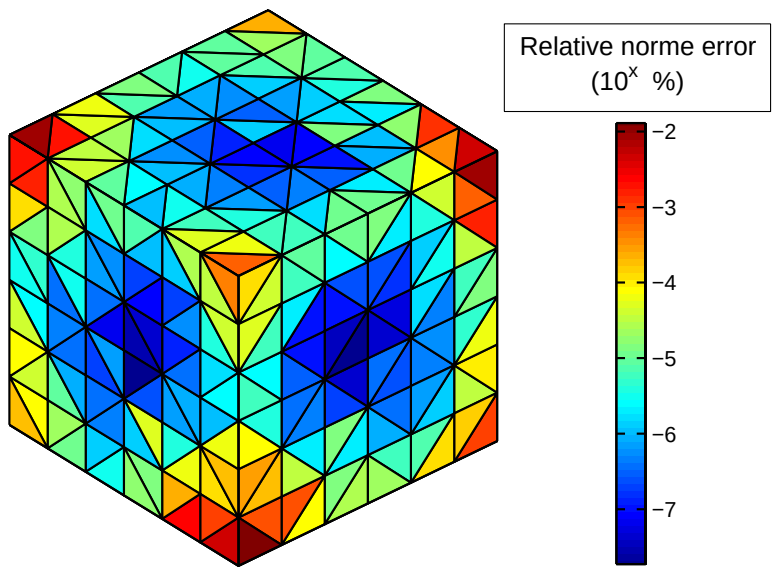

Figure 5.11: Example of an error pattern produced by a vibration mode at 243 Hz.

In this way the behavior of the errors can be appreciated in terms of the mesh quality factor. Taking again $M = 2N$ field pressures uniformly distributed inside the cube, the surface pressures $\mathbf{p}_S$ and velocities $\mathbf{v}_S$ are estimated by the least-squares optimization. The results of this tests are presented in Figures 5.12(a) and 5.12(b).

It became clear that the error in the inverse estimation of surface pressures and velocities is also affected by variations in the uniformity of the mesh elements, with a tendency to increase as one or more of the elements become considerably smaller with respect to the others. This variation can be explained in terms of the numerical computations of the integrals in the acoustic BEM. Recalling that the solution of the integral equations of the Kirchhoff-Helmholtz formulation by the BEM [97] involve the calculation of singular integrals of the forms:

$$\int_S f(\vec{r})\partial_n \left(\frac{e^{-jkr}}{4\pi r}\right) dS, \qquad \text{and} \qquad \int_S g(\vec{r}) \left(\frac{e^{-jkr}}{4\pi r}\right) dS,$$

where the factors $1/r^2$ and $1/r$ respectively represent the source of the singularity. In practice, these integrals are usually approximated with numerical techniques such as Gaussian quadrature with a transformation to polar coordinates. Therefore as the surface of the integrating element becomes smaller, the singularity of the integrand increases, making the

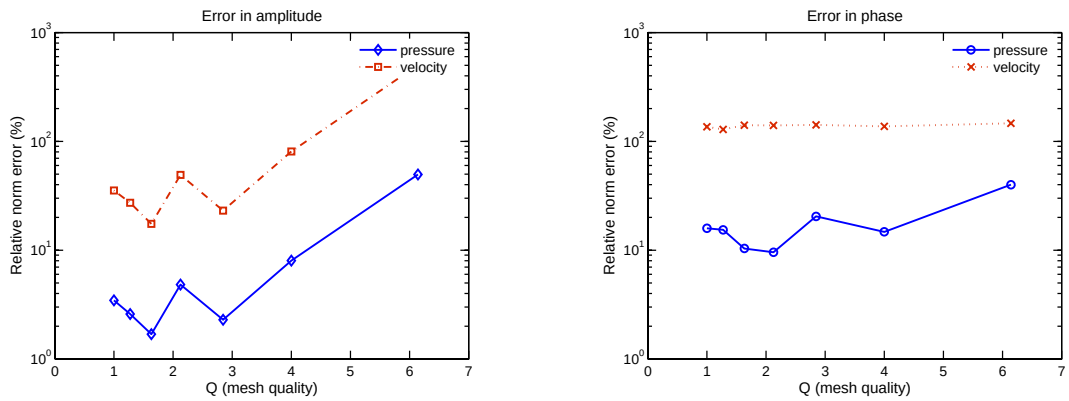

(a) (b)

Figure 5.12: Variation of the reconstruction error with the mesh quality. (a) Error in amplitude. (b) Error in phase.

approximation of the integral inaccurate. This inaccuracy is propagated when performing the inverse process, resulting in noise that is amplified by the singular values of the inverse transfer matrix. Consequently, errors are introduced in the reconstruction of p_S and v_S.

As the plots of Figures 5.12(a) and 5.12(b) suggest, there is an optimum size of the elements that can produce the best reconstruction error in the sense of the least-squares. Hence, in order to improve the accuracy, this optimum should be considered in the solution of the inverse estimation problem. This optimization process, however, is out of the scope of the present work. The balance between the size of the elements is difficult achieved basically because of two reasons: i) the BEM together with the inverse BEM are numerical techniques computational expensive by themselves, and including a mesh optimization process will require the recalculation of the BEM matrices at each step of the process, making the computational cost considerably higher; ii) there is currently no meshing method that provides full control over the sizing criterion when building the mesh. The meshing process is constrained to geometric rules that try to ensure smoothness and continuity of the mesh, ensuring thus the best approximation to the original surface.

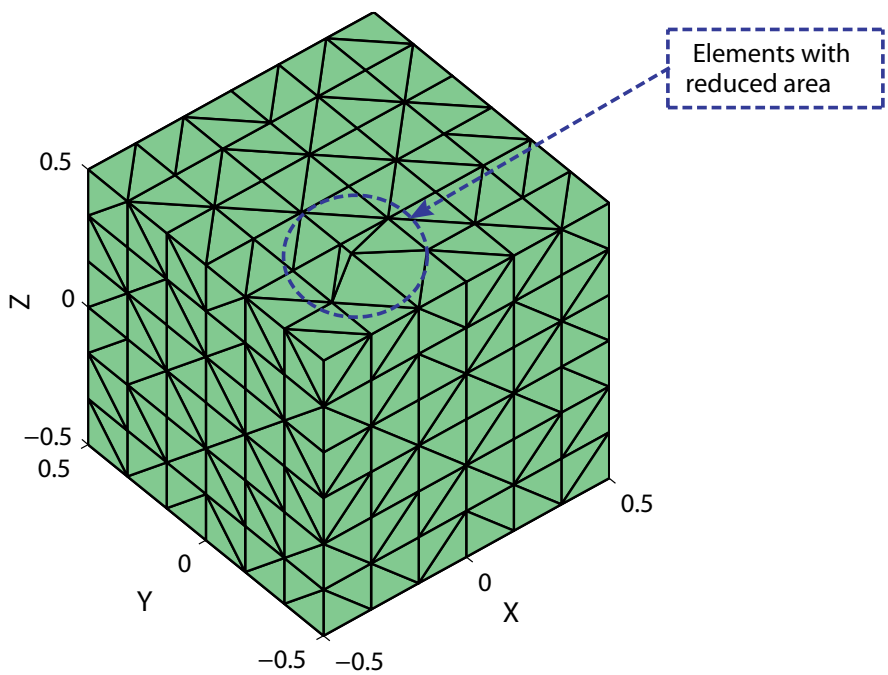

Figure 5.13: Mesh variations for the mesh quality test.

Chapter 6

Acoustic impedance estimation by an iterative optimization method

6.1 An iterative non-linear optimization approach

Strictly speaking, the impedance at every point on the surface is different depending on how the incident wave hits the surface, or the composition of the material in the incident point, etc. In this sense, the constrained least-squares optimization approach presented in the previous chapter gives approximated estimation of impedances at each element, and as the mesh elements become smaller, better approximations to the distribution of the acoustic impedance over the surface are achieved. Nevertheless, the solutions obtained by the least-squares shows large variances in some elements of the same surface type. This is a direct effect of the ill-conditioning of the transfer matrix, as it has been discussed before. Furthermore, the large variance of the solutions grow as the dimensionality of the optimization problem gets larger.

In order to eliminate these variances between neighbor elements of the same surface, the physical constrain of the smoothness of the surfaces is considered again in the following approach leading to an iterative statement of the inverse optimization problem. Let us start from the assumption that the acoustic impedance is homogeneous in each type of surface of the 3D model. This condition implies that the surfaces inside the interior space can be segmented in subareas with approximately the same properties (thickness, density, etc.) which, under the assumption of normal incidence, present only slight variations of impedance values in such a way that can be considered as constant over that subarea. Then, replacing the surface pressures p_s of the equation (5.3) by the impedances Z_s from

equation (5.1), and arranging unknown and known parameters as in (5.5), we can express equations (5.3) as follows:

$$\mathbf{A}_f \langle \mathbf{v}_s \cdot \mathbf{z}_s \rangle = -\mathbf{B}_f \mathbf{v}_s - \mathbf{p}_f, \tag{6.1}$$

where $\langle \ \cdot \ \rangle$ means element–wise product.

As described in the definition of the problem (Figure 5.1), there are n different surfaces in the room. Hence, consideration of the above assumption implies that for each l–th surface,

$$z_{s,m_{l-1}+1} = z_{s,m_{l-1}+2} = \ldots = z_{s,m_l} = Z_l, \ \text{ with } l = 1, 2, \ldots, n. \tag{6.2}$$

Here, $z_{s,m}$'s are the surface impedance values at each element of the mesh, and Z_l is the homogeneous impedance of the surface S_l. Substituting the $z_{s,m}$'s by their corresponding value of Z_l, we can reduce the system of equations (5.7) to a system with n unknown parameters as follows:

$$\begin{pmatrix} \sum_{j=1}^{m_1} a_{f,(1,j)}\ v_{s,(j)} & \sum_{j=m_1+1}^{m_2} a_{f,(1,j)}\ v_{s,(j)} & \cdots & \sum_{j=m_{n-1}+1}^{m_n} a_{f,(1,j)}\ v_{s,(j)} \\ \vdots & \vdots & \cdots & \vdots \\ \vdots & \vdots & \cdots & \vdots \\ \sum_{j=1}^{m_1} a_{f,(M,j)}\ v_{s,(j)} & \sum_{j=m_1+1}^{m_2} a_{f,(M,j)}\ v_{s,(j)} & \cdots & \sum_{j=m_{n-1}+1}^{m_n} a_{f,(M,j)}\ v_{s,(j)} \end{pmatrix} \begin{pmatrix} Z_1 \\ Z_2 \\ \vdots \\ Z_n \end{pmatrix} = -\mathbf{B}_f \mathbf{v}_s - \mathbf{p}_f, \tag{6.3}$$

or in compact form

$$\widehat{\mathbf{A}}_f \mathbf{z} = -\mathbf{B}_f \mathbf{v}_s - \mathbf{p}_f \tag{6.4}$$

where the a_f's are the elements of the matrix $\mathbf{A}_f$.

The first thing to note in equation (6.4) is the change of variable to $\mathbf{z}$. While in the problem given by equation (5.13) the unknown parameters to be estimated are the sound pressures $\mathbf{p}_S$ and the velocities $\mathbf{v}_S$ at each element, in (6.4) the values to be estimated are the homogeneous impedances of the materials. Second, because of the assumption of the surface segmentation, the degrees of freedom (DOF) of the inverse problem has been dramatically reduced from N to n, where N is the number of nodes in the mesh, and n is the number of surfaces of different properties.

Note also that the vector $\mathbf{v}_S$ in the right hand side is just partially known. In other words, the elements whose surface vibration is known are those of the sound source.

Thus, In order to solve (6.4), an initial impedance value $\mathbf{z}_{\text{init}}$ can be prescribed and start an iterative process. In the first iteration the initial $\mathbf{z}_{\text{init}}$ is substituted into the system of equations (5.2)(5.3) and solve for the boundary values which in turn will allow us to compute a set of M field pressures $\mathbf{p}_g$ at the same positions of $\mathbf{p}_f$. These two sets of field pressures are then compared at each iteration according to the following cost function:

$$\alpha = \frac{\|\mathbf{p}_g - \mathbf{p}_f\|^2}{\|\mathbf{p}_f\|^2} \leq \text{tol}, \tag{6.5}$$

where $\| \cdot \|$ indicates again the 2–norm, and tol is a termination threshold. If equation (6.5) is not satisfied then equation (6.4) is updated with the current $\mathbf{v}_s$ and solved for a new $\mathbf{z}$. Moreover, we may impose again the bounds used in the least-square solution of the previous section to give more information of the desired solution. Thus the iteration process takes the form:

$$\begin{array}{c} \mathbf{z}^{(k+1)} = \min\limits_{\mathbf{z}} \|\widehat{\mathbf{A}}_f^{(k)}\mathbf{z} + \mathbf{B}_f\mathbf{v}_s^{(k)} + \mathbf{p}_f\| \\ \text{s.t. } \ \mathrm{Z}_0 \leq \mathbf{z} \leq \mathrm{Z}_{\max} \end{array}, \tag{6.6}$$

where k is the iteration index.

In practice, this iterative approach was found to converge to small residual values and to approximations of the surface impedances. Thus the impedances are estimated directly from the iteration process (in contrast to previous approaches that compute first sound pressures and velocities). However, the drawback of this method is its slow convergence rate, taking typically hundreds of evaluations of equation (6.5). The convergence rate can be improved by using more sophisticated iterative procedures such as krylov subspace methods. This improvement is out of the scope of the present dissertation, nevertheless interested readers are referred to [93].

6.2 Numerical example: Reverberation chamber model

The performance of the iterative approach proposed in the previous section is shown with a numerical example. As usual, simulations are performed following the procedure depicted in Figure 5.3. This time, the graphic model of an experimental reverberation chamber is employed. The reason to show an example with this model is that validation experiments in the real chamber will be presented in further sections.

The chamber consists of a 30 mm–thick acrylic box of dimensions $1.37 \times 1.56 \times 0.87$m. Its 3D graphic model is generated and meshed into 314 isoparametric triangular elements

with a maximum size of 0.22 m, allowing a frequency analysis of up to 260 Hz following the $\lambda/6$ rule. Figure 2 depicts the model of the chamber.

The boundary conditions assigned to the walls of the chamber are impedance values as follows: 1000 for the walls, 2000 for the sides of the speaker, and 1 for the lateral opening of the chamber (note that these values are real-valued and normalized to Z_0, where Z_0 is here again the characteristic impedance of the air, $Z_0 \approx 415\, rayls$). It is assumed that only the circular area of the speaker is the vibrating sound source whose velocity amplitude is $1\ \mathrm{m/s}$. Under these conditions a set of $M = 1000$ field pressures are generated using BEM for a frequency of 250 Hz. In practice, the distribution of the measurement points is not perfectly uniform, however for this numerical example, uniformly distributed field points are considered. After the set of field pressures are generated, artificial noise is added. Thus, three groups of field data is obtained by including gaussian noise to the field pressures in three levels: a) Noiseless, b) $SNR = 50\ \mathrm{dB}$ and c) $SNR = 30\ \mathrm{dB}$. . Here the SNR is taken as

$$SNR = 10 \log \left(\frac{\Psi_{p_{\text{field}}}}{\Psi_{p_{\text{noise}}}} \right) = 10 \log \left(\frac{\mathbf{p}_{\text{field}}^H \cdot \mathbf{p}_{\text{field}}}{\mathbf{p}_{\text{noise}}^H \cdot \mathbf{p}_{\text{noise}}} \right), \tag{6.7}$$

where Ψ represents the total power, and $\mathbf{p}_{\text{noise}}$ is the noise component added to the field pressures.

The acoustic impedances of the boundaries are then estimated using the methods introduced in this dissertation, the constrained least-squares and the iterative optimization. The results will be compared at the end. Thus, for each group of field pressures with different levels of noise, the same set of data is used with the inverse methods mention above. For the case of the iterative algorithm, four types of surfaces are specified: the air opening, the walls of the chamber, the sides of the speaker and the circular vibrating surface of the speaker. The latter is considered as a known variable and therefore the number of unknown impedance values to be determined in the iterative process is $n = 3$. Furthermore, an initial value of $z = Z_0$ is chosen to start the iterative optimization.

6.2.1 Comparison of results: iterative vs. least-squares solutions

As can be seen in the results shown in Figure 6.3, the constrained least-squares method gives approximated solutions when the data is not severely contaminated with noise, however the element-wise values of the solution tend to degenerate greatly as the noise level grows. The poor smoothness of the solutions of this method is due to the amplification of

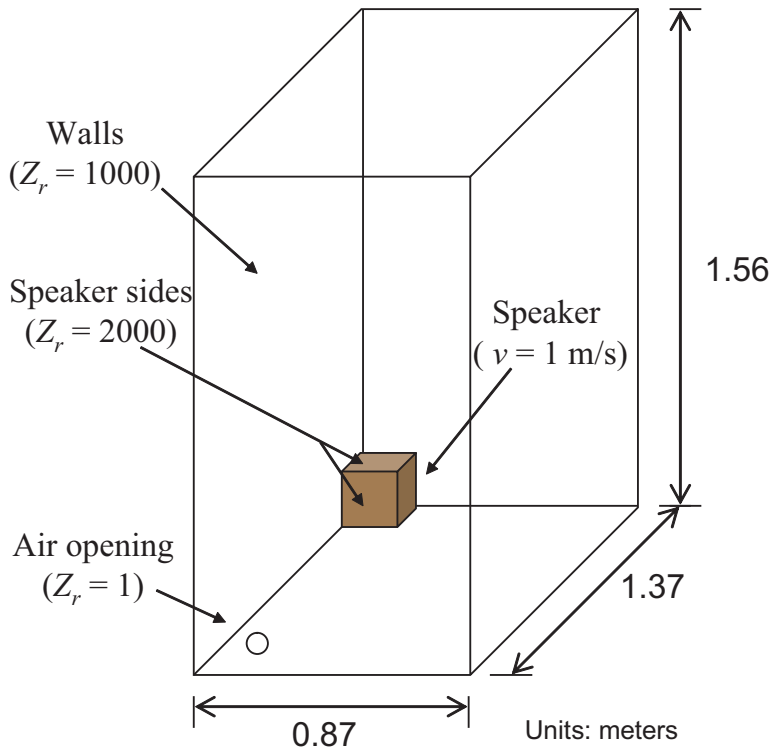

Figure 6.1: Geometric model of the reverberation chamber for the numerical simulations.

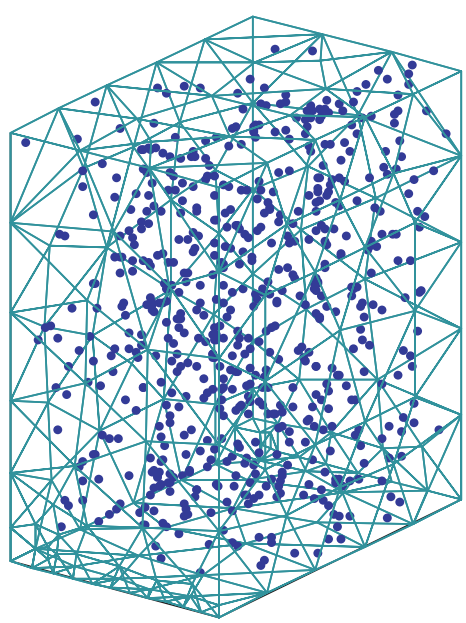

Figure 6.2: Mesh of the reverberation chamber model and 1000 field points uniformly distributed.

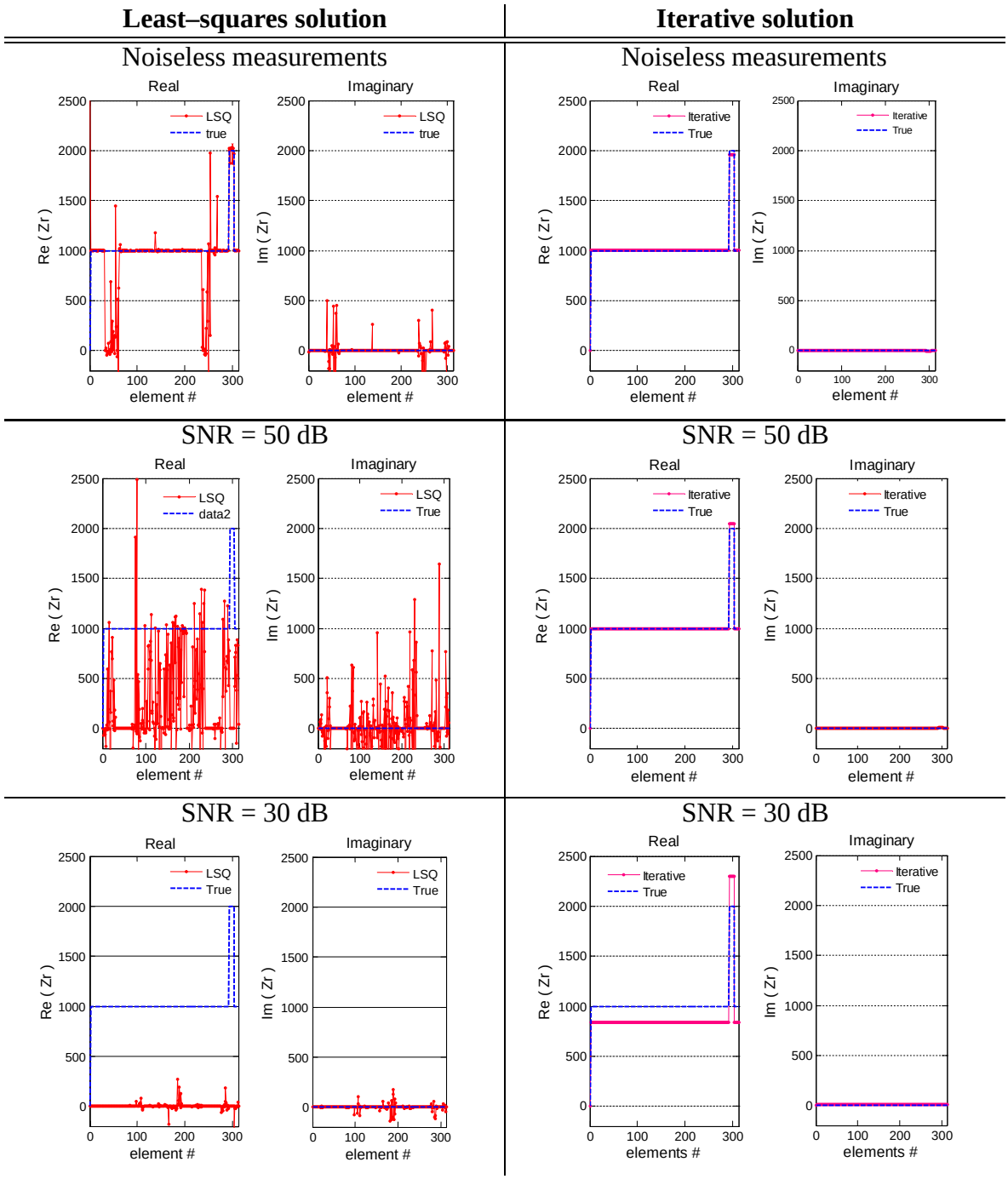

Figure 6.3: Surface impedances obtained by the Least–squares method (left column), and by the Iterative optimization approach (right column).

noise caused by the ill-conditioning of the transfer matrix. The mechanism of amplification of noise in the back reconstruction has been readily studied in previous sections and in other works in the literature, e.g. [55, 65]. An advantage of the least-squares method is the fact that the solution vector represents the impedances at each element, thus as the original surface is approximated with more elements, the distribution of the impedances over the surfaces is more accurate. However, this advantage is diminished by its vulnerability to noise in the data. In contrast, the iterative method was found to be more robust to the noisy data, achieving solution fairly close to the original impedance value even when at noise levels of $\mathrm{SNR} = 50\ \mathrm{dB}$. At higher levels of noise, e.g. $\mathrm{SNR} = 30\ \mathrm{dB}$, the estimated impedances tend to be deviated from the true value, nevertheless still achieving approximated values, (as can be appreciated in Figure 6.3, $\mathrm{SNR} = 30\ \mathrm{dB}$). Another advantage is the suppression of the element-wise large variances present in the least-squares solutions. This is a consequence of the change of variable from $(\mathbf{p}_S, \mathbf{v}_S)$ to $\mathbf{z}$ in equation (6.4). Thus, instead of solving for an element-wise vector, the solution is sought for a few impedance values of the surfaces. As discussed before, this brings the benefit of reducing considerably the dimensionality of the inverse problem. A draw back of this method is its poor convergence, taking in all of the cases of this numerical example, between 240 and 500 evaluations of the cost function (6.5) until a solution is found. In the current implementation of this algorithm no information of the gradient of the cost function, nor a search method is employed to accelerate the convergence, nevertheless in practice it was found that the method converges. The convergence of this approach is also sensitive to the starting point, i.e. the initial guess specified. Thus the selection of an appropriate initial vector is still another limitation of this method.

Chapter 7

Experimental measurements in a reverberation chamber

Numerical simulations are powerful tools to make predictions of acoustic phenomena in several areas of acoustics, however such numerical models are useless if they are not a close representation of the real phenomena, and in many cases validation experiments are needed in order to evaluate the performance of the theoretical algorithms. Hence, it is the turn of this chapter to present the experiments carried on to validate the algorithms presented in previous sections. Let us first give a brief review of the type of experiments that previous work has done.

In the area of inverse acoustic problems such as Near–field Acoustic Holography (NAH) extensive experiments have been performed by several researchers, e.g. [94, 95, 50]. Most of them have successfully achieved the reconstruction of the sound source strength from sound field measurements up to a certain accuracy which is affected by the noise contained in the actual measurements themselves and by the limitation imposed by the ill–posedness which dramatically increases as the dimensionality of the problem grows. Furthermore, carefully performed experiments in the radiation case, [54, 55], have shown that in order to recover the particle velocities of the vibrating surface the position of the microphones with respect to the discrete representation of the sound source should be optimally chosen so that the condition number of the transfer matrix is best for the inverse solution. According to Nelson et. al., [54], this optimal conditioning is achieved when the number of discrete sources is small, when the geometrical arrangement of the microphones closely matches the assumed source array geometry, when the distance between the sources is the same as the distance between the microphones, when the microphone array is placed close to the source array and when the sensor array is positioned symmet-

rically with respect to the array. Although these conditions seem to ensure a successful reconstruction of the vibro–acoustic parameters of the vibrating surface, they represent serious limitations when the measurements are to be performed in real situations where the geometry of the surfaces is rather complex. On the other hand, when considering the estimation of the impedances of the surfaces in a room, optimal placement of the microphones is even more complicated. Moreover, large–scale problems, such as those being targeted in the present work, demand also large amounts of measured data (of the order of hundreds or thousands of fields pressures) making the construction of such microphone arrays impossible. It is thus that in the following sections a system that allows measurement of large amount of data is introduced. And with the use of this data acquisition technique experiments in a reverberation chamber are presented as well.

7.1 Implementation of a real-time system to measure sound pressure

7.1.1 Mass acquisition of sound pressure data

Inverse estimation of the acoustic impedance of the interior surfaces involves the solution of an overdetermined linear system of equation given by (5.7). The size of this matrix system depends on the dimensions and shape of the geometry of the interior space. If real spaces, e.g. an office room, is to be under consideration, the discretization of the 3D model into N elements leads to a BEM system of at least N equations, therefore the solution of the overdetermined linear system (5.7) requires $M \geq N$ measurements of sound pressure in the interior fields. This is impossible if an array of microphones is to be used for a large space. However, in order to overcome this problem a real-time measuring system that requires only one microphone is proposed. The basic idea is depicted in Figure 7.1.

While a sound source (e.g. a speaker) is radiating sound into the interior field, a microphone is continuously measuring the sound pressure as it moves freely in space, thus acquiring in real–time as many measurements as desired at the positions of interest. The recording time is set so as to match a suitable number of field points per minute, and the speed of the moving microphone is limited by the wavelength of the analysis frequency. Under the assumption that the wavelength is comparably bigger than the maximum distance walked by the microphone per second, the Doppler effect is neglected. For example, if the wavelength of the emitted sound is $\lambda = 1.37$ m/s (≈ 250 Hz), the maximum speed

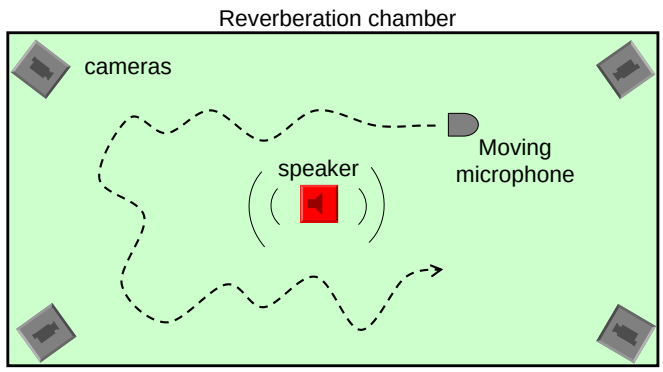

Figure 7.1: Real-time acquisition of the sound field pressures in a room.

of the moving microphone is limited to 13.7 cm/s.

Recalling now that in equation (5.7) the sought parameter is the acoustic impedance Z_s of each surface which is given by the relation between the complex surface pressure p_s and the complex particle velocity v_s as

$$Z_s = \frac{p_s}{v_s},$$

and as discussed in chapter 4, the data that is given as input to the inverse estimation process are the geometry of the model, the vibration velocity of the sound source, and a set of sound pressures p_f measured in the interior field. The geometric model is constructed using 3D CAD software, therefore the data that is to be measured is the amplitude velocity of the vibrating source v_{source} and the sound pressures p_f. Thus the acquired parameters are of the form:

$$\begin{aligned} v_{\text{source}} &= |\mathrm{V}| \exp^{(j\omega t + \theta_v)}, \\ p_f &= |\mathrm{P}| \exp^{(j\omega t + \Delta\theta)}, \end{aligned}$$

where $|\mathrm{V}|$ and $|\mathrm{P}|$ are the amplitudes of the source vibration and the field pressure respectively, θ_v is the initial phase of the sound source, and $\Delta\theta = \theta_{\mathrm{p}} - \theta_v$ is the phase of the sound pressure at a field point with respect to the phase of the sound source. For a steady state analysis the time factor can be omitted, and setting the $\theta_v = 0$ the above expression become

$$v_{\text{source}} = |\mathrm{V}|, \tag{7.1}$$

$$p_f = |\mathrm{P}| \exp^{(\theta_{\mathrm{p}})}. \tag{7.2}$$

Therefore the parameters to be directly measured from the experiments are $|\mathrm{V}|$, $|\mathrm{P}|$ and θ_{p}. Furthermore, for ease of calculations when handling the data in the impedance estimation process, the measured parameters can be normalized and thus the fields pressures and vibration amplitude of the source become

$$v_{\mathrm{source}} = 1, \tag{7.3}$$

$$p_f = \frac{|\mathrm{P}|}{|\mathrm{V}|} \exp^{(\widehat{\theta}_{\mathrm{p}})}, \tag{7.4}$$

where $-180^{\mathrm{o}} \leq \widehat{\theta}_{\mathrm{p}} \leq 180^{\mathrm{o}}$.

The phase of the sound pressures p_f are directly obtained by comparison of the sound source and the microphone signals, however care should be taken by considering the phase delay introduced by the measuring devices that may result in inaccurate measurements. These inaccuracies have a big impact on the accuracy of the acoustic impedance estimated by the inverse process presented previously. As an example, Figure 7.2 shows the phase delay (in degrees) introduced by the Measuring Amplifier B&K Type 2610 used for the experimental validation. Finally the amplitude of the source vibration is obtained using a Laser Doppler Vibrometer (LDV) B&K Type 8329 which points to the center of the vibrating cone of a speaker when it is used as sound source. The LDV B&K Type 8329 is sensible to vibration velocities from $65\ \mu\mathrm{m/s}$ to $425\ \mathrm{mm/s}$ within a range of frequencies of 0.1 Hz to 25 kHz. The physical aspect of the LDV B&K Type 8329 is shown in Figure 7.3.

7.1.2 3D tracking of a moving microphone

Besides the sound pressure measured at each sampling point, the position in 3D space of each measurement of field pressure is also required by the inverse BEM process. Here, traditional techniques employ mechanic systems that move the microphone some distance that is known by the automated system and thus the location of the measurement point is obtained at each step. However these kind of mechanic systems are usually expensive and their installation is constrained by geometric aspects. In the present work a set of cameras is employed to overcome this limitations. As illustrated in Figure 7.1 an array of cameras is installed in the interior of the room. The cameras perform then the 3D acquisition by tracking in real–time the position of the moving microphone.

The use of cameras for 3D tracking requires extra processing and Computer Vision techniques but they bring other benefits:

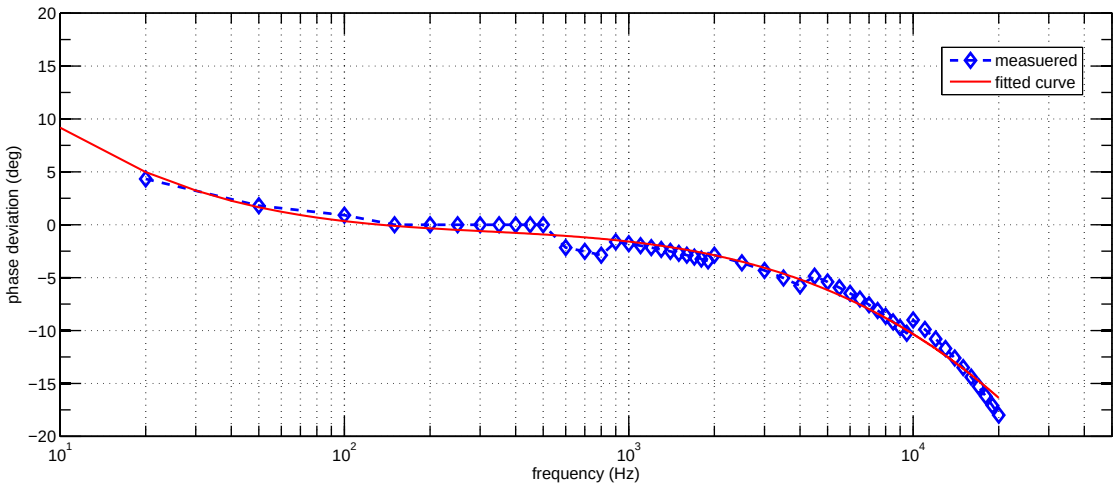

Figure 7.2: Phase delay introduced by the measuring amplifier B&K Type 2610.

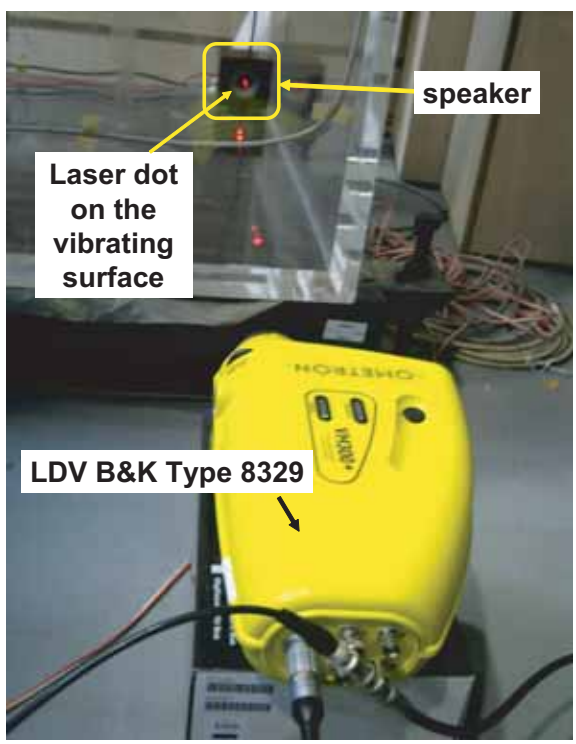

Figure 7.3: Physical aspect of the Laser Doppler Vibrometer B&K Type 8329.

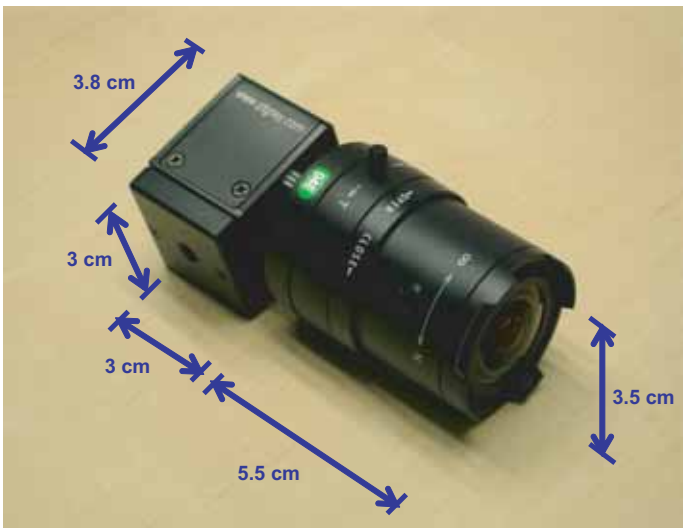

Figure 7.4: Size of the video cameras used for the 3D tracking implementation.

- Free placement of the microphone inside the room.
- Instantaneous relocation of the microphone in a new position (rea–time traking).
- Low–cost mass data acquisition.
- Acquisition of extra information via computer vision techniques (such as automatic surface segmentation of the 3D geometric model from the images of the room).

On the other hand, recent advances in the Solid State engineering area have enable the manufacture of tiny image sensors (CCD) that result in the construction of small video cameras. It is then assumed that the acoustic scattering effect due to the cameras is negligible when comparing the size of the actual video camera with the wavelength of the test frequency. Figure 7.4 shows the size of the cameras used for the 3D tracking implemented in this work. The cameras used in these experiments are compact digital cameras by the maker Point Grey, [68], model Flea (IEEE 1394a). These cameras have a color $1/3$" CCD and are able to transmit 30 fps at a resolution of XVGA to the computer through the interface IEEE–1394.

In order to facilitate the detection of the microphone by the video cameras a small lamp is attached to the microphone. Again, the relative size of the lamp is small enough so as to neglect the acoustic scattering effect produced by the lamp. In Figure 7.5 the mounting of the microphone and the lamp, together with the actual installation of the video cameras in a reverberation chamber is depicted.

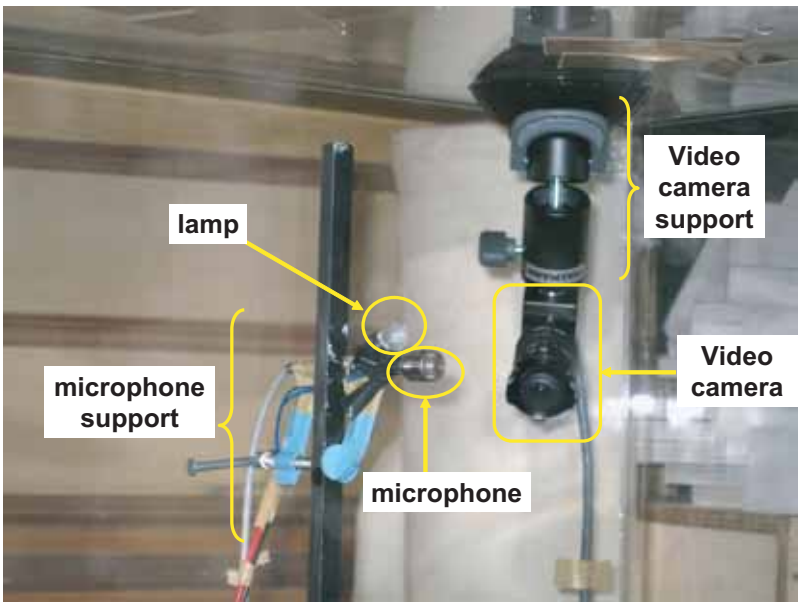

Figure 7.5: Actual mounting of the set microphone–lamp and a video camera.

7.2 Experiments in a rigid reverberation chamber

7.2.1 Experimental setup

After the description of the implementation and the devices employed, this section describes a real experimental case in which the impedances of the interior surfaces in rigid reverberation chamber is estimated by the methods proposed in the present work.

The model consists of rigid box made of 3 cm–thick acrylic walls with dimensions as depicted Figure 7.6. This chamber is available for experiments at the Institute of Industrial Science of The University of Tokyo.

First of all the calibration of the cameras for the 3D tracking is performed only once in order to get accurate locations of the moving microphone. Regarding the 3D tracking, there is already a number of software available for general purpose computer vision purposes, and a good theoretical introduction to this area can be found in [33].

Next, the microphone is placed on a movable vertical support to allow free displacement. This kind of mounting allows only two degrees of freedom, therefore the microphone is relocated at different hight levels on the vertical supporting stick after a number of field pressures were taken in one level. The more levels we take the more coverage of the interior volume space is achieved. Note that while the microphone is moving freely

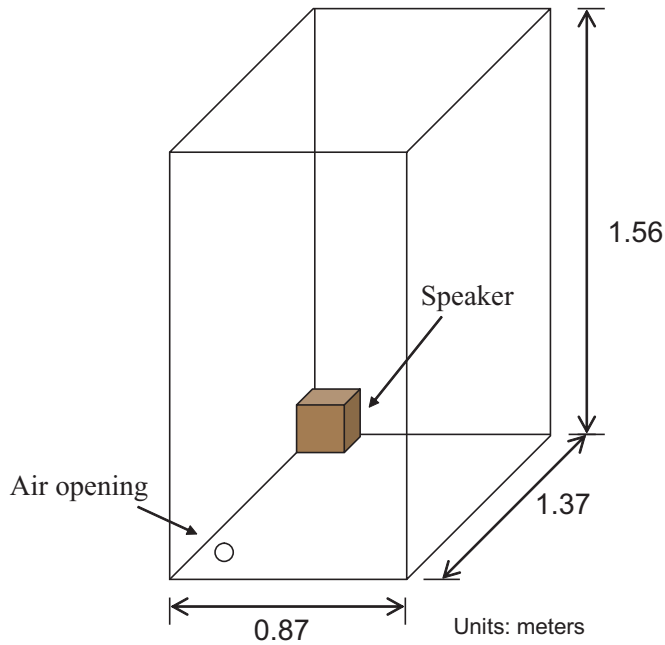

Figure 7.6: Dimensions of the reverberation chamber.

in space, a sinusoidal tone is being emitted by the speaker which is placed at one of the inferior corners. At the same time, the LDV senses the vibrations of the speaker and provides the corresponding signal into the computer system. The analog signals (from the measuring amplifier and the LDV) are interfaced to the computer through the RME Hammerfall DSP Multiface, [74] which offers up to eight analog input channels.

The general setup of the devices for the experiments in the reverberation chamber is displayed in the diagram of Figure 7.7, and the actual chamber together with the experimental setup is shown in the picture of Figure 7.8. As can be appreciated in Figure 7.8, the chamber has an rectangular window that allows access to its interior. During the measurement process, this window is closed by placing the corresponding acrylic plate which fits smoothly into the opening, in a way that all of the sound is practically confined to the interior of the chamber.

On the other hand, since the inverse estimation of acoustic impedances is based on the BEM theory, the measurements of fields pressures p_f have to be performed in a steady-state sound field. Therefore, a set of measurements is taken for each analysis frequency of interest. The experiments presented here are performed for the following frequencies: 125 Hz, 250 Hz, 500 Hz, 1 kHz.

With the current implementation of the data acquisition system the following steps are

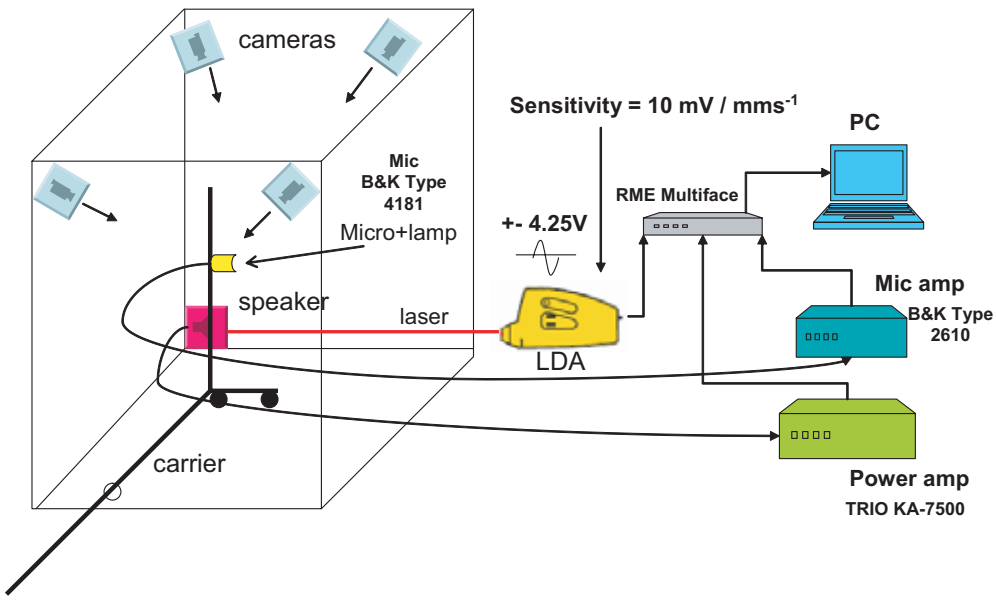

Figure 7.7: Diagram of the experimental setup in a reverberation chamber.

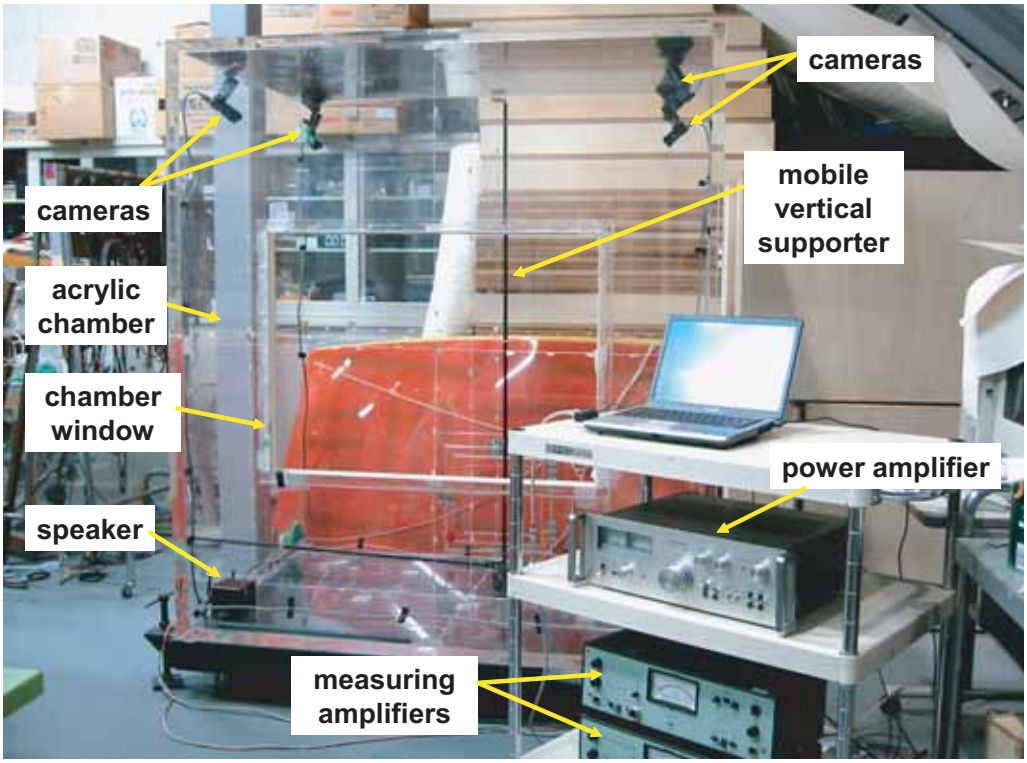

Figure 7.8: Picture of the actual setup of the experiments.

executed for each test frequency:

1. Attach the microphone–lamp to a fixed hight level of the vertical mobile supporter.
2. Set the output tone to the frequency of interest and emit the sound through the speaker.
3. Start the 3D tracking.
4. Start recording the sound from the microphone while displacing the vertical supporter all over the interior volume until the desired number of fields pressures for that level is acquired.
5. Reallocate the microphone–lamp set in a different hight level and repeat from step 3.
6. The measurement process is finished when the total number of field pressures is achieved.

One point to remark is that, the amplitude of the emitted sound is chosen loud enough so as to ensure a high signal to noise ratio (SNR), but at the same time it should not be so large to cause a non-linear response of the acrylic box which would result in wrong measurements of sound pressures. For the case of the experimental chamber used here, an output power of approx. 3 watts was set so that the output sound is large enough compared to the noise produced by the the movement of the vertical supporter. The noise coming from the exterior of the box is considered negligible because the chamber is located in the interior of a quiet experimental room.

7.2.2 Performance of the data acquisition system

When the matrices of the inverse BEM process are computed, knowledge of the position of the measurement points is required. If the coefficients of this matrices are calculated at wrong positions the final effect is the introduction of errors in the estimation of the acoustic impedances. Therefore it is of our concern that the 3D tracking performed by the set of cameras provides accurate coordinate positions of the measurement points.

As for the implementation done in the present work, the tracking system showed to work satisfactorily, achieving an average 3D reprojection error of $\approx \pm 3.5$ cm. In [33],

an introduction to stereo reconstruction from images is given, as well as the definition of the *reprojection error* as a measurement of the 3D reconstruction, together with other measures of the 3D accuracy in stereo vision systems. For the case of the experiments in the reverberation chamber, Figure 7.9 shows an example of the 3D reprojection error which has been plotted in terms of an estimation of the actual position of the measurement points.

From the set of measured data, the points with large 3D-position error can be in addition filtered out by simply applying a threshold. For example, one can select all the measurements that are associated with a maximum error of 20 mm deviating from the estimated actual position, and discard all those which exceed that value. It is worth to note that most of the measurements with large 3D reconstruction error in the experiments of this work, correspond to the measurements acquired near the corners of the chamber. In Figure 7.10 this effect can be observed, where a slight curvature of the plane formed by the measurement points is more evident near the corners of the box. This effect is due to the non–linear distortion produced by the lens of the cameras itself. As the tracked object moves away from the principal axis of the camera lens, the light rays that finally arrive to the CCD of the camera are more refracted by the lens. Since the refraction coefficient of the lens is not perfectly uniform over the complete lens, additional distortions are introduced, therefore resulting in noise that affect the accuracy of the 3D tracking. This difficulty can be overcome by pointing the cameras to the volume space of interest so that the microphone will move within the range of the principal axis of the lenses.

In general, the availability of a real–time tracking system enable us to perform measurement of large amounts of sound pressures. This system may also be used for other applications where mass acquisition of sound pressures is needed together with their coordinate positions in a 3D space. The sound pressure field can then be visualized straightforward. For example, with 3000 sample points taken inside the reverberation box, the distribution of the sound field can be easily observed, as depicted in Figure 7.10. The only requirement in the current implementation is the calibration of the cameras once they are installed in fixed locations. This calibration step is fully automated. The calibration software used in this work is part of a project run by Svoboda et. al., [86], and it is available as a toolbox for MATLAB at [85]. Regarding the acquisition of the sound pressures, this task is straightforward after some signal processing, and it does not require extra calibration steps.

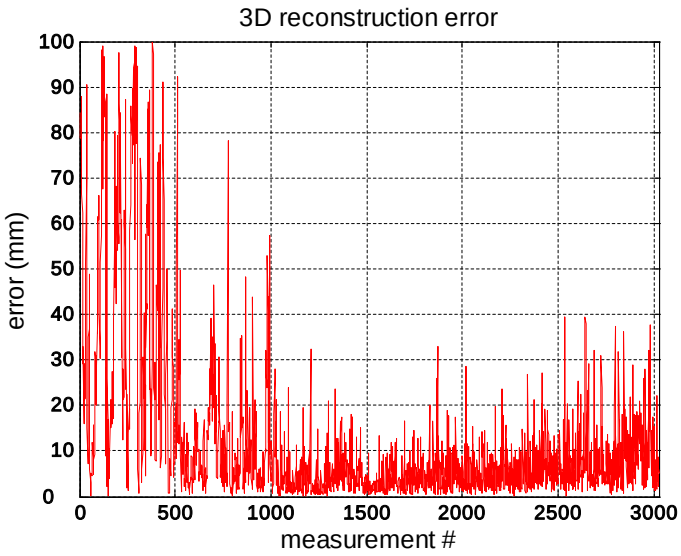

Figure 7.9: Example of 3D reprojection error of the tracking system with cameras.

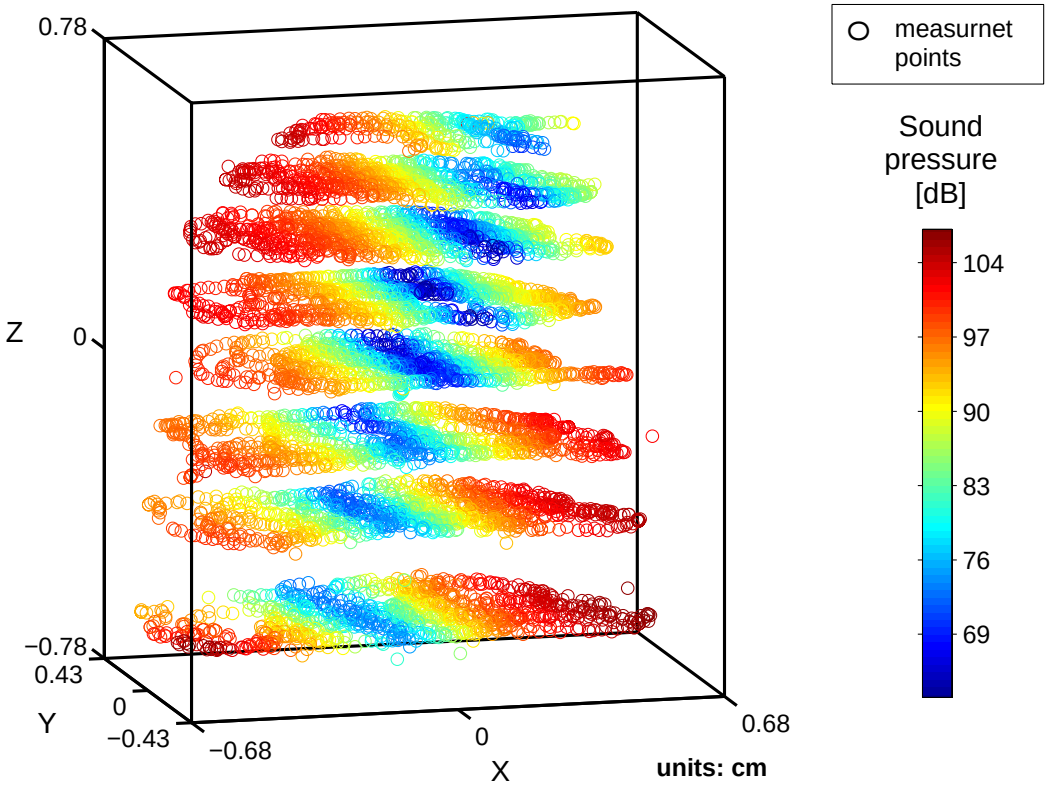

Figure 7.10: Example of 3000 3D-points acquired by the cameras-array. The microphone is randomly moved along planes XY at different Z levels inside the box while measuring the sound pressure. The frequency in this example is 125 Hz.

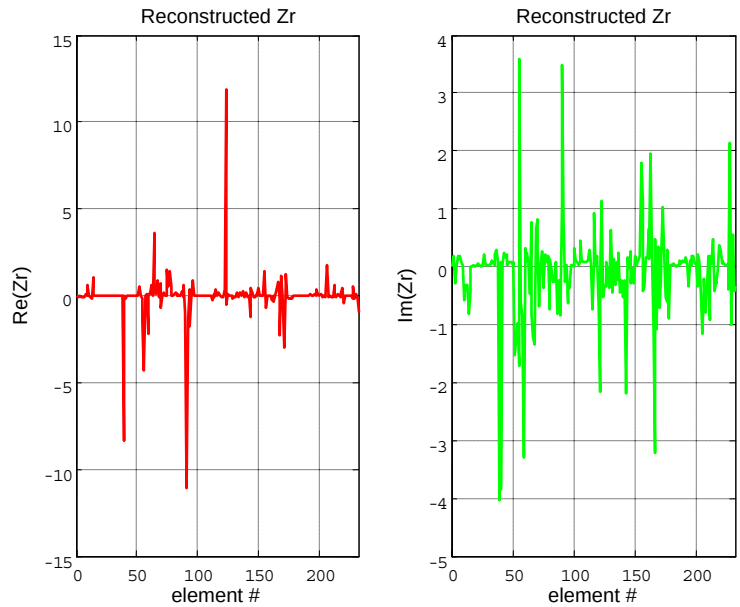

Figure 7.11: Impedance values calculated by the constrained leas–squares approach using experimental data at 125 Hz.

7.2.3 Estimated acoustic impedances by the constrained least–squares algorithm

After the measurements are performed for each specified frequency as discussed in the previous section, the data is then processed and used for the estimation of the acoustic impedances of the surfaces. First, the constrained leas–squares method described in chapter 5 is used for that purpose.

Recall that this method requires the solution of the minimization problem

$$\min_{\mathbf{x}_S} \quad g(\mathbf{x}_S) = \|\mathbf{D}\,\mathbf{x}_S - \mathbf{d}\|^2 + \lambda\|\mathbf{G}\,\mathbf{z}(\mathbf{x}_S)\|^2$$

$$\text{with} \qquad \mathrm{Z}_0 < \mathbf{z}(\mathbf{x}_S) < \mathrm{Z}_{max}$$

the matrices **D** and **G** are computed directly form the geometry of the interior space, then the vector **d** that includes the measured data is calculated as specified in equations (5.6) and (5.7). For the impedance bounds Z_0 and Z_{max}, it is considered that the lower relative impedance present in the interior surfaces, is that of the acoustic media (air, $\mathrm{Z}_r = 1$), and a maximum value of $\mathrm{Z}_{max} = 19277$ which corresponds to a standard concrete wall. With all the data available the least-squares solution is obtained by solving the problem given above using routines implemented in a commercial software such as MATLAB. The

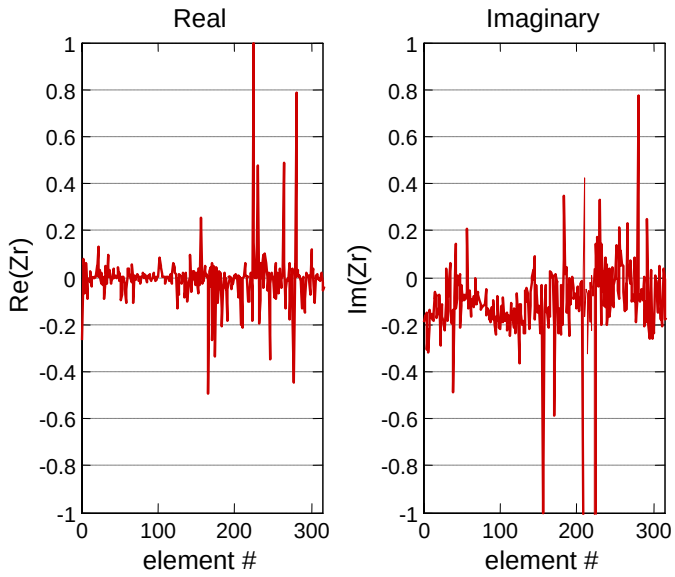

Figure 7.12: Impedance values calculated by the constrained leas–squares approach using experimental data at 250 Hz.

process takes a few minutes before a solution is obtained. Figures 7.11 and 7.12 show the impedance values obtained with this method.

As expected, the influence of the noise level in the measurements affects the accuracy of the least-squares solution. Similar results have been obtained in experiments realized by other researchers (e.g. [55]), with applications to radiation problems.

In order to investigate the levels of noise that produce erroneous solutions such as that shown in Figures 7.11 and 7.12, test simulations are performed again using the 3D model of the reverberation chamber (which has been already presented in Figure 7.6). By manually assigning impedance values to the walls of the chamber, a set of field points are synthetically generated at the same positions as the experimental measurements inside the real chamber. This time, the correct impedance values to be recovered from the inverse estimation process are $Z_{walls} = 348 + 0j$ and $Z_{air\ opening} = 1 + 0j$. Note that this values are relative to Z_{air}. In addition, different levels of artificial noise are introduced to the computed field pressures. The groups of data are then used to estimate the impedance values by the constrained least-squares. Finally, Figure 7.13 illustrates the results obtained at each of these different noise levels.

Observe that as the magnitude of the noise contained in the field pressures grows, the

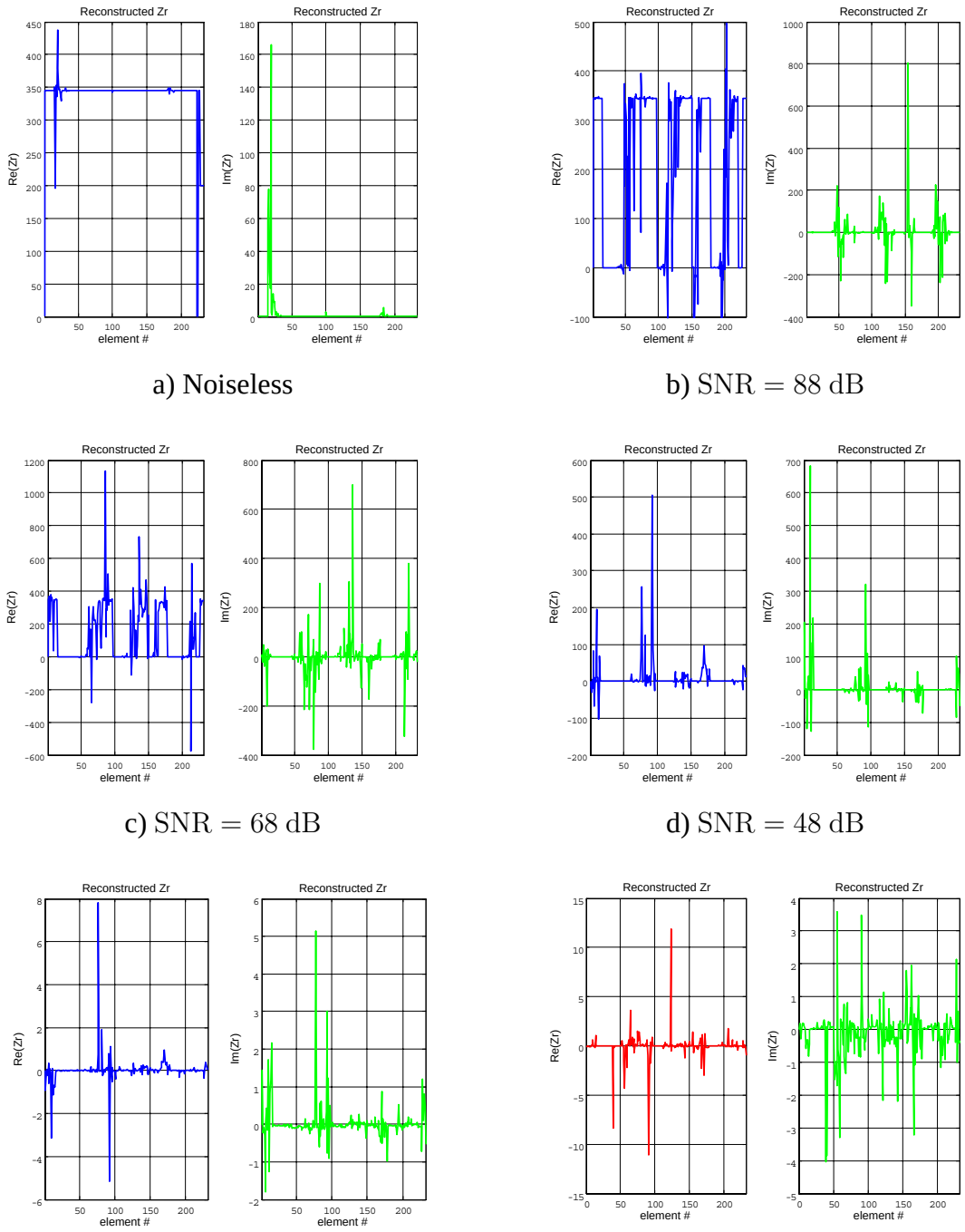

a) Noiseless

b) $\mathrm{SNR} = 88\ \mathrm{dB}$

c) $\mathrm{SNR} = 68\ \mathrm{dB}$

d) $\mathrm{SNR} = 48\ \mathrm{dB}$

e) $\mathrm{SNR} = 28\ \mathrm{dB}$

f) Experimental

Figure 7.13: Surface impedances obtained by simulations with different levels of noise in the field pressures: a)Noiseless, b) SNR = 88 dB, c) SNR = 68 dB, d) SNR = 48 dB, e) SNR = 28 dB, f) Same results as Figure 7.11 displayed here again for comparison purpose.

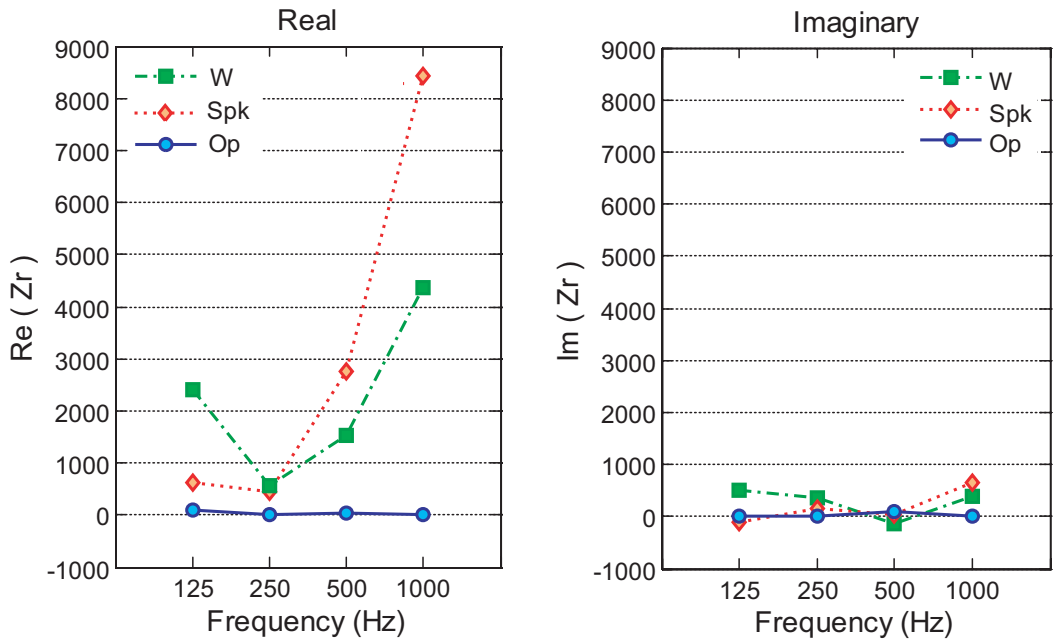

Figure 7.14: Experimental impedance values at the surfaces of the empty reverberation box estimated by the iterative approach. Surface types: **Spk** - rigid sides of the speaker, **W** - rigid walls of the chamber, **Op** - air opening in a lateral side of the chamber.

least-squares solution tends to degenerate dramatically. And at a noise level of $\mathrm{SNR} < 30$ dB, the impedance values obtained by the test simulations are similar to those obtained using the original experimental data. This can be appreciate it by comparing Figure 7.13e and Figure 7.13f – the latter is the same as Figure 7.12 put here again for comparison purposes. This fact suggests that the total level of actual noise introduced during the measurements and the inverse estimation process is of the order of $\mathrm{SNR} < 30$ dB. Which is in fact a level of noise ratio usually found in acoustic measurements. Thus if a higher SNR cannot be ensured this method have serious limitations that overweight its efficiency of computation compared with the iterative approach.

7.2.4 Estimated acoustic impedances by the Iterative optimization approach

In summary, it has been seen from experimental evaluations that the least-squares approach fails to estimate accurately the acoustic impedance values of the surfaces when using real data contaminated with noise.

Let us turn now to present the results obtained by the the second approach proposed

in this work. Using the same experimental data as in the above test, the measured pressures are used to construct the matrices of the iterative optimization formulation given in equation (6.6). As indicated in this method, the field pressures are introduced directly into the optimization process. On the other hand, the matrix $\mathbf{A}_f$ and the vector $\mathbf{v}_s$ have to be updated at each iteration k. Hence, for the first iteration, an starting initial value of $\mathbf{z}$ is prescribed as $\mathbf{z} = \mathbf{1}$ (i.e. the initial guess starts from the impedance value of the acoustic media) and using precomputed BEM matrices, the matrix $\mathbf{A}_f$ and the vector $\mathbf{v}_s$ are updated. After giving a initial guess, the iterative process runs automatically until a specified accuracy of the solution is achieved indicating that equation (6.5) has been satisfied. In this experiment three different types of surfaces is considered as follows: 1)the air opening at one corner, 2)the plain walls of the reverberation box and 3)the hard sides of the speaker. Therefore, in the iterative process the number of unknown optimization variables is $m = 3$. This optimization process is repeated for each analysis frequency: 125 Hz, 250 Hz, 500 Hz, and 1 kHz. Figure 7.14 presents the complex impedance values obtained using the iterative optimization approach and the experimental data of this first experiment.

In practice, it is fairly complicated to measure the actual impedance value of the rigid walls in the interior of the reverberation box by employing other techniques different from those introduced in this work, and therefore a lack of reference data impede proper comparisons. Nevertheless, as expected, the estimated impedances display large absolute values at the solid walls and the sides of the speaker since these surfaces are basically rigid boundaries. On the other hand, it is also noted that the impedance at the air opening area is near the value Z_{air}, as we may readily predict.

Although the experimental results above would seem to agree in a first glance with empirical knowledge, it can be concluded that the experimental conditions of an empty reverberation box (with plain rigid walls) are not appropriated for the validation of the iterative impedance estimation approach. Hence, one way to get more meaningful results would consist on installing other materials in the interior walls of the chamber and performing experiments again to obtain the impedance of those materials. Naturally the impedances of these materials should be known in advance by measuring their acoustic impedance values with other methods and under similar conditions (temperature, humidity, etc.).

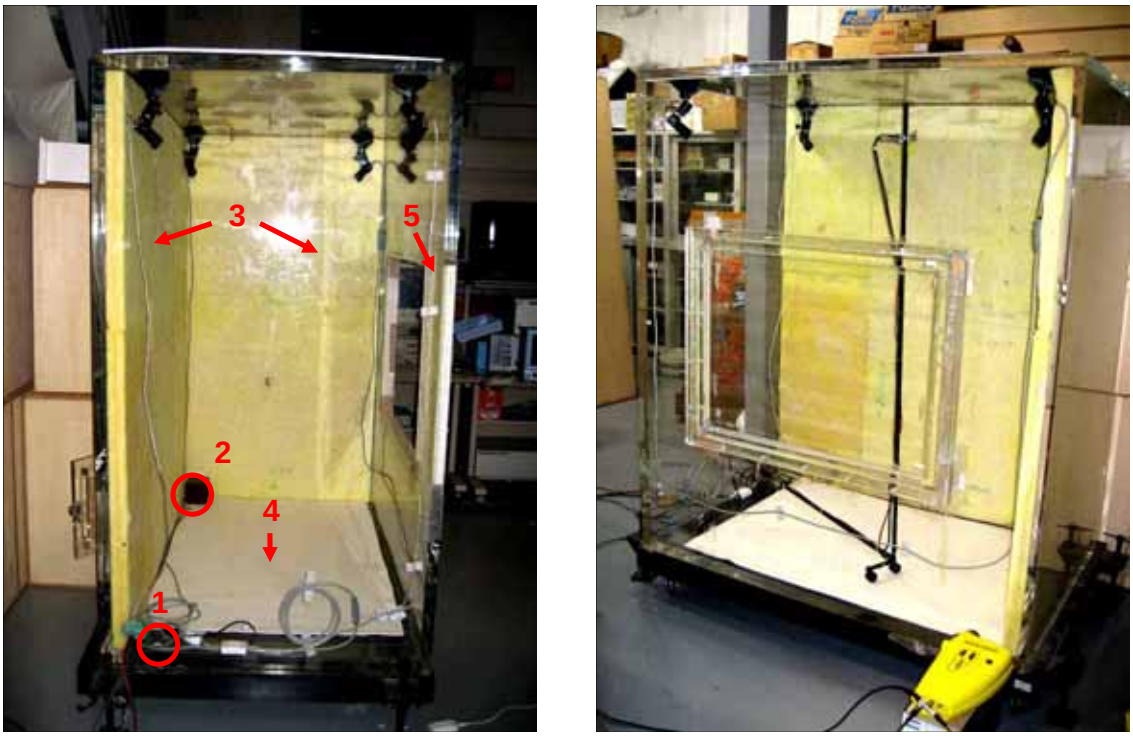

(a) (b)

Figure 7.15: Setup for a validation experiment with impedance boundaries. Five types of impedance boundaries are considered: 1) air opening, 2) hard sides of the speaker, 3) 50 mm–thick glass wool, 4) 5 mm–thick wool felt, 5) rigid walls.

7.3 Validation experiments with impedance boundaries

7.3.1 Experimental setup

A second experimental case is presented. The reverberation chamber is employed again but this time acoustic absorbent materials are installed in some of the walls of the chamber. The two absorbent materials used here are: 1) 50 mm–thick glass wool placed in two lateral walls, and 2) 5 mm–thick wool felt lying on the floor of the chamber. Figure 7.15 shows the distribution of these materials inside the reverberation box. In order to have closer approximation of local reaction of the materials (specially of the 50 mm–thick glass wool) it is important to ensure the best fit between the absorbents and the rigid surfaces. Moreover, the glass wool is extended over a complete wall fitting properly the edges of the neighbor walls, as can be seen in Figures 7.15a,b.

With this setup, five different types of surfaces are considered, and therefore five different impedance values are expected. Of particular interest is to compare the acous-

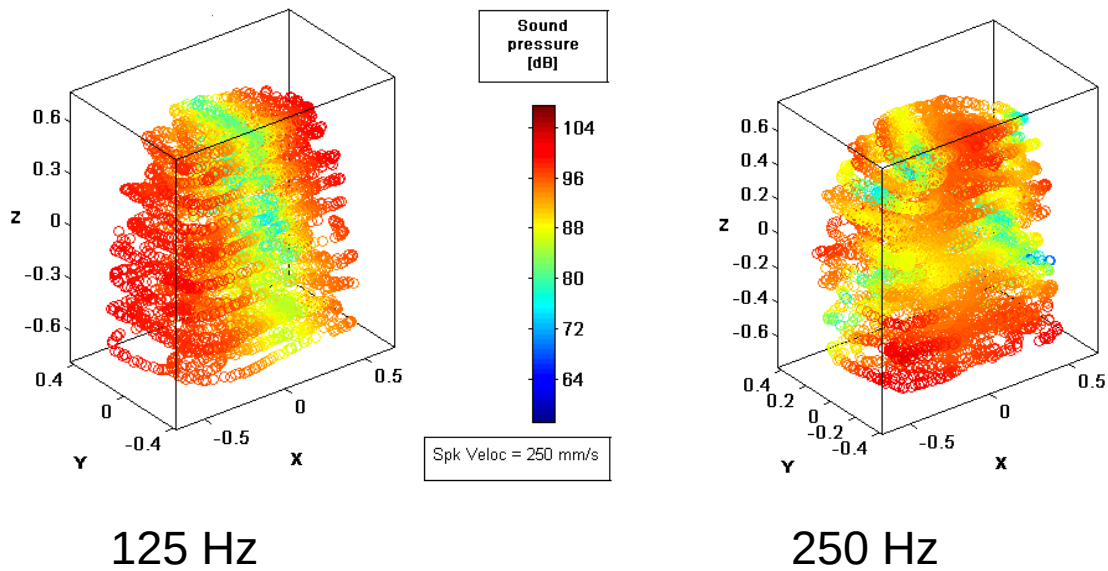

Figure 7.16: Example of field pressures acquired from the experiments with absorbent materials at 125 Hz and 250 Hz.

tic impedance of the acoustic absorbent materials estimated by the iterative optimization method with the impedance values of the same materials measured with another method. For this purpose, the standardized impedance tube method [35] was employed to measure in advance the acoustic normal impedance of the absorbents, (see Appendix A).

With the above experimental setup, data of field pressures is acquired at frequencies 125 Hz, 250 Hz and 500 Hz. Figure 7.16 shows an example of the field pressures measured at the first two frequencies. The vibration velocity of the speaker was fixed to $250\ \mathrm{mm/s}$ for all the analysis frequencies, thus Figure 7.16 gives a direct comparison reference of the sound pressure levels produced in the interior of the chamber at each frequency.

7.3.2 Performance and results

The acquired data of this second experimental setup is then used as input for the inverse estimation of impedances with the iterative approach. In this case the optimization problem defined in equation (6.6) is stated as follows:

$$\mathbf{z}^{(k+1)} = \min_{\mathbf{z}} \|\widehat{\mathbf{A}}_f^{(k)}\mathbf{z} + \mathbf{B}_f\mathbf{v}_s^{(k)} + \mathbf{p}_f\|$$
$$\text{s.t.}\ \ (\mathrm{Z}_{\min} = 1) \leq \mathbf{z} \leq (\mathrm{Z}_{\max} = 1000),$$

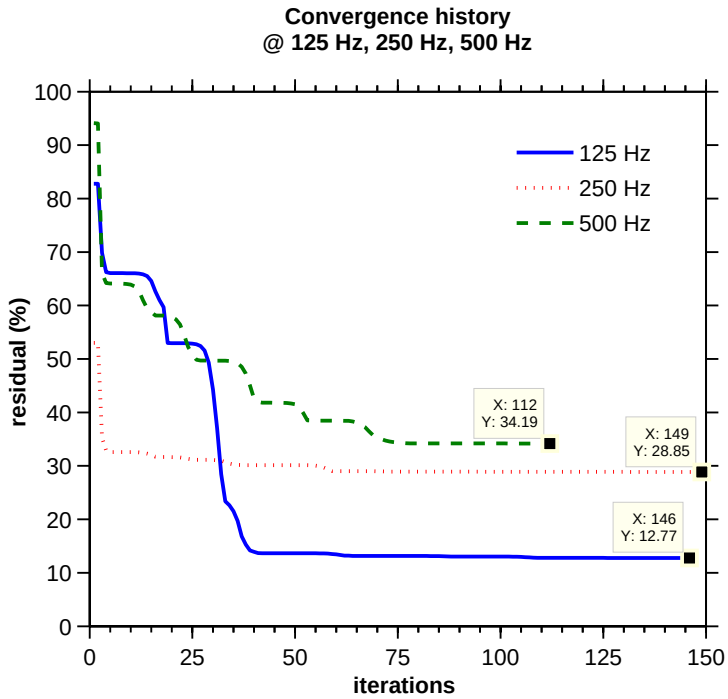

Figure 7.17: Example of field pressures acquired from the experiments with absorbent materials at 125 Hz and 250 Hz.

where $\mathrm{Z}_{\mathrm{min}} = 1$ is the lower bound for the solution space and corresponds to the relative impedance of the acoustic media (air in this case), and similarly $\mathrm{Z}_{\mathrm{max}} = 1000$ is a prescribed upper bound. Note that since five different types of surfaces are considered in this experiment the dimensionality of the optimization problem is $\mathrm{DOF} = 5$. Furthermore, the initial impedance guess is set as $\mathbf{z}_{\mathrm{init}} = 1 + j0$. The iterative process is then started and the iterations are stopped until no further improvement of the residual is achieved. One of the drawbacks of the iterative optimization approach proposed here is its low convergence. This effect can be observed in Figure 7.17 where the number of iterations vs. the residual error (%) is plotted for the estimation process at each frequency. The minimum residual error achieved is 12.7% at 125 Hz. Note that after the residual error falls abruptly the iterations are followed by small improvements of the solution. The process is stopped after a minimum threshold of improvement is achieved. If the iterations are not stopped in this way, the iterative solutions start to be dominated by random errors.

In spite of the mentioned drawback of this method, it proved to be robust to the noise levels inherent to the measured data. In a first glance, the solutions at each analysis frequency seem to agree with our empirical a priory guess that the impedances at the hard surfaces should be much higher than the soft surfaces of the absorbent mate-

@ 125 Hz

surface	Material	Ideal		Tube		Exp.	
		Re	Im	Re	Im	Re	Im
1	Air op.	1	0	-	-	0.67	0.075
2	Rigid (Speaker)	+-Inf	+-Inf	-	-	41.45	-0.1
3	Glass Wool	-	-	1	-7	2.35	-7.96
4	Felt	-	-	3	-27	0.66	-5.05
5	Rigid (walls)	+-Inf	+-Inf	-	-	259.4	-74.63

Table 7.1: Comparison of impedances (impedance tube vs. experimental) at 125Hz.

@ 250 Hz

surface	Material	Ideal		Tube		Exp.	
		Re	Im	Re	Im	Re	Im
1	Air	1	0	-	-	0.5	-0.42
2	Rigid (Spk)	+-Inf	+-Inf	-	-	30.6	-40
3	Glass Wool	-	-	0.7	-3.5	1.87	-1.34
4	Felt	-	-	2	-14.8	0.92	-3.13
5	Rigid (walls)	+-Inf	+-Inf	-	-	108.4	-216.9

Table 7.2: Comparison of impedances (impedance tube vs. experimental) at 250Hz.

@ 500 Hz

surface	Material	Ideal		Tube		Exp.	
		Re	Im	Re	Im	Re	Im
1	Air	1	0	-	-	0.55	-0.245
2	Rigid (Spk)	+-Inf	+-Inf	-	-	-38.1	-41.32
3	Glass Wool	-	-	0.7	1.8	1.13	-1.26
4	Felt	-	-	1	-7.5	0.46	-2.04
5	Rigid (walls)	+-Inf	+-Inf	-	-	235.8	-162.1

Table 7.3: Comparison of impedances (impedance tube vs. experimental) at 500Hz.

rials. The actual impedance values (real and imaginary part) recovered by the iterative approach are listed in Tables 7.1, 7.2, 7.3. These comparison tables show three main columns: impedances for ideal conditions (column ”Ideal”), impedances measured by the impedance tube (column ”Tube”), and the experimental impedances obtained by the iterative method (column ”Exp.”). Detailed figures showing the acoustic impedance of the sample materials measured by the impedance tube are included in Appendix A. From the results shown in the tables the following observations can be made:

- For the surface type of the air opening, experimental values near $1 + j0$ were estimated at all frequencies. This is in agreement with the characteristic (normalized) impedance value of the acoustic media $\mathrm{Z}_0 = 1$.
- The impedances of the hard surfaces resulted, as expected, relatively higher than the soft surfaces.
- The estimated impedances of the glass wool are fairly close to those measured by the impedance tube method.

As in the case of the previous experimental setup (plain rigid walls), the lack of precise impedance values for these type of surfaces prevents a proper comparison with the experimental results. Furthermore, the impedances of the surface type 4 (felt) differ from those measured with the impedance tube. One possible cause of this discrepancy can be attributed to the ill-conditioning of the acoustic transfer matrix. Although the iterative method does not require the inversion of the transfer matric (recall that it is usually nearly-singular), the solution vector that minimizes the optimization equation (6.6) at each iteration is not unique. Therefore, even when some of the impedances in the solution vector are found to be close to the true value, there are still a number of impedance combinations that satisfy (6.6). In order to observe this effect the following simulation test was performed.

7.3.3 Simulation test with empirical and experimental data

Using the 3D mesh model of the experimental setup with the absorbent material installed in the reverberation chamber, two simulations are done. In each simulation field pressures at the experimental measurement points are computed with acoustic BEM at the analysis

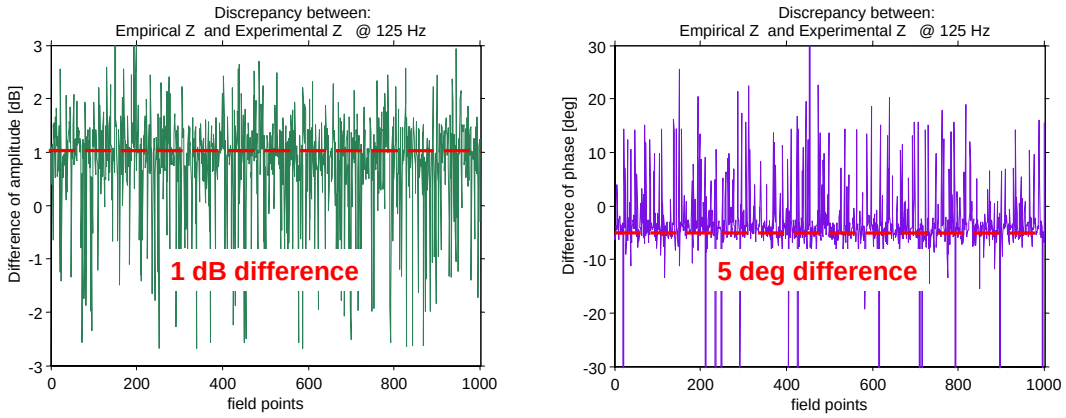

(a) (b)

Figure 7.18: Setup for a validation experiment with impedance boundaries. Five types of impedance boundaries are considered: 1) air opening, 2) hard sides of the speaker, 3) 50 mm–thick glass wool, 4) 5 mm–thick wool felt, 5) rigid walls.

frequency of 125 Hz (the lowest frequency among the frequencies of the experiments was chosen for reasons of computational cost).

For the first simulation, the acoustic impedances that are assigned to the five types of surfaces are those of the columns ”Ideal” and ”Tube” from Table 7.1. This set of impedances will be called ”Empirical Z”. Note that in a computer program, entries of ”infinite” values cannot be assessed, instead the boundary condition $v_S = 0$ is used for rigid surfaces. Using the Empirical data set, field pressures at 1000 points is generated.

For a second simulation, the impedances estimated from the experimental setup with absorbents (which will be referred as ”Experimental Z”) are used to assigned boundary conditions to BEM and generate another set of field pressures at the same points of the previous simulation, at the same frequency 125 Hz, and using the same 3D mesh model.

Finally, the sets of field pressures from both simulations are then compared to observe the discrepancy between the sound fields produced by the Empirical Z and the Experimental Z. In Figure 7.18a–b the differences of amplitude and phase are plotted.

As the graphs suggest, both sets of impedance boundaries (Empirical and Experimental) reproduce nearly the same sound field in the interior of the reverberation chamber. In fact, the average difference between the pressure amplitude of both sound fields is 1 dB, and an average phase difference of 5 degrees. This means that the iterative approach found an equivalent combination of complex impedances that closely reproduce the sound field produced by the empirical values, and at the same time they are near approximations

to the real impedances. If we consider that differences of sound pressure of this order are in many cases not perceptible for the human hear, the impedances estimated by the proposed method represent a suitable set of equivalent impedances close to the original set. This is extremely useful in acoustics simulations of interior spaces where the numerical method implemented requires the specification of boundary conditions in order to make predictions of sound fields.

In summary, the iterative optimization approach showed to have some advantages over the constrained least-squares method:

- while in the least-squares approach the number of unknowns is as big as $2N$, where N is the number of nodes in the 3D mesh, in the iterative optimization method the dimensionality is reduced dramatically to m, where m is the number of surfaces of different types.
- experiments proved that the iterative approach is capable to find meaningful solutions using experimental data, in contrast to the least-squares solutions which are dominated by errors.
- as a consequence of the reduction of the dimensionality of the optimization problem, the iterative approach requires less storage memory for the calculations.

On the other hand, the main drawback of the iterative method is its slow convergence. As shown in Figure 7.17, after a big jump to lower residual the process continues with small improvements. At this time, the solutions estimated at each iteration can readily reproduce sound fields similar to the sound field produced by the real impedances. Regarding this, the problem is now to establish a criterion to stop the iterations before the solution becomes dominated by random errors. This problem is targeted to future work.

Chapter 8

Conclusions

8.1 Conclusions and summary

In-situ measurement of acoustic properties of materials remains as an active research subject in the inverse acoustic area. The present work represent a novel contribution to the measurement techniques of passive materials. The method introduced in this dissertation attempts to estimate the acoustic impedance of the interior surfaces of an entire space by taking samples of sound at random places in the field. The inverse estimation of acoustic impedances is based on the inverse boundary element method (IBEM), which is fundamentally a restatement of the linear equations resulting from the discretization of the Helmholtz acoustic equation for an enclosed surface. However, the inverse linear system of equations is rank deficient and the acoustic transfer matrix of this system is severely ill-conditioned. Therefore special techniques for the regularization of the solution have to be applied. In this work, two methods to overcome this problem have been proposed:

1. a constrained least-squares optimization that computes surface pressure and particle velocity at each element of the 3D mesh, then the acoustic impedance is known from the pressure and velocity. This method is effective if one can ensure negligible noise levels in the measured data.

2. an iterative approach which computes directly the impedance values of the n different surfaces in the interior. This method reduces dramatically the dimensionality of the problem, from $2N$ to m, where N is the number of elements in the mesh of the geometric model and m is the number of interior surfaces of distinct materials. Moreover, the inversion of the nearly-singular matrix in the system of equations is

avoided.

The ill-conditioning, however, is still present and affects the performance of both methods. In the case of the iterative method, this is specially observed in the slow convergence of the algorithm due to the existence of many solutions that minimize the cost function. On the other hand, although both methods exploit information of how the physical surfaces are distributed in the interior space, the iterative approach showed to be more robust to the constrain least-squares method. It is concluded therefore that the iterative method is applicable to practical situations. This method can further be improved by more sophisticated iterative techniques such as Krylov subspace methods.

Regarding the importance of the work presented here, there are a number of reasons why such a system is desired:

- most of the current numerical methods for the simulation of sound responses require knowledge of the acoustic properties of the materials that are simulated. For example, if the simulation of the sound response of a room is done by finite element methods (FEM) or boundary element methods (BEM), specification of the boundary conditions (e.g. acoustic impedance) is needed.

- Although there are databases of acoustic impedances for common materials, it is difficult to match this values with the acoustic impedance of materials that are installed in an already constructed building. Moreover, samples of those materials may not be taken to the laboratory for measurement. Therefore, in-situ measurement is necessary.

- Furthermore, if the acoustic impedances of all the surfaces in an room are known at once, more accurate predictions of the sound field are possible.

- Having knowledge of the impedance of all surfaces in the interior, acoustic optimization can be perform by means of simulations in order to reduce noise levels or to produce a determined acoustic response of that room. These simulations bring the possibility to avoid unnecessary expenses in the actual acoustic optimization.

- Inverse methods in Computer Graphics (CG) have achieved the synthesis of virtual environments with realistic visual effects by acquiring the reflectance properties of the real objects from their photographs. Hence, the work presented here is an

analogous to the work in CG that will eventually become its complement (Inverse sound rendering).

On the other hand, the contributions of the research work presented here can be summarized are as follows:

- A first attempt to estimate the acoustic impedance of all the interior surfaces in a real interior space by inverse boundary elements methods.
- The introduction of the concept of Inverse Sound Rendering as a new paradigm in the area of inverse acoustic problems, as an analogous to Inverse illumination rendering in Computer graphics.
- The development of two optimization methods for the solution of an ill-conditioned inverse acoustic problem that falls in the category of interior boundary formulations of the Helmholtz equation, applied to the estimation of acoustic impedances at the boundaries of large-scale models.
- The elimination of the restriction of complex microphone arrays and the possibility to use sound samples measured at random points inside the enclosed space.

8.2 Future work

As mention before, this kind of acoustic inverse problems are actively finding applications in several acoustic areas. Thus the improvement of the work presented in this dissertation can be supported by advances in the area of Inverse problems. For example, recent work on iterative optimization theory have proposed fast convergent algorithms that can be applied to large–scale problems. In those algorithms, techniques of stopping criteria for iterative methods have been suggested. Moreover, the adaptation of such methods, like Krylov subspace (e.g. [10]) and Trust-Region methods (e.g. [75]) to solve an inverse acoustic problem such as the one addressed in this work, represent motivation for future research. Another issue considered for future work is the use of faster numerical simulation tools that allow the prediction of sound field with less computational cost. Namely, the Fast Multipole Boundary Element Method (FMBEM), that has shown notable achievements in the computation of sound fields in large spaces, [78]. The possibility to estimate acoustic impedances of the surfaces within a range of frequencies by performing only one

measurement of the field points (i.e. not several measurements for each frequency step) will be also studied.

The final challenge is to perform experiments in real rooms where there are a number of surfaces with complex geometries. The impedances of the surfaces will be then attempted. In principle, the BEM is able to handle irregular geometries provided that a suitable mesh is used, thus complete rooms (like the office room shown in a previous numerical example) will be targeted for practical applications.

Appendix A

Acoustic impedance measurements by the impedance tube method

One of the widely employed methods to measure normal acoustic impedance of absorbent materials is the *impedance tube*. The standardized method implemented in [35] is used in the present work to measure the normal acoustic impedances of two absorbent materials: 1) 50 mm–thick glass wool, and 2) 5 mm–thick wool felt.

The actual hardware used for this measurements is displayed in Figure A.1 together with the absorbent samples. The impedance tube is a B&K type 4206 which can perform measurements of normal incidence parameters such as *sound absorption coefficient*, *reflection coefficient*, *acoustic impedance*, and *acoustic admitance*, within the range of frequency 50 Hz–1.6 kHz for a **large-tube** setup, and 500 Hz–6.4 kHz with a **small-tube** setup. Details of these mountings can be found in [4]. The measurement technique is based on the two-microphone transfer function method established in the international standard [35].

With the large-tube setup the acoustic impedance of the two specimens shown in Figure A.1b is measured. The procedure for the measurements is as in the description given in [35]. Nevertheless some practical aspects should be taken into account when performing the measurements: when collocating the absorbent materials in the interior of the tube, it is important to make sure that the size of the specimens fits smoothly the transversal section of the tube (100 mm diameter), and to eliminate as much as possible the air gaps between the rigid backing and the surface of the sample material. In the case of thick porous materials, it is also important that the effective thickness of the specimen is kept all over the transversal area. Sometimes when the materials are pushed by the adjustable

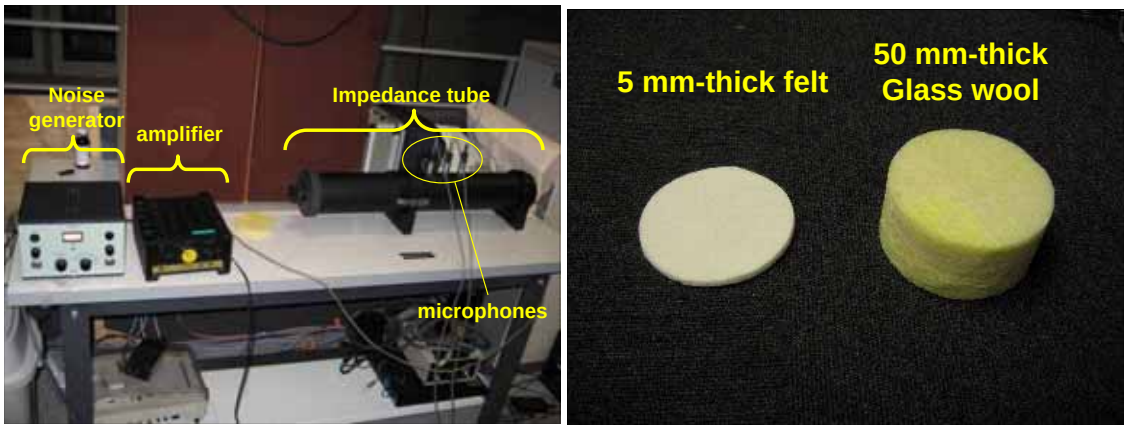

(a) (b)

Figure A.1: a) Setup for impedance measurements with the impedance tube. b) Samples of the absorbent materials used with the impedance tube.

rigid backing provided with the tube kit, the materials are compressed by this rigid plate altering the effective thickness, thus incorrect impedance measurements are obtained as a result.

It is common to use a broadband signal to excite the speaker of the tube so that impedance measurements can be achieved within a range of frequencies. For the experiments done in the present work, a pink noise signal was used since the rage of frequencies of interest is within 125 Hz to 1 kHz. In any case, the level of the output power should be fixed during all the measurement procedure and it should be high enough so as to ensure a good signal to noise ratio, but not too strong so as to produce non–linear response of the specimen and the tube as well. An output power of 5 W is enough to excite the interior of the tube and to prevent permanent damage to the speaker, (the max. average power supported by the speaker of the B&K Type 4206 is 10 W). For the analysis of the signals coming from the microphones, the Multichannel Data Acquisition unit B&K Type 2816 was employed together with a B&K PULSE analysis software. With this software the acquisition process is fully automated, and analysis parameters such as complex cross-power spectrum coefficients can be directly obtained. This complex coefficients are then used in MS-Excel routines to compute the transfer functions between the microphones. Once the transfer functions are known, the acoustic impedances are calculated for the range frequencies mentioned above with a resolution step of 1 Hz. The formulas employed in all the calculations are those prescribed in [35]. Figures A.2 and A.3 show the normal acoustic impedances of the two specimens measured with the impedance tube.

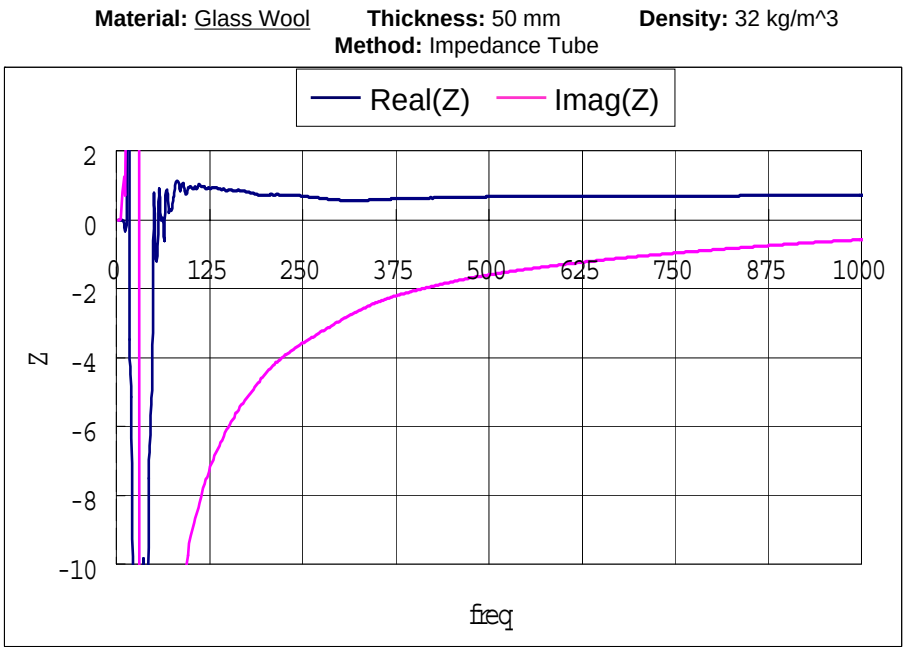

Figure A.2: Normal incidence impedance of the Glass wool measured with the impedance tube method.

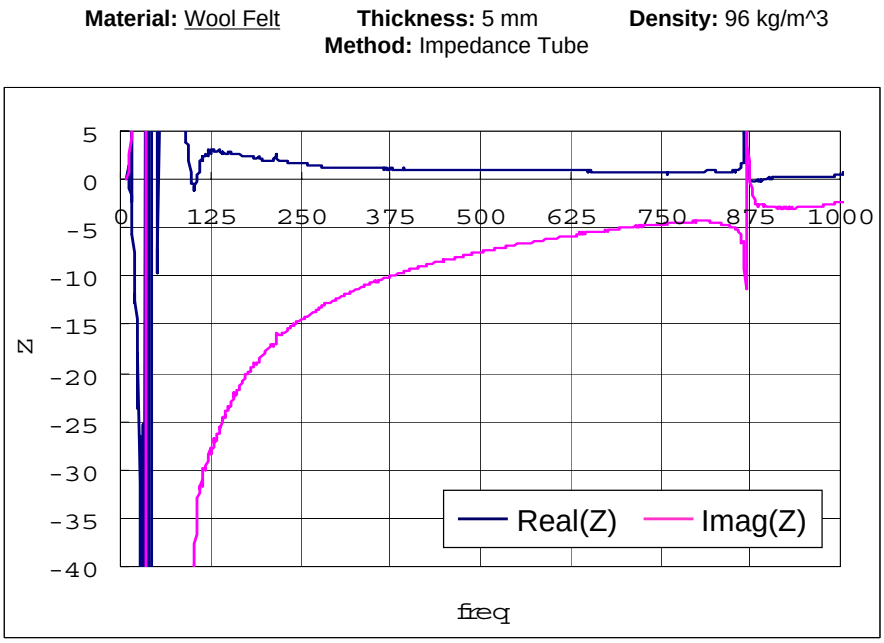

Figure A.3: Normal incidence impedance of the Felt measured with the impedance tube method.

List of publications

1. Gabriel Pablo Nava, Yosuke Yasuda, Yoichi Sato and Shinichi Sakamoto. *In-situ estimation of acoustic impedance on the surfaces of a room for inverse sound rendering*. In Proc. Int. Conf. on Noise and Vibration Engineering ISMA 2006, Leuven, Belgium, paper No.460, 2006.

2. Gabriel Pablo Nava, Yosuke Yasuda, Yoichi Sato and Shinichi Sakamoto. *An inverse method for the in-situ estimation of acoustic surfaces impedance targeting inverse sound rendering in rooms*. In Proc. Int. Congress and Exhibition on Noise Control Engineering Inter-Noise 2006, Honolulu, Hawaii, paper No.280, 2006.

3. Gabriel Pablo Nava, Hidehiko Tanaka and Ichiro Ide. *A convolutional kernel . based approach for note onset detection in piano-solo audio signals*. In Proc. Int. Symposium on Musical Acoustics ISMA2004, Nara, Japan, 2004.

4. Gabriel Pablo Nava, Hidehiko Tanaka and Ichiro Ide. *Finding music beats and tempo by using an image processing technique*. In Proc. Int. Conf. on Information Technology and Applications ICITA2004, Harbin, China, 2004.

References

[1] ARFKEN, G. B., AND WEBER, H. J. *Mathematical methods for physicists*. Harcourt Academic Press, 2001.

[2] BAI, M. R. Application of BEM (boundary element mehtod)- based acoustic holography to radiation analysis of sound sources with arbitrarily shaped geometries. *Journal of the Acoust. Soc. of Amer.*, *92*, 1 (1992), 533–549.

[3] BENCHMARK. Benchmark platform on computational methods for achitectural–enviromental acoustics. http://gacoust.hwe.oita-u.ac.jp/AIJ-BPCA/.

[4] B&K. Br*ü*el&Kjær Impedance Tube Kit – Type 4206. Br*ü*el&Kjær Product data.

[5] BOIVIN, S., AND GAGALOWICZ, A. Image–based rendering of diffuse, specular and glossy surfaces from a single image. In *Proc. of SIGGRAPH 2001* (2001), pp. 107–116.

[6] BORGIOTTI, G. V., AND ROSEN, E. M. The determination of the far field of an acoustic radiator from sparse measurement samples in the near field. *Journal of the Acoust. Soc. of Amer.*, *92*, 2 (1992), 807–818.

[7] CALVETTI, D., LEWIS, B., AND REICHEL, L. On the choice of subspace for iterative methods for linear discrete ill-posed problems. *Journal of Appl. Math. Comput. Sci.*, 11 (2001), 1069–1092.

[8] CALVETTI, D., LEWIS, B., AND REICHEL, L. GMRES, L–curves and discrete ill-posed problems. *BIT*, 42 (2002), 44–65.

[9] CALVETTI, D., LEWIS, B., AND REICHEL, L. On the regularization properties of the GMRES method. *Numerical Mathemathics*, 92 (2002), 605–625.

[10] CALVETTI, D., REICHEL, L., AND SHUIBI, A. Enriched krylov subspace methods for ill-posed problems. *Linear Algebra Appl.*, 362 (2003), 257–273.

[11] CISKOWSKI, R. D., AND BREBBIA, C. A. *Boundary Element Methods in Acoustics*. Computational Mechanics Publications and Elsevier Science Publishers, 1991.

[12] COX, T. J., AND D'ANTONIO, P. *Acoustic absorbers and diffusers, theory design and application*. Spon Press, 2004.

[13] CREMER, L., MÜLLER, H. A., AND SCHULTZ, T. J. *Principles and applications of room acoustics*, vol. 1. Applied Science Publishers, 1982.

[14] DAHLQUIST, G., BJÖRCK, A., AND ANDERSON, N. *Numerical Methods*. Prentice–Hall, 1974.

[15] DE MUNCK, J. C., FAES, T. J. C., AND HEETHAAR, R. M. The boundary element method in the forward and inverse problem of electrical impedance tomography. *IEEE Trans. on Biomedical Engineering, 47*, 6 (2000), 792–800.

[16] DELILLO, T., ISAKOV, V., VALDIVIA, N., AND WANG, L. The detection of surface vibrations from interior acoustical pressures. *Inverse Problems, 19* (2004), 507–524.

[17] DERICHE, R. Fast algorithms for low-level vision. *IEEE Trans. on Pattern Analysis and Machine Intelligence, 12*, 1 (1990), 78–87.

[18] DUTILLEAUX, G., VIGRAN, T. E., AND KRISTIANSEN, U. R. An in-situ transfer function technique for the assessment of the acosutic absorption of materials in buildings. *Applied Acoustics*, 62 (2001), 555–572.

[19] DUTILLEUX, G., SGARG, F. C., AND KRISTIANSEN, U. R. Low-frequency assessment of the in situ acoustic absorption of materials in rooms: an inverse problem approach using evolutionary optimization. *Int. J. Numer. Meth. Eng., 53*, 9 (2002), 2143–2161.

[20] FILLIPI, P. J. T., AND PIRAUX, J. Noise source modeling and identification. *Journal of Sound and Vibration, 98*, 4 (1985), 596–600.

[21] FLETCHER, N. H., SMITH, J., TARNOPOLSKY, A. Z., AND WOLFE, J. Acoustic impedance measurements–correction for probe geometry mismatch. *Journal of the Acoust. Soc. of Amer., 117*, 5 (2005), 2889–2895.

[22] FORSYTH, D. A., AND PONCE, J. *Computer Vision, A modern approach*. Prentice–Hall, 2003.

[23] FUNKHOUSER, T., JEAN-MARC, J., AND TSINGOS, N. Sounds good to me: Computational sound for graphics, virtual reality and interactive systems. In *Course notes of SIGGRAPH 2002* (San Antonio, USA, 2002).

[24] GARAI, M. Measurement of sound-absorption coefficient in-situ: The reflection method using periodic pseudo-random sequences of maximum length. *Applied Acoustics*, 39 (1993), 119–139.

[25] GOLUB, G. H., AND VAN-LOAN, C. F. *Matrix Computations*. The John Hopkins University Press, 1996.

[26] GONZALEZ, R. C., AND WOODS, R. E. *Digital Image Processing*. Prentice–Hall, 2002.

[27] HALD, J. STSF – a unique technique for scan-based near-field acoustic holography without restrictions of coherence. Tech. rep., Brüel&Kjær Technical Review, 1989.

[28] HALD, J. Spatial transformation of sound field STSF techniques in the automotive industry. Tech. rep., Brüel&Kjær Technical Review, 1995.

[29] HANKE, M. Conjugate gradient type methods for ill-posed problems. *Longman, Harlow,* (1995).

[30] HANSEN, P. C. Regularization tools: A Matlab package for analysis and solution of discrete ill-posed problems. *Numerical Algorithms*, 6 (1994), 1–35.

[31] HANSEN, P. C. Rank deficient and discrete ill-posed problems. *SIAM,* (2002).

[32] HANSEN, P. C., AND O'LEARY, D. P. The use of the L-curve in the regularization of discrete ill-posed problems. *SIAM Journal of Sci. and Comput.*, 14 (1993), 1487–1503.

[33] HARTLEY, R., AND ZISSERMAN, A. *Multiple view geometry in computer vision*. Cambridge University Press, 2003.

[34] IKEUCHI, K., AND HORN, B. K. P. Numerical shape fron shading and occluding boundaries. *Artificial Intelligence, 17*, 1–3 (1981), 141–184.

[35] ISO10534-2. Acoustics – Determination of sound absorption coefficient and impedance in impedance tubes – Part 2: Transfer-function method, 1998. International standards, ISO 10534–2(1998).

[36] JACOBY, S. L. S., KOWALIK, J. S., AND PIZZO, J. T. *Iterative methods for nonlinear optimization problems*. Prentice–Hall, 1974.

[37] JEON, I. Y., IH, J. G., AND KIM, B. K. Bem-based holographic reconstruction with additional field information. In *Proc. Int. Congress and Exhibition on Noise Control Engineering Inter-Noise 2003* (Seogwipo, Korea, 2003). paper No. 127.

[38] KIM, B. K., AND IH, J. G. Reconstruction of vibro-acoustic field of car panels using acoustic bem. In *Proc. of Inter-Noise 95* (1995), pp. 1341–1344.

[39] KIM, B. K., AND IH, J. G. On the reconstruction of the vibro-acoustic field over the surface enclosing and interior space using the boundary element method. *Journal of the Acoust. Soc. of Amer., 100*, 5 (1996), 3003–3016.

[40] KIM, G. T., AND LEE, B. H. 3–D source reconstruction and field reprediction using the helmholtz integral equation. *Journal of Sound and Vibration, 136*, 2 (1990), 245–261.

[41] KIM, J. K., AND IH, J. G. Prediction of sound level at high–frequency band by means of a simplified boundary element mehtod. *Journal of the Acoust. Soc. of Amer., 112*, 6 (2001), 2645–2655.

[42] KIM, Y., AND NELSON, P. A. Optimal regularization for acoustic source reconstruction by inverse methods. *Journal of Sound and Vibration*, 275 (2004), 463–487.

[43] KINSLER, L. E., FREY, A. R., COPPENS, A. B., AND SANDERS, J. V. *Fundamentals of acoustics*. John Wiley & Sons, 1982.

[44] KIRKUP, S. *The Boundary Element Method in Acoustics*. Integrated Sound Software, 1998.

[45] KIRKUP, S. M. The computational mdelling of acoustic shields by the boundary and shell element method. *Computers and Structures, 40*, 5 (1991), 1177–1183.

[46] KIRKUP, S. M. Computational solution of the acoustic field surrounding a baffle panel by the Rayleigh integral method. *Appl. Math. Modelling*, 18 (1994), 403–407.

[47] LAWSON, C. L., AND HANSON, R. J. *Solving Least Squares Problems*. Prentice–Hall, 1974.

[48] MAEKAWA, Z., AND LORD, P. *Environmental and achitectural acoustics*. E&FN Spon, 1994.

[49] MAKAROV, S. N. An iterative solver of the Helmholtz integral equation for high-frequency acoustic scattering. *Journal of the Acoust. Soc. of Amer., 103*, 2 (1998), 742–750.

[50] MAYNARD, J. D., WILLIAMS, E. G., AND LEE, Y. Nearfield acoustic holography: I. Theory of the generalized holography and the developement of the NAH. *Journal of the Acoust. Soc. of Amer., 78*, 4 (1985), 1395–1413.

[51] MITRA, S. K. *Digital Signa Processing*. McGraw Hill, 1998.

[52] MOMERTZ, E. Angle-dependent in situ measurement of reflection coefficients using a substraction technique. *Applied Acoustics, 46*, 3 (1995), 251–264.

[53] MONKS, M., OH, B. M., AND DORSEY, J. Audioptimization: Goal-based acoustic design. *IEEE Computer Graphics and Applications, 20*, 3 (2000), 76–91.

[54] NELSON, P. A., AND YOO, S. H. Estimation of acoustic source strength by inverse methods: Part I, conditioning of the inverse problem. *Journal of Sound and Vibration, 233*, 4 (2000), 643–668.

[55] NELSON, P. A., AND YOO, S. H. Estimation of acoustic source strength by inverse methods: Part II, experimental investigation of methods for choosing regularization parameters. *Journal of Sound and Vibration, 233*, 4 (2000), 669–705.

[56] NOKE, C. In-situ acoustic impedance meausrement using a free-field transfer function method. *Applied Acoustics*, 59 (1998), 253–264.

[57] NOKE, C., AND MELLERT, V. Breif review on in situ measurement techniques of impedance or absorption. In *Proc. of Forum Acusticum, Sevilla* (2002).

[58] OCHMANN, M., HOMM, A., MAKAROV, S., AND SEMENOV, S. An iterative GMRES-based boundary element solver for acoustic scattering. *Engineering Analysis with Boundary Elements*, 27 (2003), 717–725.

[59] PABLO-NAVA, G., TANAKA, H., AND IDE, I. A convolutional kernel . based approach for note onset detection in piano-solo audio signals. In *Proc. Int. Symposium on Musical Acoustics ISMA2004* (Nara, Japan, 2004).

[60] PABLO-NAVA, G., TANAKA, H., AND IDE, I. Finding music beats and tempo by using an image processing technique. In *Proc. Int. Conf. on Information Technology and Applications ICITA2004* (Harbin, China, 2004).

[61] PABLO-NAVA, G., YASUDA, Y., SATO, Y., AND SAKAMOTO, S. In-situ estimation of acoustic impedance on the surfaces of a room for inverse sound rendering. In *Proc. Int. Conf. on Noise and Vibration Engineering ISMA 2006* (Leuven, Belgium, 2006). paper No. 460.

[62] PABLO-NAVA, G., YASUDA, Y., SATO, Y., AND SAKAMOTO, S. An inverse method for the in-situ estimation of acoustic surfaces impedance targeting inverse sound rendering in rooms. In *Proc. Int. Congress and Exhibition on Noise Control Engineering Inter-Noise 2006* (Honolulu, Hawaii, 2006). paper No. 415.

[63] PATOW, G. A survey of inverse rendering problems. In *Proc. of Computer Graphics Forum* (2003), 22, pp. 663–667.

[64] PHILLIPS, D. L. A technique for numerical solution of certain numerical equations of the first kind. *Journal of the Assoc. Comput. Mach.*, 9 (1992), 84–97.

[65] PHOTIADIS, D. M. The relationship of singular value decomposition to wave-vector filtering in sound radiation problems. *Journal of the Acoust. Soc. of Amer., 88*, 2 (1990), 1152–1159.

[66] PIERCE, A. D. *Acoustics, An introduction to its physical principles and applications*. Acoustical Society of America, 1989.

[67] PINA, H. L. G., FERNANDES, J. L. M., AND BREBBIA, C. A. Some numerical integration formulae over triangles and squares with $1/r$ singularity. *Applied Mathematics Modelling*, 5 (1981), 209–211.

[68] POINT-GREY. Point grey inc. http://www.ptgrey.com.

[69] PRESS, W. H., TEUKOLSKY, S. A., VETTERLING, W. T., AND FLANNERY, B. P. *Numerical recipes in C, The art of scientific computing*. Cambridge Unversity Press, 1999.

[70] RALTSON, A. *A first course in numerical analysis*. McGraw–Hill, 1965.

[71] RAMAMOORTHI, R., AND HANRAHAN, P. A signal processing framework for inverse rendering. In *Proc. of SIGGRAPH 2001* (2001), pp. 117–118.

[72] REICHEL, L., AND YE, Q. Breakdown-free GMRES for singular systems. *SIAM J. Matrix Anal. Appl.*, *26*, 4 (2005), 1001–1021.

[73] RIENSTRA, S. W. 1–D reflection at an impedance wall. *Journal of Sound and Vibration*, *125*, 1 (1988), 43–51.

[74] RME. Rme intelligent audio solutions. http://www.rme-audio.com.

[75] ROJAS, M., AND SORENSEN, D. C. A Trust-Region approach to the regularization of large-scale discrete forms of ill-posed problems. *SIAM Journal on Sci. Comp.*, *26*, 3 (2002), 1843–1861.

[76] RUSSELL, D. A., TITLOW, J. P., AND BEMMEN, Y.-J. Acoustic monopoles, dipoles, and quadrupoles: An experiment revisited. *Am. J. Phys.*, *67*, 8 (1999), 660–664.

[77] SAAD, Y. Analysis of augmented Krylov subspace methods. *SIAM J. Matrix Anal. Appl.*, 18 (1997), 435–449.

[78] SAKUMA, T., AND YASUDA, Y. Fast Multipole Boundary Element Method for large-scale steady-state sound field analysis. Part I: Setup and validation. *Acta Acustica united with Acoustica*, 88 (2002), 513–525.

[79] SATO, I., SATO, Y., AND IKEUCHI, K. Illumination distribution from brightness in shadows: adaptive examination of illumination distribution with unknown reflectance properties in shadow regions. In *Proc. of IEEE ICCV 99* (1999), pp. 875–882.

[80] SCHUHMACHER, A. P. *Sound source reconstruction using inverse sound field calculations*. PhD thesis, Technical University of Denmark, 2000.

[81] SCHUHMACHER, A. P., AND HALD, J. Sound source reconstruction using inverse boundary elemtn calculations. *Journal of the Acoust. Soc. of Amer., 113,* 1 (2003).

[82] SCHUHMACHER, A. P., AND HANSEN, P. C. Sound source reconstruction using inverse bem. In *Proc. Int. Congress and Exhibition on Noise Control Engineering Inter-Noise 2001* (The Hague, Netherlands, 2001). paper No. 280.

[83] SIGNAL. Signal processing SA.
. http://www.signal-processing.com/tech/us_data_frame.htm.

[84] SILLION, F. X., AND PUECH, C. *Radiosity and Global Illumination*. Morgan Kaufmann Publishers, 1994.

[85] SVOBODA, T. Multi-camera self-calibration. http://cmp.felk.cvut.cz/ svoboda/SelfCal/.

[86] SVOBODA, T., MARTINEC, D., AND PAJDLA, T. A convenient multi-camera self-calibration for virtual environments. *PRESENCE: Teleoperators and Virtual Environments, 14,* 4 (2005), 407–422.

[87] TAKAHASHI, Y., OTSURU, T., AND TOMIKU, R. In situ measurements of absorption characteristics using two microphones and environmental *anonymous* noise. *Journal of the Acoust. Soc. of Japan, Acoust. Sci. and Tech., 24,* 6 (2003), 382–385.

[88] TEKATLIAN, A., FILLIPI, P., AND HABAULT, D. Determination of vibration characteristics of noise sources solving and inverse radiation problem. *Acoustica,* 82 (1996), 91–101.

[89] TIKHONOV, A. N. Solution of incorrectly formulated problems and the regularization method. *Soviet Math. Dokl.,* 4 (1963), 1035–1038.

[90] TIKHONOV, A. N., GONCHARSKY, A. V., STEPANOV, V. V., AND YAGOLA, A. G. *Numerical methods for the solution of ill-posed problems*. Kluwer Academic Publishers, 1995.

[91] TRUCCO, E., AND VERRI, A. *Intoductory techniques for 3-D computer vision*. Prentice Hall, 1998.

[92] VALDIVIA, N., AND WILLIAMS, E. G. Krylov subspace iterative methods for boundary element method based near–field acoustic holography. *Journal of the Acoust. Soc. of Amer., 117*, 2 (2004), 711–724.

[93] VAN DER VORST, H. A. *Iterative Krylov methods for large linear sytems*. Cambridge University Press, 2003.

[94] VERONESI, W. A., AND MAYNARD, J. D. Nearfield acoustic holography: II. Holopraphic reconstruction algorithms and computer implementation. *Journal of the Acoust. Soc. of Amer., 81*, 5 (1987), 1307–1322.

[95] VERONESI, W. A., AND MAYNARD, J. D. Digital holographic reconstruction of sources with arbitrarily shaped surfaces. *Journal of the Acoust. Soc. of Amer., 85*, 5 (1989), 588–598.

[96] VISSER, R. Acoutic source localization based on pressure and article velocity measurements. In *Proc. of Inter-noise 2003* (Jeju, Korea, 2003), pp. 665–670.

[97] VON ESTORFF, O. *Boundary elements in acoustics - Advances and applications*. WIT Press, 2000.

[98] WANG, Z., AND WU, S. F. Helmholtz equation–least-squares method for reconstructing the acoustic pressure field. *Journal of the Acoust. Soc. of Amer., 102*, 4 (1997), 2020–2032.

[99] WILLIAMS, E. G. *Fourier Acoustics: Sound Radiation and Near Field Acoustical Holography*. Academic Press, 1989.

[100] WILLIAMS, E. G., AND HOUSTON, B. H. Interior near–field acoustical holography in flight. *Journal of the Acoust. Soc. of Amer., 108*, 4 (2000), 1451–1463.

[101] WU, T. W. *Boundary Element Acoustics, Fundamentals and computer codes*. WIT Press, 2000.

[102] YASUDA, Y., AND SAKUMA, T. Fast Multipole Boundary Element Method for large-scale steady-state sound field analysis. Part II: Examination of numerical items. *Acta Acustica united with Acoustica*, 89 (2003), 28–38.

[103] YU, Y., DEBEVEC, P., MALIK, J., AND HAWKINS, T. Inverse global illumination: Recovering reflectance models of real scenes from photographs. In *Proc. of SIGGRAPH 99* (1999), pp. 215–224.